2-22-2021

Investigation of the Structure and Dynamics of Novel Battery Electrolytes by Utilizing Multidimensional Infrared Spectroscopic Techniques

Susith Rajitha Abeythunga Galle Kankanamge
Louisiana State University and Agricultural and Mechanical College

INVESTIGATION OF THE STRUCTURE AND DYNAMICS OF NOVEL BATTERY ELECTROLYTES BY UTILIZING MULTIDIMENSIONAL INFRARED SPECTROSCOPIC TECHNIQUES

A Dissertation

Submitted to the Graduate Faculty of the
Louisiana State University and
Agricultural and Mechanical College
in partial fulfillment of the
requirements for the degree of
Doctor of Philosophy

in

The Department of Chemistry

by
Susith Rajitha Abeythunga Galle Kankanamge
B.Sc., University of Colombo, 2014
May 2021

To my loving parents, ***Dolison*** *and* ***Hemalatha***

මාගේ ආදරණීය දෙමාපියන්ට

ACKNOWLEDGEMENTS

I would like to express my sincerest gratitude to my advisor Professor Daniel Kuroda for continuous guidance and support. He always believed in me and allowed me to learn and perform research by myself and guided me to the correct path whenever I am troubling. He also helped me to improve my hands-on skills in mechanical and technical sides. My graduate career would not be as successful as today without his encouragement. I also thank all my committee members, Prof. Murray, Prof. Gilman, Prof. Kumar, and Prof. Tzanov, for their advice and valuable feedback on my research.

I am thankful for all the current and former group members in the Kuroda group, especially Kristen and Yoawen, for initially teaching me the techniques involved in my projects when I first joined the group, and Xiaoliu, Xiaobing and Jeramie for giving me valuable feedback on my research and proofreading my manuscripts.

I want to extend my gratitude to my brothers Yasith and Lasith, and my sister Malithi for all the support, encouragement and love. I also thank my friends from Sri Lanka as well as from Baton Rouge, especially Udara for giving me all the support.

An enormous thanks to my parents Dolison and Hemalatha for their unconditional love, care, support and for giving me the strength to become the man who I am today. I also thank my uncle Chandrasena and aunt Bandumathi for taking care of me when I was a kid.

Lastly, I want to give a special thank to my wife Nadeesha for her true love and care, and for supporting me through everything.

TABLE OF CONTENTS

ABSTRACT

Novel battery technologies are being developed due to the high global demand for energy in many fields where different specifications are required. The battery electrolyte provides a medium for ions to diffuse between electrodes and its composition determines the compatibility with the electrode pair. While many works focus on characterizing novel electrolyte systems to advance new batteries, the understanding of the microscopic structure and dynamics of speciations present in these electrolytes is limited. Many experiment methods have obtained incomplete time-averaged structure information due to lack of instrumental time resolution compared to the molecular intrinsic time sales of electrolytes that range from femtoseconds to sub-picosecond. Work described in this dissertation utilized linear and nonlinear infrared spectroscopic techniques in conjugation with computational tools to investigate the structure and picoseconds dynamics of novel battery electrolytes. Glyme based electrolyte systems were identified as potential candidates for sodium-ion battery systems and the first project focused on the microscopic structural and dynamical changes of the ion pairs with the length of the glyme. The preliminary study of Fourier transform infrared (FTIR) spectroscopy revealed a strong ionic association in these electrolytes regardless of the glyme length. Two dimensional infrared (2DIR) spectroscopy and IR pump-probe spectroscopy deduced the characteristic time constants of the motions associated with the anion. The experimental findings were later validated with numerical simulation and density functional theory (DFT) calculations. A similar approach was followed to investigate the interactions and motions associated with highly concentrated systems that are composed of bis(trifluoromethanesulfonyl)imide (LiTFSI) and carbonyl-containing solvents. While the overall speciations present in each solvent remain the same, an additional interaction was identified in the cyclic solvent, which was later determined to affect the macroscopic properties of the electrolyte.

Finally, the ionic concentration gradient and changes of the solvation structure and dynamics of electrolytes in presence of an external electric field were studied by probing the anion with linear and nonlinear IR methods. A decrease of the anion near the negative electrode indicated the building of concentration gradient across the electrolyte system and breaking of ionic species was also observed.

CHAPTER 1. INTRODUCTION

1.1 Background of Energy Storage Systems

The high demand for electric energy is a growing global concern nowadays. Fossil-fuel based technologies still fulfill almost eighty percent of the worldwide energy requirement, and it is slowly decreasing as other renewable arising.[1-3] The cost, availability, and environmental factors have brought the attention of the renewable energy sources, especially in the grid electricity and automobile industries.[4] However, most renewable energy sources are intermittent and stochastic sources that prevent them from being a competitive candidate for fossil fuel energy. An effective energy storage system could overcome the barrier to implementing intermittent sources to replace conventional fossil fuel-based techniques. Energy storage can act as an energy leveling system to provide uninterrupted power on demand. Additionally, hybrid renewable sources are possible when the energy sources are weather or season dependent.

The use of energy storage systems has been established long ago with the development of portable instruments and becomes a necessity in many fields with time. High energy density, high specific power, high recyclability, low self-discharge rate, light weight, and long cycle life are the expectations of a good energy storage system, especially in the portable device industry where space limitation is imposed. However, the cost of development and maintenance has more importance weight compared to the physical size of the storage when designing storage systems for energy grids. Therefore, different fields have distinctive expectations from the storage systems.

The discovery of primary batteries, i.e. non-rechargeable, was reported in the 18th century, while the development of rechargeable batteries started in the middle of the 19th century with the discovery of the wet lead-acid battery.[5, 6] An improved version of lead-acid battery is still in use in fields where weight and size are not concerns. Nickel-cadmium batteries were the primary

energy storage system for portable applications until the lithium-ion battery was commercially introduced in 1991.[5, 7, 8] The popularity of lithium-ion batteries has rapidly increased not only in the portable device industry, but also in other fields such as automobile, grid and off-grid electricity.[9-11] Lithium-ion batteries are successful because they have high energy density, high single-cell voltage, and lightweight. Nevertheless, lithium-ion technology is still being developed to improve performance.

Any rechargeable battery consists of three main components, the anode material, cathode material, and electrolyte. The cathode material is considered as the source of ions where the oxidation reaction allows ions to move into the host anode material, where the parallel reduction reaction occurs during the charging cycle. During the discharge cycle, the reverse reaction on each electrode creates an external current through the load. The electrolyte provides the mediums for ions to travel between the two electrodes. Therefore, the overall quality of the battery equally depends on all three components. Different combinations of electrode materials with a compatible electrolyte are used for different rechargeable battery systems, i.e. lithium-ion batteries, sodium-ion batteries, etc. An ideal pair of electrodes provides high capacity, high energy density, high rate of reversible ion insertion and desertion, and high working potential.[11-13] Meanwhile, a good electrolyte should have high conductivity, low viscosity, high working potential window, high thermal stability, and higher electrode stability.[11, 14] For an example, in current lithium ion batteries, the selection of the electrolyte system creates a passivation layer called the solid electrolyte interface on the anode to prevent the degradation of the electrode.[15] However, the development of a rechargeable battery comprised of the aforementioned qualities is impossible due to the practical and theoretical limitations. Therefore, the qualities are optimized to achieve the desired performance in individual applications.

1.2 Contemporary Energy Storage Systems

Lithium-ion battery technology is the most popular rechargeable battery in today's market due to the high energy density and lightweight of the materials. A few types of cathode materials are currently being used in lithium-ion batteries; namely, $LiCoO_2$, $LiNiO_2$, $LiMn_2O_2$, etc.[11, 13, 16, 17] Each material has its own advantages and disadvantages and often blend with auxiliary elements to increase the performance and lifetime.[18] On the other hand, graphite-based electrodes are still being used as the anode since the beginning of the discovery of lithium-ion batteries due to the low cost and high abundance.[16, 17, 19] The most commonly used electrolyte consists of a lithium salt dissolved in a mixture of organic carbonates such as ethylene carbonate, dimethyl carbonate, diethyl carbonate, ethyl methyl carbonate.[20] The use of non-aqueous electrolyte allows the battery to operate at a higher voltage compared to aqueous electrolyte based batteries due to their higher electrochemical window. Moreover, the formation of the solid electrolyte interface on the graphite anode material, which has a lower redox potential, is also increased the operating voltage window.[15, 21] However, the current lithium-ion battery technology faces challenges and complications when implementing in certain fields.

1.3 Issues of Lithium-ion Technology

Currently, the scope of applications of lithium-ion batteries expands to fields such as automobile and electric grids that require high energy capacity, high energy density, and high operating voltage.[5, 7, 13] The existing lithium-ion batteries operate around ~4 V with 372 $mAhg^{-1}$ theoretical capacity which is clearly insufficient to be directly implemented to these areas.[13, 17, 22] Thus, a series of batteries connected in the parallel configuration is required, that hinders achieving smaller dimensions and lighter weight. Consequently, the cost of development of these batteries becomes high, and it will be more expensive in the future as the global depletion of lithium

resources. Besides, current lithium-ion batteries suffer from safety issues, mainly due to the thermal runaway of the organic-based electrolytes of choice that are highly inflammable. Different factors cause this thermal runaway: overcharging the battery, dendrite formation as a result of fast charging, the release of gases due to the overpotential and solvent decomposition.[23, 24] Therefore, the overall battery design is important for the safety features of the lithium-ion batteries, especially in medium and large scales developments.

The scientific community is addressing the ongoing problems with current lithium-ion technology in mainly two ways. First, by using alternative elements to replace lithium ions and second is by using different lithium ion sources with different compositions and configurations.

1.3.1 Lithium Ion Alternatives

The global availability of lithium resources and the high cost of building medium to large lithium-ion batteries have drawn attention in search of inexpensive and high abundant alternative materials. Currently, there are extensive studies on counterparts of lithium ions using neighboring elements in the periodic table. Sodium-based,[25-27] magnesium-based,[28, 29] aluminum-based,[30, 31] potassium-based,[32-35] zinc-based batteries[36-38] are the potential rivals to lithium-ion batteries. However, sodium-based batteries have higher consideration compared to other techniques due to the chemical and physical similarities between sodium and lithium.[39] In fact, research on sodium-ion batteries started parallel to the timeline of the development of the lithium-ion batteries, but quickly faded away due to the immense success of the lithium-ion battery technology.[40] Early development of the sodium batteries were focused on the sodium-sulfur based batteries due to the high capacity and low cost. Molten sodium and molten sulfur were used as the cathode and the electrolyte, hence the working temperature of the battery was high, and the ability to use at room temperature was questionable.[25] Sodium- air battery was introduced in search of high capacity

batteries and their initial working temperature was much smaller compared to sodium-sulfur batteries.[25, 41, 42] Consequently, Sun *et al.* developed a working sodium-air at room temperature but suffered from poor cycling performances.[43] Hence, numerous studies have been conducted to improve the quality of the sodium-air battery.[44-47] At the same time, the battery community is focused on the development of sodium-ion batteries, which follows a similar working mechanism as lithium-ion batteries. One of the biggest challenges in developing sodium-ion batteries is to find proper anode materials. Conventional graphite-based anode materials show less thermodynamical stability with sodium ions compared to that of lithium-ion.[48] Transition metal oxide, transition metal sulfide and transition metal phosphide based electrodes are reported to be good anode materials for sodium ion batteries.[49-51] However, engineering of metal oxide based electrodes will raise the cost and complexity of the battery.

1.3.1.1 Sodium-Ion Battery Electrolytes

An electrolyte that is compatible with sodium-ion batteries should be chemically stable where no side reactions occur during the normal operation, electrochemically stable where redox reactions remain unaltered, and thermally stable where the melting and boiling points are well outside the operating conditions. Thus, the selection of the electrolyte components must be carefully examined in the quest of developing a compatible electrolyte. A wide range of sodium salts has been suggested for sodium-ion battery electrolytes, among them sodium hexafluorophosphate ($NaPF_6$), sodium trifluoromethanesulfonate (NaTf), sodium bis(fluorosulfonyl)imide (NaFSI) and sodium bis(trifluoromethylsulfonyl)imide (NaTFSI) are the most popular ones due to the high dissociative properties in polar solvents. The usual high dielectric polar carbonate solvents that are used for lithium-ion batteries perform poorly on sodium-ion batteries as a consequence of weakly formed solid electrolyte interface on anode

materials.[52, 53] Aqueous based electrolytes were introduced as a solution to the safety problems of lithium-ion batteries where the electrolytes made with high flammable organic solvents.[54] While the concept was extended to sodium-ion batteries, the lower redox potential of water narrows the electrochemical windows of the overall electrolyte system.[55-57] However, high salt concentration of such electrolytes is reported to increase the operating voltage around 2.5 V, but high viscosity of the electrolyte discourages its use.[58] Ionic liquids were proposed as the solvents for the sodium ion electrolyte due to the physicochemical and electrochemical properties, i.e. high boiling point, large electrochemical window, high thermal stability. Ionic liquids are considered as molten salts (liquid) at room temperature with specific organic cation and organic or inorganic anion. Hence, the high viscosity and low conductivity of such an electrolyte system might limit the performance of the battery.[52]

In recent years, there have been studies on electrochemically inert ether-based electrolytes for sodium-ion batteries. Particularly, glymes, ether-based solvents consisting of glycol diether units, have become popular due to the ability of coordination with alkali metals through ether oxygens. Adelhelm *et al.* first time showed highly reversible sodium intercalation into graphite materials using a diglyme based electrolyte.[59] In such a system, the unstable binary graphite intercalation is replaced by ternary intercalation, where the solvated ions intercalate into the graphite crystal structure.[59] Thus, it is evident that careful selection of solvents enables the implementation of low-cost graphite-based anode material for sodium-ion batteries as well.

1.3.1.2 Microscopic Structure of Electrolytes

Following the Adelhelm *et al.* findings of diglyme based electrolytes, more work has been conducted on glyme-based electrolytes. Some studies have discovered correlations between the length of the glyme and properties and performance of the battery, i.e. change in the operating

voltage with glyme's chain length.[60, 61] Therefore, it indicates that interactions between solvent and ions play a major role in defining electrolyte properties. Understanding of interactions at the molecular level enables access to the information needed to reduce the knowledge gap in developing better battery technology.

The dielectric constants of the glymes are reported to be low compared to carbonates, which leave the expectation of weaker ion-dipole interactions between the ions and solvents. However, a higher dissolution power of alkali metals is observed in glymes due to the chelation effect that allows glymes to wrap around the sodium ions.[62] Only a few studies have reported information about the structure and coordination of the glymes with sodium ions. A concentration-dependent study of ionic speciation present in diglyme-based electrolytes revealed the existence of a high percentage of ion pairs even at lower concentrations.[63] Another study explored the ionic speciation in different glymes utilizing FTIR, Raman spectroscopy and NMR, and reached a similar conclusion of a high percentage of ion pairs.[64] A more comprehensive study was carried out using computational tools in conjugation with FTIR experiments to identify the solvation-shell structure.[65] The probability of the counterions present in the first solvation-shell is found to be high when the short length glymes are used. Thus the ionic association is inferred to be important in these systems. Based on these findings, another study pointed out the existence of a non-vehicular type conductive mechanism in shorter glymes.[66] In order to combine the properties of each glymes-based electrolytes, Adelhelm *et al.* again suggested mixing different lengths of glymes.[67] Nevertheless, before reaching such an approach with an incomplete description of glyme-based electrolytes, further investigation of the structure and dynamics of the individual system is required.

1.3.2 High Energy Density Lithium-Ion Batteries

Sodium-based batteries are good alternative options to overcome some of the ongoing problems of lithium-ion batteries, but it may be unsuitable to completely replace the current lithium battery technology due to the lower redox potential and lower energy density of the sodium compared to lithium. Nevertheless, it will be a better economical approach for energy storage where the dimensions and weight are not issues. The energy density of the battery becomes an important factor in portable devices as the extreme power consumption of high-end electronics in these devices. The novel trending of electric automobiles is another emerging technology that requires immense energy density to compete with fuel-based automobiles. In addition, the imposed space and weight requirement in these fields hinder the implication of sodium technology. Thus, lithium being the lightest metal on the periodic table makes scientists to further advance lithium battery technology because of its high energy density storage per unit weight.

The energy density of the current lithium-ion battery is mainly dictated by the specific capacity of the graphite-based anode material. Hence, the scientific community is conducting intensive research in new anode materials in search of higher energy density batteries. There have been some studies on lithium metal based[68-74], silicon based[75-79], molybdenum based[80, 81], tin based[82] anode materials to replace the conventional graphite-based anodes, but lithium metal and silicon-based anode materials are highlighted due to their theoretical capacity of ~3900 $mAhg^{-1}$ and ~4200 $mAhg^{-1}$, respectively.[75] Initially, the silicon-based anode materials are reported to undergo high volumetric changes during the lithiation and delithiation processes, and Nano-structured designs have been proposed to overcome the problem.[83-87] These complex engineered electrode materials are raising concerns about the building cost. Thus, the studies are currently centered around lithium metal anodes because of their straightforward utilization.

1.3.2.1 Lithium metal anodes

The high chemical reactivity of the currently used carbonate-based solvents with lithium metal reduces the higher-cycling performance. As mentioned above, the formation of a solid electrolyte interface protects the electrode by blocking further reaction with solvent molecules. Unlikely in the case of the graphite-based electrode, the solid interface formed on lithium metal is fragile and inhomogeneous. Therefore, the uneven lithium-ion deposition on lithium metal causes different nucleation sites, which results in a dendrite formation. The formed dendrites can further react with the remaining solvent molecules and create another fragile solid electrolyte interface that eventually breaks off and leads to further dendrite growth until triggers the internal short-circuit.

Interfacial engineering enables creating an artificial protective layer on top of the lithium metal and improving the cyclic performance of the battery.[88-91] Nanometer-scale MoS_2 based protective layers have been reported to suppress the dendrite formation due to high mechanical stiffness.[92] In-situ layer deposition techniques also proven to be effective in protecting the lithium anode in addition to ex-situ plating.[90, 93] While these techniques are recognized to be an efficient way to increase the durability of the battery, the complexity that brings for development might not be cost-effective.

1.3.2.2 Electrolytes for High Energy Density Lithium-Ion Batteries

Henderson *et al.* studied the structure of high concertation glyme-based lithium electrolytes as a potential solution to dendrite formation.[94, 95] However, in 2008, Ogumi *et al.* demonstrated suppression of dendrite formation using electrolyte compose of $LiN(SO_2C_2F_5)_2$ in propylene carbonate at high concentration.[96] Since then, the electrolyte community has tested various lithium salts at high concentrations in various organic solvents as well as aqueous systems.[97] Yamada *et*

al. presented exceptional stability in lithium-metal-based battery systems when using a super-concentrated $LiN(SO_2CF_3)_2$ in acetonitrile.[98] The high reactivity of lithium with acetonitrile was found to be prevented in high concertation electrolyte due to the limited availability of the free solvent molecules. Interestingly, the electrochemical window has widened in the electrolyte of the study, indicating the potential application of high voltage batteries. Later, the same group showed high cyclic performance on high concentrated $LiN(SO_2F_3)_2$ in carbonate-based electrolytes, where the limitation of free solvent also reduces safety issues of inflammable free solvents.[99] Zhang et al also presented the highly cycled high concentration electrolyte system compose of $LiN(SO_2F_3)_2$ and 1,2-dimethoxyethane, and show the morphology of suppression of dendrite formation.[73]

Thus, it has been established that increasing the salt concentration can provide stability to the lithium-metal-based anode material by suppressing dendrite formation and increasing the electrochemical window. However, it is important to note that the viscosity of the electrolyte will be increased as the salt concentration increases, which results in slower ionic diffusion through the electrolyte. These conditions are not favorable in the charging and discharging rates of the battery. Watanabe *et al.* discovered an undergoing hopping conduction mechanism in high concentrated $LiBF_4$ in sulfolane as a result of the bridging of lithium clusters.[100] Later, they showed the same conduction mechanism is responsible for different high concentrated electrolyte systems.[101-103] While it is tempting to assume a similar type of mechanism is involved in any high concentrated electrolyte systems, a change in counter ion may change the origin of the conduction mechanism. Xia *et al*. discovered that electrochemically inert solvents could be introduced to lower the viscosity of the high concentration electrolyte systems without interrupting the properties.[104] Therefore, understanding of the microscopic structure parameters and dynamics are important in the development of a better electrolyte system. While Henderson *et al.* have given a significant

contribution to the findings in structural parameters of high concentration electrolyte solvates which are in solid states[105-110], the studies on the solvation structure of liquid phase systems are limited.[111, 112]

1.4 Methods

Various experimental tools, such as linear and nonlinear infrared spectroscopy,[113-117] Raman spectroscopy,[118-123] nuclear magnetic resonance,[123-127] mass spectrometry,[128, 129] and X-ray diffraction,[130, 131] have been utilized to obtain the microscopic structure information in different electrolyte systems. NMR, mass spectroscopy and X-ray diffraction have identified some spatial arrangement of the lithium solvation-shell in electrolytes. However, only time-resolved nonlinear infrared spectroscopy has the time resolution to study the molecular motion in the femtosecond to sub-picosecond scales. Thus, the aforementioned techniques only provide the time-averaged structural information rather than instantaneous structure details. Time-resolved infrared spectroscopy obtains the structural and dynamical parameters by accessing the vibrational energy profile of the molecular probes that are sensitive to the environment and responds to the changes in the vicinity. Therefore, nonlinear IR spectroscopic techniques have been used in different fields to obtain the structural and dynamical information that can not be resolved by other techniques, i.e. battery electrolytes,[54, 114-117, 132, 133] deep eutectic solvents,[134-137] ionic liquids,[138-141] proteins.[142-144]

1.5 Objectives

The main objective of my dissertation was to investigate the microscopic solvation structure and dynamics of novel battery electrolytes. The motivation of my work arises from the lack of knowledge of solvation structure information of the proposed electrolyte systems that work with novel electrode materials. The microscopic structure parameters are important in optimizing

the ion-solvent interactions to obtain desired properties such as conductivity, viscosity. In addition, an effort is made to observe the structural and dynamical changes that undergo during charging and discharging conditions.

In the following chapter, the methods and mathematical concepts of linear and nonlinear spectroscopy are discussed in context. Initially, a semi-classical description of molecular-field interaction will be described and then extended to explain the molecular ensemble-field interaction with the help of density matrix treatments. The generation of linear and nonlinear macroscopic polarization due to field interactions is derived, and the time evolution of the polarization is described according to the system Hamiltonian. The emission of a photon echo due to the rephasing polarization is also explained. Later, the techniques that are used to conduct such experiments are discussed.

Chapter 3 of this dissertation is focused on characterizing the structure parameters and dynamics of ion paired formed in glyme based sodium electrolyte systems. Glyme-based sodium electrolytes are considered good candidates for sodium-ion and sodium-air batteries, but still, there are unresolved questions to be answered regarding the interactions between the ion and glyme when the chain length is changed. While the recent studies found the ion paired present in these systems plays an important role in the conductivity mechanism, the understanding of solvation structure and motions were unclear. Thus, to answer these questions, sodium thiocyanate dissolved in different glyme lengths were understudied.

The correlation between the microscopic structure and macroscopic properties in high concentration lithium-based electrolytes is discussed in Chapter 4. The proposed high concentration electrolytes for the lithium-metal-based batteries are still in the early development stage due to a lack of knowledge in ion-ion and ion-solvent interactions. Therefore, a series of

carbonate-based high concentration lithium electrolyte systems was studied to find the structure and motions of the ionic clusters that present in high concentration electrolytes.

The final chapter discusses the in-situ method to determine the concentration gradient of the ions and ionic speciation present in the electrolyte system under an external electric field. The ionic concentration gradient was determined by probing the anion. The experimental setup and the results are in the preliminary stage and require further improvements.

CHAPTER 2. THE THEORY OF LINEAR AND NONLINEAR SPECTROSCOPY

In this chapter, the theory and mathematical concepts behind the linear and nonlinear spectroscopy are discussed along with the derivation of third-order nonlinear signal results from two dimensional infrared spectroscopy (2DIR) experiments. The interaction between the electric field and the molecules is considered to be weak compared to molecular internal interactions, but strong enough to create a perturbation to the system equilibrium and generate a macroscopic polarization. The generated macroscopic polarization is proportional to a response function that intrinsically evolves according to the molecular system of interest. The electromagnetic signal emitted due to the generated macroscopic polarization is detected with a local oscillator on a square-law detector to preserve all the information of the molecular system including the phase and sign. The lineshape and properties of the 2DIR spectrum are defined by the structure and dynamics of the system under study. The experimental designs and data acquisition of 2DR experiments are described at the end of this chapter.

2.1 Molecular Vibrational Modes

Molecules oscillate as simple harmonic oscillators when the correct amount of energy is provided. The IR frequency range of the electromagnetic spectrum can access the vibrational modes of molecular systems when the field is in resonance with the energy difference in adjacent vibrational eigenstates of a given vibrational mode. The energy of the individual eigenstate of a single molecule is derived from the Schrodinger equations and expressed up to the second order as:

$$E_n = \hbar\omega\left(n+\frac{1}{2}\right) - \chi\left(n+\frac{1}{2}\right)^2 \tag{2.1}$$

where the ω is the harmonic oscillation frequency, n is quantum level and χ is the anharmonicity. The number of vibrational modes of a molecule is 3N-5 for a linear molecule, 3N-6 for a nonlinear molecule where the N is the number of atoms of the molecule. The strength of such transition is governed by the transition dipole moment of the molecule which is derived from the change in the static dipole of the molecule and the vibrational selection rule, i.e. $\Delta v = \pm 1$ under harmonic approximation.

2.2 Molecular Interaction with the Electric Field.

The molecular wavefunction of an isolated molecule can be expanded in the basis of eigenstates of the Hamiltonian as:

$$|\psi\rangle = \sum_n C_n |n\rangle \tag{2.2}$$

where the coefficient C_n is the probability amplitude of the $|n\rangle$ eigenstate and the wavefunction evolves according to the time-dependent Schrodinger equation,

$$i\hbar \frac{\partial}{\partial t}|\psi\rangle = \hat{H}(t)|\psi\rangle \tag{2.3}$$

In the absence of the laser field, the molecular Hamiltonian is time-independent, $\hat{H}_0|n\rangle = E_n|n\rangle$, and the solution of the wavefunction becomes:

$$|\psi\rangle = \sum_n C_n e^{-iE_n t/\hbar}|n\rangle \tag{2.4}$$

However, when the molecule interacts with a time-dependent electric filed, the total Hamiltonian of the system can be represented as a summation of time-independent Hamiltonian, $\hat{H}_0$, and the time-dependent interaction term, $\hat{U}(t)$:

$$\hat{H}(t) = \hat{H}_0 + \hat{U}(t) \tag{2.5}$$

The molecular interaction with the electric field is considered to be semi-classical where the electric field is treated classically while vibrational energy states treated quantum mechanically. Within these limits, the time-dependent interaction potential term is defined as:

$$\widehat{U}(t) = -\hat{\mu}E(t) \tag{2.6}$$

where the $\hat{\mu}$ and $E(t)$ are the dipole moment of the molecule and electric field of the laser, respectively. When the laser field is interacting with the molecule, the total Hamiltonian is time-dependent and the coefficients in equation (2.4) become time-dependent as well. The time dependency of these coefficients can be obtained by substituting equation (2.4) and (2.5) into equation(2.3),

$$\frac{\partial}{\partial t}C_m(t) = -\frac{i}{\hbar}\sum_n C_n(t)e^{-i(E_n-E_m)t/\hbar}\langle m|\widehat{U}(t)|n\rangle \tag{2.7}$$

where a numerical approach is required to obtain each coefficient when using ultrashort laser fields. This results in the molecule being in a linear combination of eigenstates, which is governed by the amplitude of the coefficients upon the molecular-field interaction. The characteristic time evolution of the generated linear coherent superposition is called the molecular response, $R(t)$, and contains the information about the molecule system under study.

2.3 Macroscopic Polarization

In condensed phase systems, more than a single molecule interacts with the electric field under the area of the laser beam, which are initially in phase with the oscillation of the field. This results in a macroscopic polarization in the sample due to the nonequilibrium charge distribution, which proportional to the $R(t)$. Since the molecules couple with electric filed through the interaction potential term, equation(2.6), the macroscopic polarization of the sample is calculated as the expectation value of the transition dipole,

$$P(t) \equiv \langle \mu \rangle = \langle \psi^*(t) | \hat{\mu} | \psi(t) \rangle$$

$$= \sum_m C_m \sum_n C_n \langle m | \hat{\mu} | n \rangle$$

$$= \sum_{mn} C_m^* C_n \mu_{mn} \tag{2.8}$$

where the μ_{mn} is the transition dipole moment of the vibrational transitions from m to n states.

2.4 Density Matrix Treatment

In order to avoid the mathematical complexity of deriving wavefunction for each molecule that interacts with the electric field, a simpler mathematical description is required. To this end, the density matrix of a pure state, which is defined for a single wavefunction as:

$$\rho = |\psi\rangle\langle\psi| \tag{2.9}$$

in which the matrix elements are $\rho_{mn} = C_m^* C_n$. Therefore, the macroscopic polarization, equation (2.8), becomes the trace of the multiplication of the density matrix and the dipole operator,

$$P(t) = \sum_{mn} \rho_{mn} \mu_{mn} = Tr(\hat{\rho}\hat{\mu}) \tag{2.10}$$

The time evolution of the density matrix is described by the Liouville-von Neumann equations, which can be derived by differentiating equation (2.9) and substitute the time evolution of the wavefunction from the Schrodinger Equation,(2.3):

$$\frac{d}{dt}\rho = -\frac{i}{\hbar}\left[\hat{H}, \rho\right] \tag{2.11}$$

where the Hamiltonian acts on both sides of the density matrix and is represented by the commutator. The solution to the equation (2.11) gives the time dependence of each element in the density matrix,

$$\rho_{nn}(t) = C_n^2 = \text{const.}$$

$$\rho_{nm}(t) = \pm\frac{i}{\hbar} C_n C_m e^{\pm i\omega_{nm}t} \tag{2.12}$$

where the ω_{nm} is the energy difference between the state n and m.

The density matrix treatment of a pure state can be extended to describe an ensemble of molecules that interacts with the electric field, with the help of a statistical description,

$$\rho = \sum_s A_s |\psi_s\rangle\langle\psi_s| \tag{2.13}$$

where the A_s is the probability of a molecule being in the state $|\psi_s\rangle$ and $A_s \geq 0$ and $\sum_s A_s = 1$. However, the time dependence of the density matrix now results in an additional term compared to equation (2.11), which arises from the Statistical Mechanics and results in dephasing and population relaxations.

$$\frac{d}{dt}\rho_{nm} = \sum_s \frac{dA_s}{dt} C_n C_m^* - \frac{i}{\hbar}\left[\hat{H}, \rho\right]_{nm} \tag{2.14}$$

where the first term that describes the homogeneous dephasing and population relaxation will be discussed phenomenologically later in this chapter. However, the homogeneous dephasing results in an additional term in anti-diagonal elements in the density matrix,

$$\rho_{nm}(t) = \pm\frac{i}{\hbar} C_n C_m e^{\pm i\omega_{nm}t} e^{-\frac{t}{T_2}} \tag{2.15}$$

Nevertheless, the equation (2.14) describes the time dependence of a density matrix of an ensemble of molecules analogs to the Schrodinger equation that describes the time dependence of a wavefunction.

2.5 Interaction Picture

The interactions between the molecules and the electric field are considered to be weak compared to the molecular internal interactions. Thus the perturbation caused by the field changes

only the coefficients of the wavefunction, not the eigenstates. In order to separate the time evolution caused by the field from the time evolution of molecular Hamiltonian in the absence of the field, the interaction picture is introduced,

$$|\psi(t)\rangle \equiv e^{-\frac{i}{\hbar}\hat{H}_0(t-t_0)}|\psi_I(t)\rangle \tag{2.16}$$

where the $e^{-\frac{i}{\hbar}\hat{H}_0(t-t_0)}$ describes the time evolution of the wavefunction in the absence of laser field whereas $|\psi_I(t)\rangle$ contains the dynamics caused by the field. A similar approach can be used to obtain the density matrix in the Interaction picture:

$$|\psi(t)\rangle\langle\psi(t)| \equiv e^{-\frac{i}{\hbar}\hat{H}_0(t-t_0)}|\psi_I(t)\rangle\langle\psi_I(t)|e^{+\frac{i}{\hbar}\hat{H}_0(t-t_0)}$$

$$\rho(t) \equiv e^{-\frac{i}{\hbar}\hat{H}_0(t-t_0)}\rho_I(t)e^{+\frac{i}{\hbar}\hat{H}_0(t-t_0)} \tag{2.17}$$

The time dependency of the density matrix is derived from the Liouville-von Neumann equations, equation (2.11):

$$\frac{d}{dt}\rho_I(t) = -\frac{i}{\hbar}\left[\hat{U}_I(t), \rho_I(t)\right] \tag{2.18}$$

where the interaction potential term is defined as $\hat{U}_I(t) = e^{+\frac{i}{\hbar}\hat{H}_0(t-t_0)}\hat{U}(t)e^{-\frac{i}{\hbar}\hat{H}_0(t-t_0)}$. The integration of equation (2.18) over the time gives the time-dependent density matrix in the Interaction picture,

$$\rho_I(t) = \rho_I(t_0) - \frac{i}{\hbar}\int_{t_0}^{t} d\tau \left[\hat{U}_I(\tau), \rho_I(\tau)\right] \tag{2.19}$$

where the t_0 is an arbitrary time origin. The perturbative expansion of the density matrix is obtained by solving the equation (2.19) iteratively,

$$\rho_I(t) = \rho_I(t_0) + \sum_{n=1}^{\infty} \left(-\frac{i}{\hbar}\right)^n \int_{t_0}^{t} d\tau_n \int_{t_0}^{\tau_n} d\tau_{n-1} \dots \int_{t_0}^{\tau_2} d\tau_1$$

$$[\widehat{U}_I(\tau_n), [\widehat{U}_I(\tau_{n-1}), \dots [\widehat{U}_I(\tau_1), \rho_I(t_0)] \dots]] \qquad (2.20)$$

Now the expanded density matrix in the interaction picture can be transformed into the Schrodinger picture according to equation(2.17),

$$\rho(t) = \rho^{(0)}(t) + \sum_{n=1}^{\infty} \left(-\frac{i}{\hbar}\right)^n \int_{t_0}^{t} d\tau_n \int_{t_0}^{\tau_n} d\tau_{n-1} \dots \int_{t_0}^{\tau_2} d\tau_1$$

$$e^{-\frac{i}{\hbar}\widehat{H}_0(t-t_0)}[\widehat{U}_I(\tau_n), [\widehat{U}_I(\tau_{n-1}), \dots [\widehat{U}_I(\tau_1), \rho(t_0)] \dots]]e^{+\frac{i}{\hbar}\widehat{H}_0(t-t_0)}$$

$$= \rho^{(0)}(t) + \sum_{n=1}^{\infty} \rho^{(n)}(t) \qquad (2.21)$$

where the $\rho^{(0)}$ and $\rho^{(n)}$ are the zeroth and nth-order density matrix. The zeroth-order density matrix represents the time evolution of the system without the molecule-filed interactions while the nth-order includes the molecule-field interaction in power of $\widehat{U}_I$. Furthermore, the nth-order density matrix can be expanded according to equation (2.6),

$$\rho^{(n)}(t) = -\left(-\frac{i}{\hbar}\right)^n \int_{t_0}^{t} d\tau_n \int_{t_0}^{\tau_n} d\tau_{n-1} \dots \int_{t_0}^{\tau_2} d\tau_1 \, E(\tau_n)E(\tau_{n-1}) \dots E(\tau_1)$$

$$e^{-\frac{i}{\hbar}\widehat{H}_0(t-t_0)}[\hat{\mu}_I(\tau_n), [\hat{\mu}_I(\tau_{n-1}), \dots [\hat{\mu}_I(\tau_1), \rho(t_0)] \dots]]e^{+\frac{i}{\hbar}\widehat{H}_0(t-t_0)} \qquad (2.22)$$

note that the dipole operator is still in the Interaction picture where $\hat{\mu}_I = e^{+\frac{i}{\hbar}\widehat{H}_0(t-t_0)}\hat{\mu}e^{-\frac{i}{\hbar}\widehat{H}_0(t-t_0)}$. Moreover, the dipole operator is time-dependent in the Interaction picture while time-independent in the Schrodinger picture.

2.6 Nonlinear Polarization and Response Function

As discussed in equation (2.10), the nth-order macroscopic polarization can be calculated as the expectation value of the multiplication of the dipole operator and nth-order density matrix. Hence, the nth-order polarization becomes,

$$P^{(n)}(t) = -\left(-\frac{i}{\hbar}\right)^n \int_{t_0}^{t} d\tau_n \int_{t_0}^{\tau_n} d\tau_{n-1} \dots \int_{t_0}^{\tau_2} d\tau_1 \, E(\tau_n)E(\tau_{n-1}) \dots E(\tau_1)$$

$$\langle \hat{\mu}_I(t)[\hat{\mu}_I(\tau_n), [\hat{\mu}_I(\tau_{n-1}), \dots [\hat{\mu}_I(\tau_1), \rho(t_0)] \dots]]\rangle \tag{2.23}$$

It is more convenient to use time interval between each interaction rather than absolute time,

$$\tau_1 = 0, t_1 = \tau_2 - \tau_1, t_2 = \tau_3 - \tau_2 \dots, t_n = t - \tau_{n-1} \tag{2.24}$$

Therefore, the n[th]-order polarization can be rewritten as,

$$P^{(n)}(t) = -\left(-\frac{i}{\hbar}\right)^n \int_0^{\infty} dt_n \int_0^{\infty} dt_{n-1} \dots \int_0^{\infty} dt_1$$

$$E(t - t_n)E(t - t_n - t_{n-11}) \dots E(t - t_n - t_{n-1} - \dots - t_1)$$

$$\langle \hat{\mu}(t_n + t_{n-1} + \dots + t_1)[\hat{\mu}(t_{n-1} + \dots + t_1), \dots [\hat{\mu}(0), \rho(-\infty)] \dots]\rangle \tag{2.25}$$

The interaction picture subscription of the dipole operator is neglected due to the obvious time dependence of the dipole operator. Moreover, the time of the initial density matrix is set to negative infinity due to the system being at equilibrium before interacts with the electric field. The last term of the above equation is the so-called nth-order response function,

$$R^{(n)}(t_n \dots . t_1) = -\left(-\frac{i}{\hbar}\right)^n \langle \hat{\mu}(t_n + t_{n-1} + \dots + t_1)[\hat{\mu}(t_{n-1} + \dots + t_1),$$

$$\dots [\hat{\mu}(0), \rho(-\infty)] \dots]\rangle \tag{2.26}$$

2.7 Propagation of the Density Matrix

The first-order response function can be deduced from the equation (2.26), and the commutator expansion gives,

$$R^{(1)}(t_1) \propto -i\langle\hat{\mu}(t_1)[\hat{\mu}(0), \rho(-\infty)]\rangle$$

$$R^{(1)}(t_1) \propto i\langle\hat{\mu}(t_1)\hat{\mu}(0)\rho(-\infty)\rangle - i\langle\rho(-\infty)\hat{\mu}(0)\hat{\mu}(t_1)\rangle \tag{2.27}$$

where the invariance of the trace under cyclic permutation is used for the rearrangement. It is clear from the above equation that the dipole operator acts on both sides of the density matrix. The density matrix for a two-level system which is in the ground state can be expressed as:

$$\rho(-\infty) = \begin{pmatrix} 1 & 0 \\ 0 & 0 \end{pmatrix} \tag{2.28}$$

The transition dipole operator is chosen to be anti-diagonal to create a coherent superposition between the ground and the first excited state after the first molecule-field interaction.

$$\mu = \begin{pmatrix} 0 & \mu_{01} \\ \mu_{01} & 0 \end{pmatrix} \tag{2.29}$$

Therefore, after the first interaction with the density matrix, the system is in a coherence state,

$$i\hat{\mu}(0)\rho(-\infty) = \begin{pmatrix} 0 & 0 \\ i\mu_{01} & 0 \end{pmatrix} \tag{2.30}$$

After the first interaction, the system evolves according to the system Hamiltonian as described in equation (2.15) and the coherence state is oscillating at the fundamental frequency between the two states along with the homogeneous dephasing term,

$$i\hat{\mu}(0)\rho(-\infty) = \begin{pmatrix} 0 & 0 \\ i\mu_{01}e^{-i\omega_{01}t_1}e^{-t/T_2} & 0 \end{pmatrix} \tag{2.31}$$

Then after t_1 time, the second transition dipole operator acts on equation (2.31) and the system is back to the population state,

$$i\hat{\mu}(t_1)\hat{\mu}(0)\rho(-\infty) = \begin{pmatrix} i\mu_{01}^2 e^{-i\omega_{01}t_1}e^{-t_1/T_2} & 0 \\ 0 & 0 \end{pmatrix} \quad (2.32)$$

The same method can be applied to the other pathway, $i\langle\rho(-\infty)\hat{\mu}(0)\hat{\mu}(t_1)\rangle$, and show it is the complex conjugate of equation (2.32). Therefore, they are often represented by $R^{(1)}(t) = R_1 + R_1^*$.

2.8 Rotating Wave Approximation

According to equation (2.25) and (2.32), the first order polarization is,

$$P^{(1)}(t) = \frac{i}{\hbar}\mu_{01}^2 \int_0^\infty dt_1 E(t-t_1)e^{-i\omega_{01}t_1} \quad (2.33)$$

The electric field can be mathematically expressed as negative and positive frequencies:

$$2E^0(t)\cos(\omega t) = E^0(t)\left(e^{-i\omega t} + e^{+i\omega t}\right) = E(t) + E^*(t) \quad (2.34)$$

Substitution of the electric field in equation (2.33) yields four integration terms,

$$P^{(1)}(t) = \frac{i}{\hbar}\mu_{01}^2 e^{-i\omega t}\int_0^\infty dt_1 E(t-t_1)e^{-t_1/T_2} + \frac{i}{\hbar}\mu_{01}^2 e^{+i\omega t}\int_0^\infty dt_1 E(t-t_1)e^{-t_1/T_2}e^{-2i\omega_{01}t_1} \quad (2.35)$$

The latter term oscillates at a much higher rate than the first term. Hence, the integration of highly oscillating terms over time is negligible compared to others. This is called rotating wave approximation and it is a useful tool to identify the term of the electric field, which acts on the density matrix along with the transition dipole, that creates the coherence.

2.9 Phase Matching Direction

The electric field consists of wavevector, $\vec{k}$, and phase, ϕ, of the field in addition to the carrier frequency,ω,

$$E(t) = E^0(t)\cos\left(\vec{k}.\vec{r} - \omega t + \phi\right) \quad (2.36)$$

The negative and positive frequencies have opposite wavevectors and phase, i.e. $E(t) \propto e^{i(-\omega t+\phi+\vec{k}.\vec{r})}$ vs $E^*(t) \propto e^{i(+\omega t-\phi-\vec{k}.\vec{r})}$. Therefore, when the rotating wave approximation is applied to a pathway, it will not only select the possible pathways but also distinguish the surviving pathways. The phase matching direction method is very useful to separate pathways that result in more than one electric field interactions. More details about phase matching selection will be discussed in the third-order nonlinear spectroscopy section.

2.10 Feynman Diagram

The previous section showed that each field-density matrix interaction creates a non-zero element in the density matrix and stores the information about the system. However, tracking each non-zero element for higher-order response functions is challenging. The expansion of the commutator in the n[th]-order response function yields 2^n number of terms and each term has its own time propagation. In order to simplify each interaction on the density matrix, a new representation (Feynman diagrams) is introduced.[145]

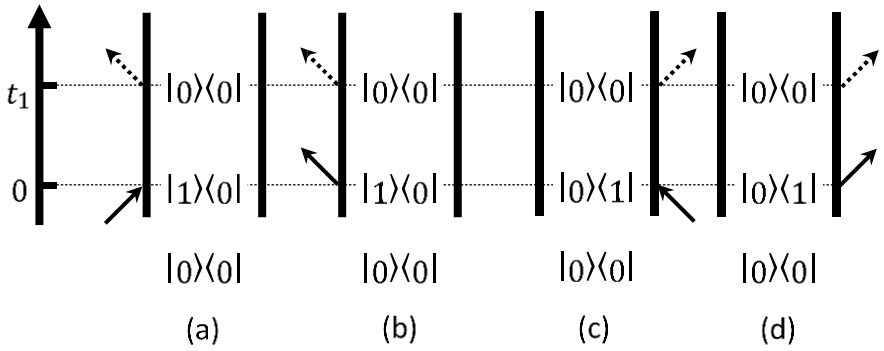

Figure 2.1 Feynman diagrams that represent the first order response function.

In Feynman diagrams, the two verticals lines represent the time propagation from bottom to top and the left line is the time evolution of left side (ket) of the density matrix while the right corresponds to time evolution of right side (bra) of the density matrix. Each interaction is represented by an arrow and the direction of the arrow is determined by the term of the electric

field, i.e. $E'(t)$ is pointing right $(+\vec{k})$ and $E'^{*}(t)$ is pointing left $(-\vec{k})$. The last interaction is a result of calculating the polarization through the trace and has the direction along the sum of the directions of the incident fields, $\vec{k}_{sig} = \sum_s \vec{k}_s$. Hence, it is marked with a dashed arrow. The sign of the diagram is determined by the number of interactions on the right side, i.e. $(-1)^n$.

The possible Feynman diagrams are shown in Figure 2.1. The first diagram shows that the system is initially at the population state, $\rho(-\infty) \rightarrow |0\rangle\langle 0|$, before any interaction with the field. The system is promoted to a (10) coherence state upon the first interaction. Note that the arrow is pointed right, hence, $E'(t)$ acted on the density matrix. Then the system returns to the initial population state. Therefore, the first diagram corresponds to $i\langle\hat{\mu}(t_1)\hat{\mu}(0)\rho(-\infty)\rangle E'(t)$. The other three diagrams represent the rest of the possible pathways that described in equation (2.35). However, in reality, the diagram (a) and (c) survive from the rotating wave approximation.

2.11 Linear Spectroscopy

In linear spectroscopy, a first-order macroscopic polarization is generated after the field-molecular interactions. The first-order response function and the first-order polarization were derived in the previous sections. According to Maxwell's equations, the generated microscopic polarization emits an $\pi/2$ phase shifted electric field with respect to the polarization.[146, 147]

$$E_{sig}^{(n)}(t) \propto iP^{(n)}(t) \tag{2.37}$$

The direction of the emitted field lies in the same direction as the initial electric field since there is only one interaction with the electric field. Therefore, the emitted field interferes with the source field. The interference is then captured using square-law detectors that can only measure the intensity of the signal. The signal can be captured in time-domain or frequency-domain. The time-domain signals need to be Fourier transformed to obtain the spectrum. However, the spectrum

can be directly obtained by placing a spectrometer before the detector in which the Fourier transformation is performed experimentally.

$$S(\omega) \propto \left| \int_0^\infty dt \left(E(t) + E_{sig}(t) \right) e^{i\omega t} \right|^2$$

$$\sim I_0(\omega) + 2\Re \left(E(\omega).E_{sig}(\omega) \right) \tag{2.38}$$

where the $I_0(\omega) = \lfloor E(t) \rfloor^2$ which is the intensity of the laser. $I_{sig}(\omega) = \left| E_{sig}(t) \right|^2$ is neglected due to the small contribution compared to the other two terms. In linear spectroscopy, the spectrum of the source is subtracted in order to separate the interference term. In this type of experiments, the interference is said to be self-heterodyned because the same source field is responsible for the E_{sig} and interference on the detector. More details about the lineshape of the linear spectroscopy will be discussed in a later section.

2.12 Third-order Nonlinear Spectroscopy

The third-order response function can be deduced from equation (2.26),

$$R^{(3)}(t_1, t_2, t_3) \propto \langle \mu(t_1 + t_2 + t_3), [\hat{\mu}(t_2 + t_1), [\hat{\mu}(t_1), [\hat{\mu}(0), \rho(-\infty)]]] \rangle \tag{2.39}$$

The expansion of the commutator reveals eight different pathways that can be arranged as four pairs of complex conjugates. However, an additional two pairs of complex conjugates are possible since the ability of third interaction to access the (21) coherence after (11) population state. The corresponding Feynman diagrams are shown in Figure 2.2 (the complex conjugates are not shown),

All the Feynman diagrams start from the (00) population states and are promoted to either (10) or (01) coherence state after the first interaction. In the case of an inhomogeneous system, initially, molecules start oscillating with their intrinsic frequencies and evolve according to their molecular Hamiltonians until t_1, which leads to a decay in the response function due to the

frequencies become out of phase. Then the second interaction move or return the system to (11) or (00) population states, respectively. Upon the interaction with the third electric field, the top three diagrams in Figure 2.2 switch the system to opposite side coherence states of the density matrix while the bottom three move to coherence states that are on the same side of the density matrix. Therefore, the sign of the time evolution after the third interaction is reversed for the top row. Hence, if an inhomogeneous system is present, the initial oscillation of each molecule reappears at $t_3 = t_1$, thus the maximum polarization of the system. Consequently, the top three diagrams are called "rephasing pulse sequence". However, the bottom Feynman diagrams do not experience such an event. Hence, they are called a "non-rephasing pulse sequence".

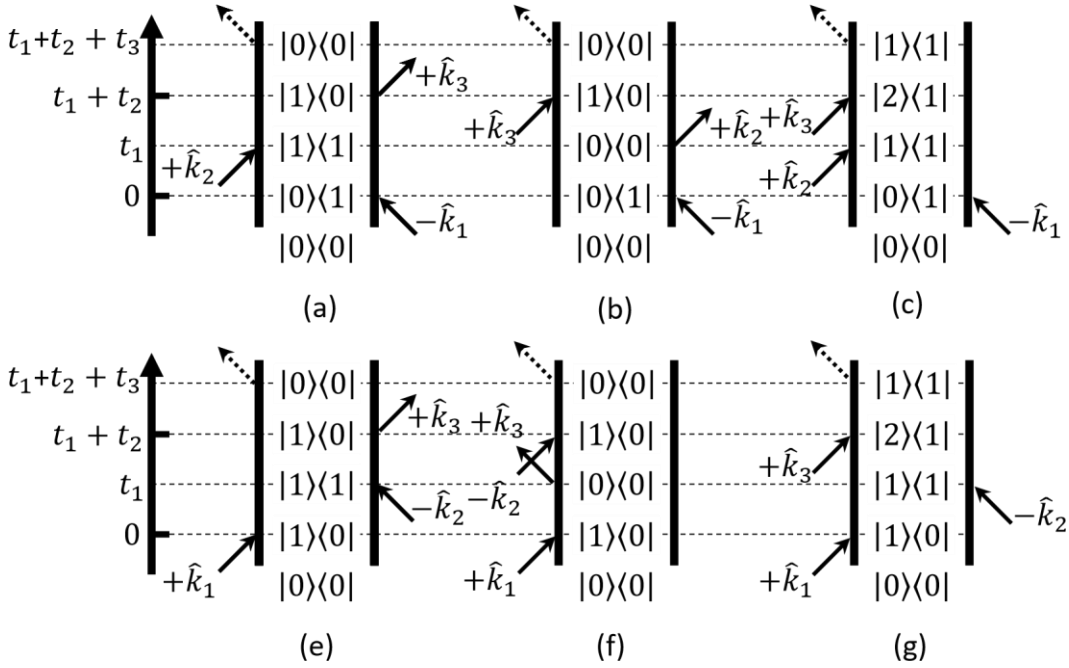

Figure 2.2 Six Feynman diagrams that result from the third-order response function.

In an inhomogeneous system, the transition frequency in each response function becomes a convolution of a Gaussian distribution,

$$R_{rephase} \propto \int e^{-i\omega_{01}(t_3-t_1)} e^{\frac{-(\omega_{01}-\overline{\omega_{01}})^2}{2\Delta\omega^2}} d\omega_{01}$$

$$\propto i e^{-i\omega_{01}(t_3-t_1)} e^{-\Delta\omega^2(t_3-t_1)^2}$$

$$R_{non-rephase} \propto \int d\omega_0 e^{\frac{-(\omega_{01}-\overline{\omega_{01}})^2}{2\Delta\omega^2}} e^{-i\omega_{01}(t_3+t_1)}$$

$$\propto i e^{-i\omega_{01}(t_3+t_1)} e^{-\Delta\omega^2(t_3+t_1)^2} \qquad (2.40)$$

In this case, the second term of the rephasing response function creates an envelope which has a maximum when $t_3 = t_1$. Both rephasing and non-rephasing will result in a third-order macroscopic polarization and according to equation (2.37), an electric field is emitted from the sample. The electric field emission due to the recurrence of the macroscopic polarization at $t_3 = t_1$ is called "photon echo" emission.

The full form of the third-order nonlinear polarization can be deduced from equation (2.25),

$$P^{(3)}_{rep}(t) \propto e^{i(-k_1+k_2+k_3)} e^{i(-\phi_1+\phi_2+\phi_3)} \int_0^\infty dt_3 \int_0^\infty dt_2 \int_0^\infty dt_1 E_3(t-t_3).$$

$$. E_2(t-t_3-t_2). E_1^*(t-t_3-t_2-t_1) R_{rep}(t_3,t_2,t_1)$$

$$P^{(3)}_{non-rep}(t) \propto e^{i(k_1-k_2+k_3)} e^{i(\phi_1-\phi_2+\phi_3)} \int_0^\infty dt_3 \int_0^\infty dt_2 \int_0^\infty dt_1 E_3(t-t_3).$$

$$. E_2^*(t-t_3-t_2). E_1(t-t_3-t_2-t_1) R_{non-rep}(t_3,t_2,t_1) \qquad (2.41)$$

The phase matching rule indicates that the direction of the emitted electric field due to the rephasing and non-rephasing polarization are along $-k_1 + k_2 + k_3$ and $+k_1 - k_2 + k_3$, respectively. Therefore, placing two detectors in each direction is used to differentiate the rephasing and non-rephasing signals. An alternative method is to use a single detector with a change of time ordering of each pulse. However, either rephasing or non-rephasing can not be further separated into individual pathways rather measured as a summation.

$$R_{rep}(t_3, t_2, t_1) = 2i\mu_{01}^4\left(e^{-i\omega_{10}(t_3-t_1)} - e^{-i\left((\omega_{01}-\Delta)t_3-\omega_{01}t_1\right)}\right)e^{-(t_1+t_3)/T_2}$$

$$R_{non-rep}(t_3, t_2, t_1) = 2i\mu_{01}^4\left(e^{-i\omega_{10}(t_3+t_1)} - e^{-i\left((\omega_{01}-\Delta)t_3+\omega_{01}t_1\right)}\right)e^{-(t_1+t_3)/T_2} \quad (2.42)$$

where the $\Delta = \omega_{01} - \omega_{12}$ and the $\mu_{12} = \sqrt{2}\mu_{01}$ assumption is made.[145]

The electric fields that result in equation (2.41) are complex values. The real part contains the absorptive spectrum while the imaginary part contains the dispersive spectrum. The most effective way to obtain the purely absorptive spectrum is to combine rephasing and non-rephasing spectrum and calculate the real part since the dispersive part of rephasing and non-rephasing spectra carry the opposite sign and cancel out. Therefore, it is essential to collect both rephasing and non-rephasing spectra to obtain the 2DIR spectrum.

2.12.1 Pump-probe Spectroscopy

Pump-probe spectroscopy is another third-order nonlinear spectroscopy in which a third-order macroscopic polarization is created in the same way described in the previous section. However, in pump-probe spectroscopy, the dephasing of the coherence state during t_1 is zero since the pump pulse acts as both $\vec{k}_1$ and $\vec{k}_2$. Therefore, the same Feynman diagrams shown in Figure 2.2 can be used to describe the pump-probe spectroscopy. The $\vec{k}_1$ and $\vec{k}_2$ are replaced with $\vec{k}_{pu}$ and $-\vec{k}_{pu}$, and $\vec{k}_3$ with $\vec{k}_{pr}$ since the emitted field follows the same direction as the probe pulse. The response functions for stimulated emission and bleach is essentially the same and excited state absorption oscillates with a different frequency,

$$R_{S.E}(t_1, t_2, t_3) \propto i\mu_{10}^4 e^{-i\omega_{01}t_3} e^{-t_3/T_2}$$

$$R_{E.A}(t_1, t_2, t_3) \propto i\mu_{10}^2\mu_{12}^2 e^{-i\omega_{12}t_3} e^{-t_3/T_2} \quad (2.43)$$

2.13 Lineshape Function

Phenomenologically introduced homogeneous dephasing term in equation (2.15) will be discussed in more detail in this section. As discussed in the previous section, molecules in the ensemble have individual frequencies when an inhomogeneous system is present. However, these frequencies are usually not static with time in the liquid phase systems due to fluctuations in the surroundings. Therefore, the time evolution of a coherence state in an ensemble is,

$$\rho_{01}(t) \propto \langle e^{-i\int_0^t \omega_{01}(\tau)d\tau} \rangle \tag{2.44}$$

The time dependence of the frequency is disentangled with a mean frequency and time-dependent fluctuation which average to zero, $\omega_{10}(t) = \omega_{10} + \delta\omega_{10}(t)$ and $\langle \delta\omega_{10}(t) \rangle = 0$. Now the equation (2.44) becomes,

$$\rho_{01}(t) \propto e^{-i\omega_{10}} \langle e^{-i\int_0^t \delta\omega_{01}(\tau)d\tau} \rangle \tag{2.45}$$

The ensemble average of the frequency fluctuation, which was phenomenologically introduced as e^{-t/T_2} in equation (2.15), can be expanded in powers of $\delta\omega_{01}$,

$$\langle e^{-i\int_0^t \delta\omega_{01}(\tau)d\tau} \rangle \equiv e^{-g(t)} = 1 - (g_1(t) + g_2(t) + \cdots) + \frac{1}{2}(g_1(t) + g_2(t) + \cdots)^2 + \cdots \tag{2.46}$$

where $g_n(t)$ represent the order function of ${\delta\omega_{10}}^n$. Similarly, for a frequency distribution of a Gaussian profile, the ensemble average of the frequency fluctuation can be evaluated using the cumulant expansion up to the second-order and the lineshape function is deduced as,

$$g(t) = \int_0^t \int_0^{\tau'} d\tau' d\tau \langle \delta\omega_{10}(\tau)\delta\omega_{10}(0) \rangle \tag{2.47}$$

where the $\langle \delta\omega_{10}(\tau)\delta\omega_{10}(0) \rangle$ is called "frequency-frequency correlation function" (FFCF) which describes the correlation of the frequency at a given time to the initial frequency. Therefore, FFCF

essentially reveals the characteristics of the fluctuations of the environment of the vibrational probe.

According to Kubo's stochastic lineshape theory,[148] the FFCF can be deduced to an exponential decay function,

$$\langle \delta\omega_{10}(t)\delta\omega_{10}(0)\rangle = \Delta\omega^2 e^{\frac{-t}{\tau_c}} \tag{2.48}$$

where the $\Delta\omega^2$ and τ_c are the fluctuation amplitude and characteristic time of the fluctuation, respectively. The solution of equation (2.47) after substitution of equation (2.48),

$$g(t) = \Delta\omega^2\tau_c^2\left[e^{-\frac{t}{\tau_c}} + \frac{t}{\tau_c} - 1\right] \tag{2.49}$$

In the limits of fast or small fluctuation, the homogeneous limit, i.e. $\Delta\omega.\tau_c \lll 1$, the lineshape function becomes,

$$g(t) = \Delta\omega^2\tau_c t = \frac{t}{T_2^*} \tag{2.50}$$

where the $T_2^* = 1/\Delta\omega^2\tau_c$. This will result in a narrowing of the frequency distribution in the spectrum. On the other hand, in the inhomogeneous limit, i.e. $\Delta\omega.\tau_c \lll 1$, the lineshape function becomes independent of the characteristic time of the fluctuations,

$$g(t) = \frac{\Delta\omega^2}{2}t^2 \tag{2.51}$$

Now the spectrum mimics the frequency distribution of the system. The systems under investigation in the following chapters are in between the homogeneous and inhomogeneous limits. Hence, the linear spectra become Voight profiles, a convolution of Gaussian and Lorentzian profiles.

The same treatment can be extended to the 2DIR lineshape, where the response functions become,

$$R_{repha} \propto 2i\mu_{01}^4\left(e^{-i\omega_{01}(t_3-t_1)} - e^{-i\left((\omega_{01}-\Delta)t_3-\omega_{01}t_1\right)}\right) \cdot e^{-g(t_1)+g(t_2)-g(t_3)-g(t_1+t_2)-g(t_2+t_3)+g(t_1+t_2+t_3)}$$

$$R_{non-repha} \propto 2i\mu_{01}^4\left(e^{-i\omega_{01}(t_3+t_1)} - e^{-i\left((\omega_{01}-\Delta)t_3+\omega_{01}t_1\right)}\right) \cdot e^{-g(t_1)-g(t_2)-g(t_3)+g(t_1+t_2)+g(t_2+t_3)-g(t_1+t_2+t_3)} \quad (2.52)$$

where the lineshape function is the same as discussed above, i.e. double integration of the FFCF. The memory of the initial frequencies fade away with the t_2 population time. Hence, the 2DIR spectra, which elongated along the diagonal line at early t_2 time will become rounder shape as the t_2 population time increases. This is the so-called spectral diffusion process. There are many ways to extract the FFCF from a series of 2DIR spectra, but mainly, tracking the spectral diffusion via the nodal line slope or the central line slope methods are convenient.[149, 150]

2.14 Experimental Setup

2.14.1 Generation of Ultrashort Pulses

One of the main requirements of conducting time-resolved spectroscopy is to generate ultrashort laser pulses at the desired wavelength, typically on the order of 100 fs. Currently, obtaining such a series of laser pulses is straightforward due to the commercially available laser systems, which are usually compact in size and produce very stable pulses. In our lab, we use a Spectra-Physics Spitfire Ace regenerative amplifier, which is pumped by a Spectra-Physics Empower Q-switched laser (Nd:YLF), to amplify the seed laser pulses generated from Spectra-Physics Mai Tai (Ti:saphire). The amplification is achieved by chirped pulse amplification method, Figure 2.3. The initial seed pulses with a central frequency of ~800 nm at 80 MHz repetition rate are stretched in time to reduce the peak power and then regeneratively amplify using Ti:Sapphire cavity, which is pumped by the Q-switched laser tuned to 527 nm. The amplified high power pulses are selectively directed at a 5 kHz repetition rate to the compressor to recompress

the pulses to the original duration. The output pulses are centered at ~800 nm with ~50 fs pulse width and 5 kHz repetition rate.

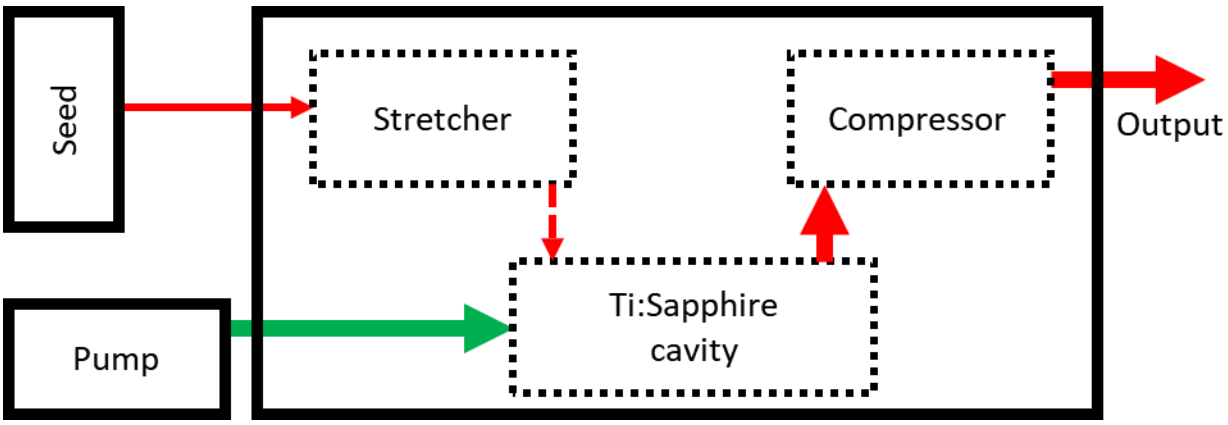

Figure 2.3. Schematic of ultrashort pulse generation.

2.14.2 Optical Parametric Amplification

The commercially available laser systems have a limited range of wavelengths, especially in IR or mid-IR regions. In order to access the desired part of the spectrum, different types of wave mixing techniques are used in the field. The required beam configurations for the wave mixing is achieved using optical parametric amplifiers (OPA). In our lab, we use a Spectra-Physics OPA 800CF amplifier to generate the signal and idler for the difference frequency generation.

The optical layout of the OPA is shown in Figure 2.4. Initially, ~4% of the 800 nm beam is reflected through a sapphire while light plate to generate the white light continuum. A ~15% of the remaining 800 nm beam is seeded with the white light on a beta barium borate (BBO) crystal on the pre-amplification stage. The temporal overlap of the beams is controlled by a delay stage on the white light path. The generated signal is blocked with a dichroic mirror and, the generated idler and the remaining pump are combined and passed through the BBO crystal again. Another delay stage is used to control the temporal overlap of the pump and the idler. Finally, a dichroic beam splitter is used to separate the output signal and idler from the residual pump. The output

signal and idler range from 1.1 μm to 1.6 μm and 1.6 μm to 3.0 μm, respectively. The desired wavelengths of the signal and idler are achieved by changing the angle of the BBO crystal. The output power depends on the tuned wavelength but usually in the order of μJ pulse energy.

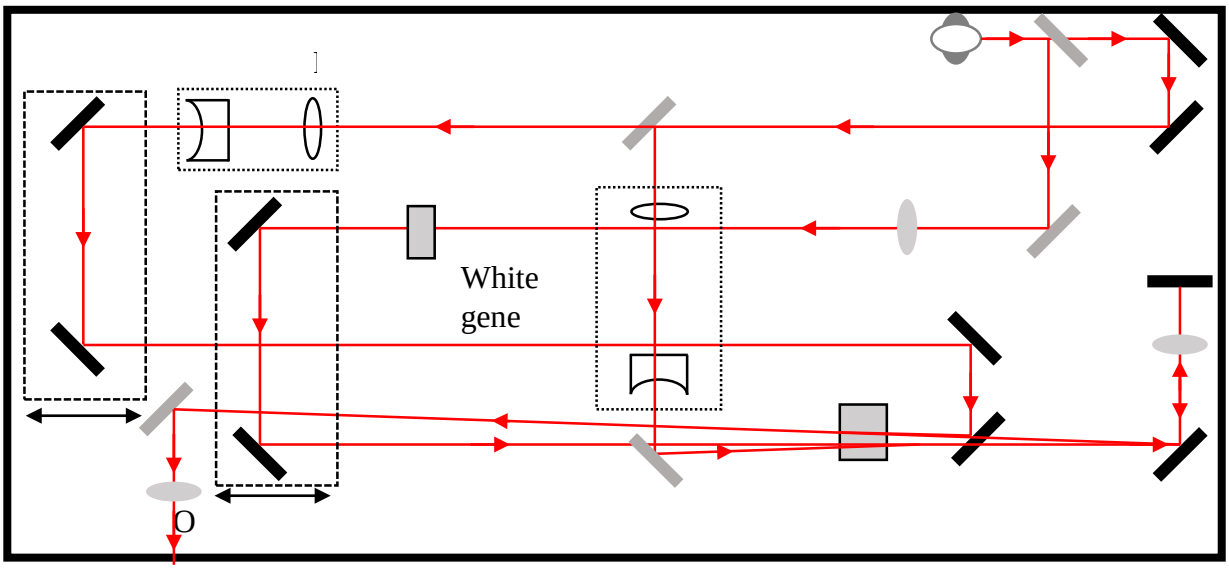

Figure 2.4. Schematic of the optical parametric amplifier.

2.14.3 Generation of Ultrafast Femtosecond Infrared Pulses

The desired IR spectrum is obtained by difference frequency mixing (DFG) technique, where the generated signal and idler are used.[151] Before the DFG step, the signal and idler are separated using a dichroic beam splitter and recombined on the same beam splitter after passed through a delay stage. The separation and recombination help to increase the stability and reduce the noise.[152] A DFG crystal ($AgGaS_2$) is placed close to the focus of the recombined signal and idler to generate the IR pulses ranging from 3 μm to 10 μm with pulse energy ranging from 1 μJ to 10 μJ. The residual signal and idler are filtered using germanium filters before IR pulses enter the 2DIR setup with parallel polarization.

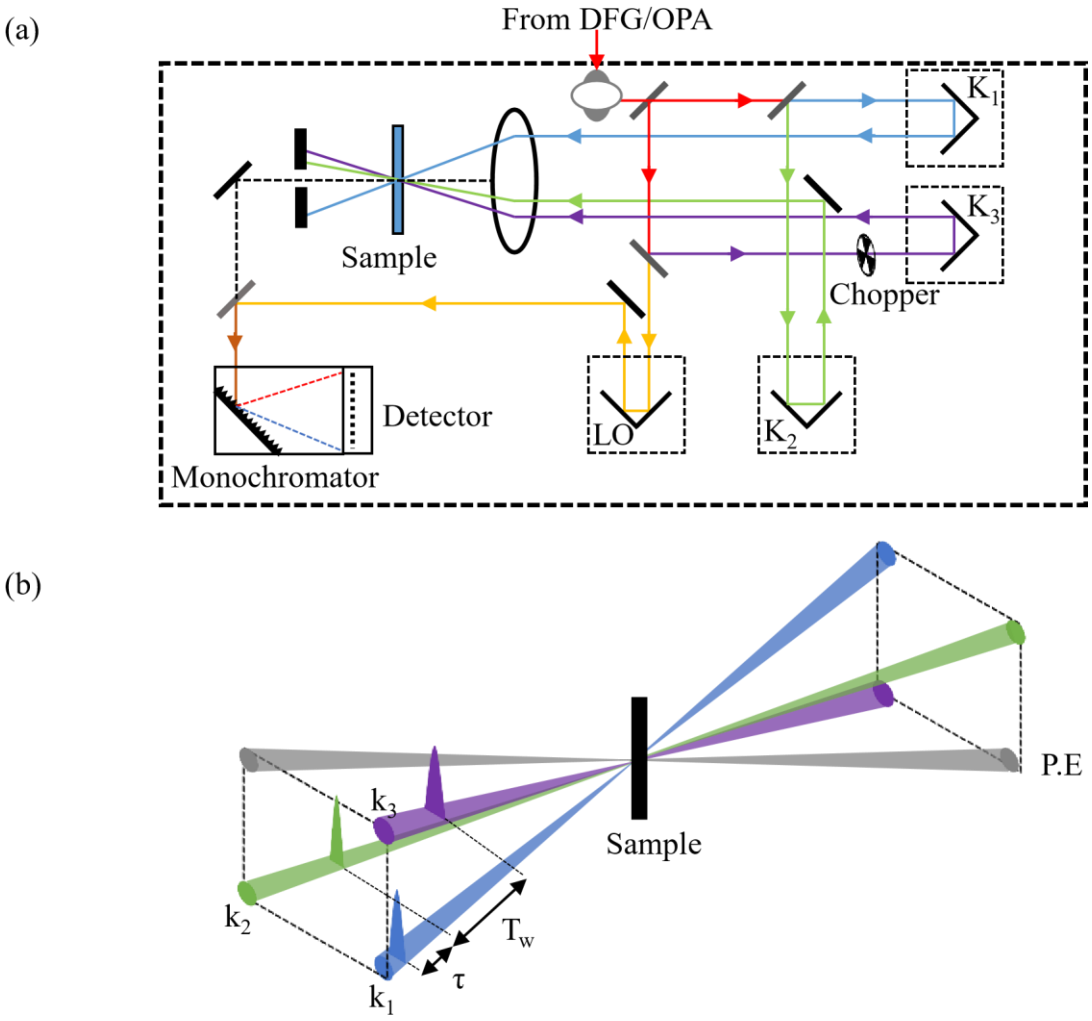

Figure 2.5. Schematic diagram of 2DIR setup and pulse sequence in boxcar configuration.

2.14.4 2DIR setup

The generated IR beam is then split into four identical pulses using 50/50 beam splitters and each is directed through a computer controlled translation stage, Figure 2.5. Three of these beams are focused on the sample with the BOXCARS configuration[145] using a convex lens and the directions are set at $\vec{k}_1$, $\vec{k}_2$and $\vec{k}_3$. Hence the photon echo will be emitted in the phase matching direction of $\vec{k}_1 + \vec{k}_2 + \vec{k}_3$ with <XXXX> polarization. The generated photon echo is heterodyned with the fourth pulse, local oscillator. Then the heterodyned signal is captured by a liquid-nitrogen

cooled 64 elements mercury cadmium telluride (MCT) detector after dispersed by a monochromator. Subsequently, the detected signal is amplified and digitized.

2.14.5 Sample Preparation and Time-zero

The sample is pressed between a pair of 2 mm CaF_2 windows and an identical sample cell that consists of water is prepared to find the time-zero between three pulses. The transient grating (TG) method is used to determine the time-zero of the three pulses to ensure the precise time overlap between each pulse.[153] In the TG method, two pulses create a transient grating on the water, and the delayed third pulse diffracted along the same direction as P.E and heterodyned with L.O. Hence, the relative time-zero of two pulses is determined by achieving the maximum transient grating.

2.14.6 Data Acquisition

The initial data is measured as a function of a wavelength λ_t and two time variables, τ and T_w. The λ_t is the detection frequency axis of the 2DIR spectrum where the monochromator performs the Fourier transform along the P.E and L.O time axis. The τ and T_w are the time intervals between pulse one and two, and pulse two and three, respectively. For each 2DIR spectrum, the τ is scanned at a fixed T_w. The detector captures the heterodyned signal as intensities,

$$S(\omega_t, \tau, T_w) = |E_{P.E}(t) + E_{L.O}|^2$$
$$\sim |E_{L.O}|^2 + 2.E_{P.E}(t).E_{L.O}^* \quad (2.53)$$

where the $E_{P.E}(t)$ and $E_{L.O}$ are the electric fields of the photon echo and local oscillator respectively. The $|E_{L.O}|^2$ is not time dependent and only provides an offset for the detected signal. Therefore, to separate the second term from the signal, a mechanical chopper is placed on the path of $\vec{k}_3$, which block the beam at half laser pulse repetition rate, and subtract the contribution from

the L.O. Both the rephasing and non-rephasing spectra are collected by scanning the τ from negative times to positive times for each waiting time.

2.14.7 Analysis of Data

As mentioned earlier, the raw data is a function of a wavelength and two time variables. First, the raw data is numerically back Fourier transformed to the time domain to obtain the signal as a function of three time variables, $S(t, \tau, T_w)$. Thereafter, the signal is double Fourier transformed along t and τ times to create the two frequency axes of the spectrum for a given T_w, $S(\omega_\tau, \omega_t, T_w)$. The same treatment is performed on both rephasing and non-rephasing raw data. The phase mismatch between rephasing and non-rephasing is corrected before combine them to obtain the pure absorptive spectrum.[154]

2.15 Pump-probe Setup

The pump-probe experiment setup is rather simpler compared to 2DIR. The layout is shown in Figure 2.6. Initially, the IR pulses are split into a weak probe pulse and a strong pump pulse using a beam splitter. Both the pump and probe pulses are focused on the sample using a parabolic mirror and the pump pulse is blocked after the sample using an iris aperture. The probe pulse passes through a delay stage which controls the waiting time between the pump and probe pulses. The separated probe pulse is directed to a monochromator and then dispersed on to liquid-nitrogen cooled MCT detector. The polarization of pulses is controlled to extend the use of pump-probe experiments to measure the anisotropy. The polarization of the probe pulse is set to 45° with respect to the pump pulse before the sample. Another polarizer is placed before the monochromator to select the parallel or perpendicular polarization contribution of the signal.

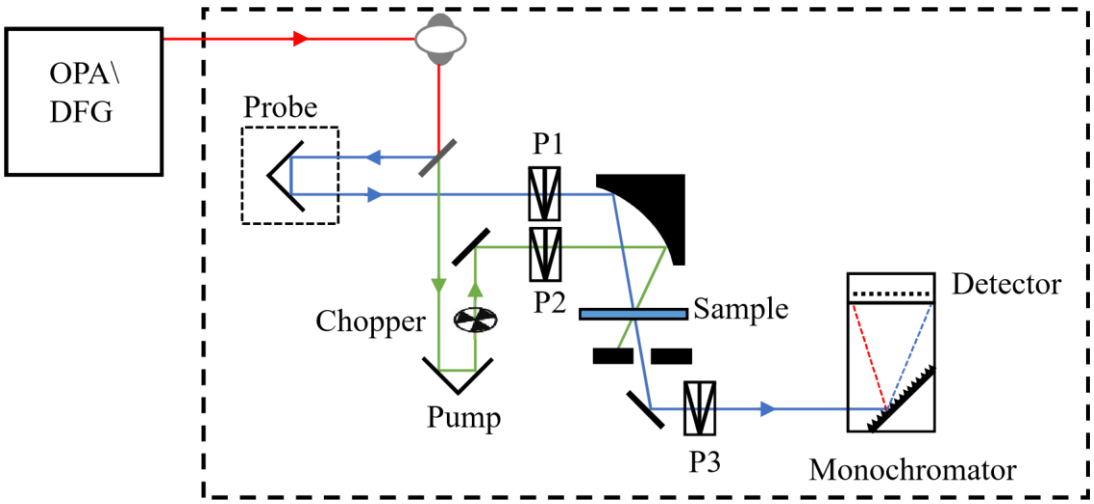

Figure 2.6. Schematic of the pump-probe setup.

The data is collected in a similar manner to 2DIR data acquisition. The signal is heterodyned with the probe pulse itself and the monochromator performs the experimental Fourier transform. Hence the interference term is the same as the result of equation (2.53). However, the absorption spectrum is defined by,

$$\Delta A(\lambda, T_w) = -\log \frac{I_{sig}(\lambda)}{I_0(\lambda)} = -\log \frac{I_{pumped}(\lambda)}{I_{unpumped}(\lambda)} \tag{2.54}$$

Therefore, the ratio between the intensities of pumped and un-pumped probe pulse separates the signal. A mechanical chopper that is synchronized at half the repetition rate of the laser is placed to block the pump beam on every other pulse. Thus, the pump-probe signal is directly obtained without further analysis of raw data.

The anisotropy decay experiments are performed in the same as described above but the pump-probe spectra are collected at both parallel and perpendicular polarizations. Further, raw data analysis is required since the anisotropy is defined as,

$$r(t) = \frac{\left(\Delta A_{para}(T_w) - \Delta A_{perp}(T_w)\right)}{\left(\Delta A_{para}(T_w) + 2\Delta A_{perp}(T_w)\right)} \tag{2.55}$$

Where the $\Delta A_{para}(T_w)$ and $\Delta A_{perp}(T_w)$ are the pump-probe spectra collected for a given waiting time at parallel and perpendicular polarizations, respectively.

2.16 Summary

This chapter described the origin of the macroscopic polarization that results from molecular-field interactions. The response function which contains the information of the system was derived using the time dependent Liouville-von Neumann equation. The first order and third-order response functions were deduced and represented with corresponding Feynman diagrams. The 2DIR and pump-probe experiments were discussed as applications of the nonlinear response function or macroscopic. Finally, the experimental approach of the 2dir and pump-probe experiments was discussed in detail.

CHAPTER 3. MOLECULAR STRUCTURE AND ULTRAFAST DYNAMICS OF SODIUM THIOCYANATE ION PAIRS FORMED IN GLYMES OF DIFFERENT LENGTH*

3.1 Introduction

The development of alternative energy sources has arisen recently due to the price and availability of fossil fuels as well as the environmental concerns from their use. Many countries and regions already have increased the use of renewable sources for supplying power to the electric grid.[155] However, these energy resources, mainly wind and photovoltaic, are intermittent and require additional energy storage systems to operate continuously. Lithium ion batteries (LIBs) are now the energy storage of choice in a wide range of fields including mobile devices and electric automobiles.[19, 156, 157] However, the implementation of LIBs in large scale energy storages worldwide has major drawbacks related to the price and the availability of lithium.[25, 158] Thus, sodium-based batteries have been suggested as substitutes to large scale storage systems despite the known limitations, such as its low energy density compared to LIBs.[25]

Sodium ion batteries (SIBs) share the same working characteristics as LIBs, including their ability to work at room temperature. While SIBs have lower energy density compared to LIBs,[25] the cost of building large scale SIBs is expected to be lower than LIBs due to the high abundance of sodium salts.[45] Therefore, the development of operational SIBs has gained more traction for application in large scale energy storage.[40, 159] The realization of fully functional SIBs has not been achieved yet due to some major challenges in their conception. One of the main problems arises from the finding of compatible electrochemical cell materials.[67] For example, conventional graphite electrodes cannot be used as the anode material with organic carbonate-based electrolytes

* This chapter was previously published as Molecular structure and ultrafast dynamics of sodium thiocyanate ion pairs formed in glymes of different lengths. S. R. Galle Kankanamge and D. G. Kuroda, Phys. Chem. Chem. Phys., 2019, 21, 833 and reprinted by the permission of The Royal Society of Chemistry

since the sodium ion does not intercalate in them.[160-163] The lack of intercalation is postulated to arise from the weaker Na-C interaction compared to other alkali metals.[164-167] In contrast, the intercalation process occurs in graphite anodes if the sodium electrolyte is composed primarily of glycol ethers (glymes), because co-intercalation phenomenon occurs in which the solvent molecules is never expelled from the solvation shell of the sodium (ternary intercalation).[67, 168] Moreover, it has been observed that the co-intercalation process is dependent on the size of the glyme molecules.[61, 168] The glyme length effect on the intercalation process has been attributed to the different interactions between glymes and sodium.[61, 168]

Until today, few reports have investigated the structure and interactions of sodium-ion electrolytes at the molecular level.[64, 65, 169] In particular, the number of studies dedicated to investigate the atomistic structure and its relation to the macroscopic properties of ether-based sodium ion electrolytes are very scarce. Previously, it was demonstrated that sodium ion is coordinated with 6 oxygens in sodium triflate/glyme systems, as expected from the known octahedral geometry of the sodium-ion solvation shell.[65, 170] Furthermore, the same studies showed that the ion association between sodium and triflate ions is non-monotonic as a function of glyme chain length despite the observation of increasing in the chelation with the length of the glyme.[65, 170] These results are also supported by a NMR study, which also demonstrated the strong ion association between the sodium and triflate ions in glymes.[171] Lately, it has been reported that the presence of ion-pairs give rise to non-vehicular transport in glyme-based electrolytes due to fast ion-pair making and breaking.[172] Finally, another study has shown the suitable electrochemical stability of glyme-base electrolytes for SIBs.[173] Therefore, the association of sodium ions in these systems is likely to play an important role in terms of the transportation properties and the stability

of the electrolyte. Thus, the knowledge of the ion pair structure and dynamics in glymes is crucial for rationalizing the observed properties.

In this work, we investigated the structure and motions associated with the ion pairs in glyme-based solvents using both infrared spectroscopic techniques and theoretical methods. In order to study the solvation shell structure of the sodium ion in glymes, sodium thiocyanate (NaSCN) was used since the anion is a relatively small ion that can easily be accommodated within the structure of the chelated sodium ion. In addition, thiocyanate anion has been previously used to investigate the motions and dynamics of different systems because its nitrile group (CN) is good reporter of the molecular environment.[135, 141, 174] Here, the effects of the glyme length on the structure and dynamics of the sodium thiocyanate are characterized. To obtain a molecular picture of the processes occurring in the different solutions, our experimental findings are successfully described by a stochastic model comprising a harmonic oscillator with restricted motions.

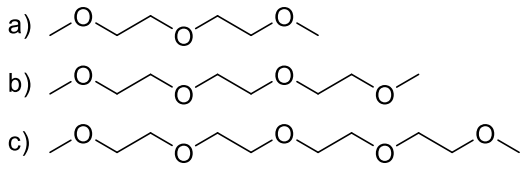

Scheme 3.1. Chemical structures of G2, (a), G3, (b), and G4, (c).

3.2 Methodology

Diglyme (G2, $(CH_3)_2[CH_2CH_2O]_2O$, >99%) and tetraglyme, (G4, $(CH_3)_2[CH_2CH_2O]_4O$, >99%) were obtained from Acros Organics and triglyme (G3, $(CH3)_2[CH_2CH_2O]_3O$, >99%) was obtained from Alfa Aesar. Tetrabutlyammonium thiocyanate (TBASCN, $C_{17}H_{36}N_2S$, >95%) was obtained from TCI chemicals and sodium thiocyanate (NaSCN, >98%) was obtained from Sigma Aldrich and dried at 70°C for 24 hours before use. All other chemicals were used without further purification. Solutions of 0.5M and 1.5M of NaSCN in glymes were prepared by simply mixing

the components inside a N_2 filled glovebox at room temperature. Note that all the samples have optical densities below 0.3 in the investigated region of the IR spectrum; i.e., 2000-2100 cm^{-1}.

3.2.1 Linear IR Spectroscopy

Fourier transform infrared (FTIR) experiments were performed using a Bruker Tensor 27 spectrometer with 0.5 cm^{-1} resolution and liquid nitrogen cooled narrow band MCT detector. The samples were measured in transmission mode. All the samples were prepared inside the N_2 filled glovebox using a transmission cell (Harrick Scientific) with a pair of 2 mm calcium fluoride windows without a spacer. Each FTIR spectrum was recorded as an average of 40 individual scans. All samples were measured at 25 °C.

3.2.2 Two dimensional IR spectroscopy

Two dimensional infrared experiments were performed using the standard boxcar configuration and heterodyne detection.[145] Briefly, a Ti:Sapphire amplifier (Spectra Physics Mai Tai and Spitfire) with a 5 kHz repletion rate was coupled to an optical parametric amplifier (Spectra Physics, 800C) to produce 60 fs broadband infrared pulses. The generated pulses were split into three identical pulses ($\mathbf{k}_1$, $\mathbf{k}_2$ and $\mathbf{k}_3$) and later focused on the sample with a boxcar configuration.[145] The time intervals: τ (time between the first pulse and the second pulse), T_w (time between the second and the third pulse) and t (time between the third pulse and the photon echo) were controlled with four computer controlled translational stages (PI Micos). The generated photo echo with pulses with parallel polarization (<XXXX>) in the phase matching direction ($-\mathbf{k}_1+\mathbf{k}_2+\mathbf{k}_3$) was heterodyned with a fourth pulse (local oscillator) and later dispersed by a Triax monochromator. Finally, the non-linear signal was detected with a liquid nitrogen cooled 64 element MCT array detector (Infrared Systems Developments). Spectra were collected for T_w from 0 to 100 ps with 21 steps. For each T_w, rephasing and non-rephasing were collected by scanning τ from -4 ps to 4 ps

in every 5 fs step. The local oscillator always preceded the photon echo signal by ~0.7 ps. To obtain each 2D-IR spectrum, the photon echo signal was transformed from (τ, T_W, t) to (ω_τ, T_W, ω_t) via a double Fourier transform along τ and t, while keeping T_W as a parameter. A detailed explanation of the Fourier analysis used to generate the 2DIR spectra can be found in Ref. [175].

3.2.3 Pump probe spectroscopy

The frequency selective pump-probe experiments were performed as follows. Broadband infrared pulses were generated with optical parametric amplifier (Spectra Physics, 800C) from the 800nm pulses generated by Ti:Sapphire amplifier (Spectra Physics Mai Tai and Spitfire) at 5 KHz repletion rate. The 60 fs IR pulses with a vertical polarization were split into a weak probe pulse and a strong pump pulse. The pump and probe beams were focused onto the sample using a parabolic mirror. While the pump beam was dumped with an iris aperture, the probe beam was recollimated using another parabolic mirror and detected with a liquid nitrogen cooled 64 element MCT array detector (Infrared Systems Developments) after being dispersed by a monochromator (SpectraPro 150). In this experiment, the probe polarization was set at 45° with respect to the pump using a polarizer before the sample. To obtain the pump-probe signal at different polarizations, the detected probe polarization was adjusted with polarizer directly after the sample. The time delay between the pump and probe pulses was controlled with a translation stage. The pump-probe signal was collected from -4 ps to 100 ps in 1 ps intervals for the first 10 ps, and followed by 5 ps intervals. The anisotropy of each sample was computed from the different polarized selective pump probe experiments as: $r(t) = [I_{\parallel}(t) - I_{\perp}(t)]/[I_{\parallel}(t) + 2I_{\perp}(t)]$, where $I_{\parallel}$(t) and $I_{\perp}$(t) are the pump-probe signals measured for parallel and perpendicular polarization between the pump and probe, respectively.

3.2.4 Density Functional Theory Calculations

Density functional theory (DFT) calculations were performed using the Gaussian 09 software and the 6-311++G** basis set was used at B3LYP level of theory.[176] One sodium ion and one thiocyanate ion were geometrically optimized with two glyme molecules for G2. The initial complex was built using the Avogadro software with MMFF94 force field.

3.2.5 Theoretical simulation

The stochastic motions of thiocyanate ion were modeled using MATLAB software. The model simulates the restricted rotational diffusion of an axially symmetric particle.[177] To this end, the simulation assumes that the axially symmetric particle can be represented by a sphere tethered to a point in space with a spring that obeys Langevin dynamics.[177] In addition, to produce the wobbling-in-cone, the particle is assumed to be moving in a potential (V_θ) such that the rotation is free within the cone ($V_\theta = 0$) and forbidden outside the cone ($V_\theta = \infty$).[177] A spring constant, $1/\delta$, determines the fluctuation of the sphere within the cone. The complete dimensionless algorithmic solution of the Langevin equation, expressed in Ref. [177], was used to generate the recursive Cartesian coordinates of the nitrogen atom of the thiocyanate ion.

A unit vector along the CN bond was used to represent the direction of the transition dipole ($\hat{\boldsymbol{\mu}}$) at a given time. The anisotropy of thiocyanate ion was calculated using:

$$r(t) = 0.4\langle P_2(\hat{\mu}_0 . \hat{\mu}_t)\rangle \qquad (3.1)$$

where $\hat{\boldsymbol{\mu}}_0$ and $\hat{\boldsymbol{\mu}}_t$ are the transition dipole at t=0 and t=*t*, respectively, and P_2 is the second order Legendre polynomial. The frequency-frequency correlation function (FFCF) was calculated from the instantaneous frequencies. The instantaneous frequencies were derived from the simulated coordinates and a frequency map derived by Choi et al.[178] In the frequency calculation, it was assumed that the fluctuation of the frequency are caused exclusively by motions of the

sodium ion. Note that the position of the sodium ion was obtained from the DFT geometry of the complex and it was assumed to be fixed. In addition, the calculation of the instantaneous frequency only considered the Z components of the frequency map since the parameters along the Z axis are much larger than those of the other two axes.[178] Each simulation was computed for t = 2500 steps with $\Delta t = 1x10^{-3}$ times steps. All the results were calculated as an ensemble average of 50,000 simulations.

3.3 Results

The structure and motions of thiocyanate ion pairs in glymes were first investigated via linear IR spectroscopy. The IR studies focused on the strong CN stretch of the thiocyanate ion (extinction coefficient of 21 ± 2 $mM^{-1}.cm^{-1}$ in D_2O)[179] located in the 2000-2100 cm^{-1} IR region. The IR spectra of NaSCN in each glyme (Figure 3.1) shows a major peak centered at ~2060 cm^{-1}, which is fairly symmetric.

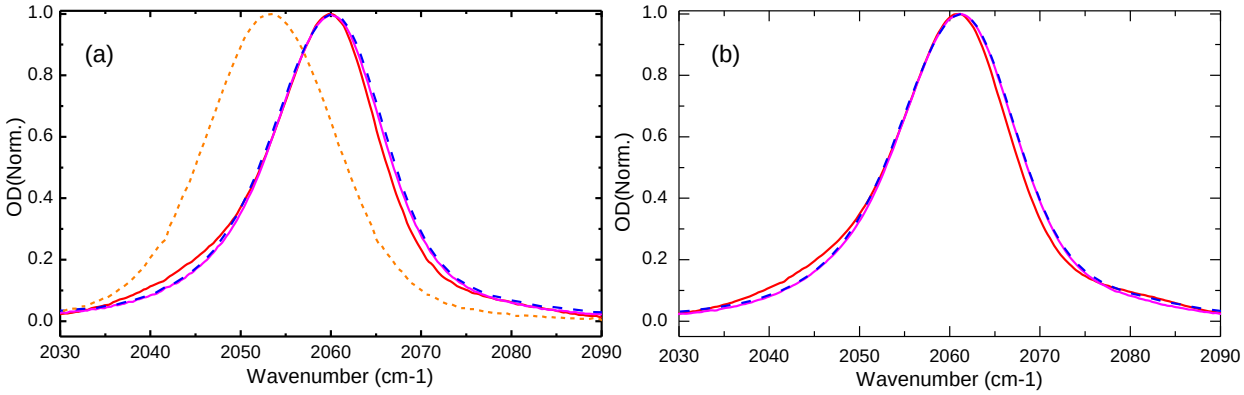

Figure 3.1. Solvent subtracted FTIR spectra of 0.5M NaSCN in different glymes, G2 (red solid line), G3 (magenta solid) and G4 (dashed blue) in the range of 2020 cm^{-1} to 2100 cm^{-1}. The dashed orange line corresponds to TBASCN in G2. The right graph shows the 1.5M NaSCN in each glymes with the same representation.

Moreover, no major differences are observed among the positions and shapes of the CN stretch bands of the thiocyanate ion in the three different glymes, albeit the presence of small shoulder on the low frequency side of the G2 sample, which is not seen in the other two glymes

(G3 and G4). In addition, the CN stretch band contains a small high frequency peak (~2080 cm^{-1}) which is barely noticeable in 0.5M NaSCN solutions, but is evident at high concentration solutions, Figure 3.1. The tetrabutylammonium (TBA) thiocyanate is used to mimic the free ion since it has been reported that the presence of the TBA cation does not significantly perturb the anion.[180] The IR spectrum of CN stretch band of TBASCN exhibits a symmetric peak centered at ~2053 cm^{-1}, which is downshifted by ~7 cm^{-1} from the corresponding peak for the sodium salt (Figure 3.1). The difference in the frequency location between thiocyanate ion from sodium and TBA salts evidences the formation of ion pairs in the former.

The dynamics and motions of the thiocyanate ion were investigated via 2DIR spectroscopy. Figure 3.2 shows the 2DIR spectra at different waiting times (T_W) in different solvents. In the 2DIR spectra, the red (positive) peaks located at [ω_τ, ω_t = ~2060 cm^{-1}, ~2060 cm^{-1}] represent the transitions between ν=0 and ν=1 vibrational states, and blue (negative) peaks centered at [ω_τ, ω_t = ~2060 cm^{-1}, ~2035 cm^{-1}] depict the transitions between ν=1 to ν=2 vibrational states.[145] The ~25 cm^{-1} downshift of the blue peak with respect to the red peak evidences the anharmonic nature of CN stretch potential of thiocyanate and is in agreement with the previous studies.[180] Similarly to the FTIR spectra of the different glyme solutions, the 2DIR spectra show analogous 2D spectra for all the samples, as seen by the location and shape of both the red and blue peaks. The waiting time evolution (T_W) of the spectra shows that the positive peak is tilted and elongated along the diagonal line (black line, ω_τ=ω_t) at T_W = 0 ps and becomes rounder and less tilted when the waiting time increases. The changes with waiting time of the shapes of the 2DIR spectral components demonstrates the loss of correlation between the pump (ω_t) and probe (ω_t) frequencies due to molecular motions of the solution components; i.e., spectral diffusion. In addition, it appears that the G2 sample presents small crosspeaks (see dashed circles in Figure 3.2) between the main peak

and the low frequency peak at longer waiting times. The presence of crosspeaks is likely to evidence the dynamics of making and breaking of ion pairs.[181-183] However, the relatively small intensity of the crosspeaks compared to the main peak hampers any possible characterization of the chemical exchange process in this system.

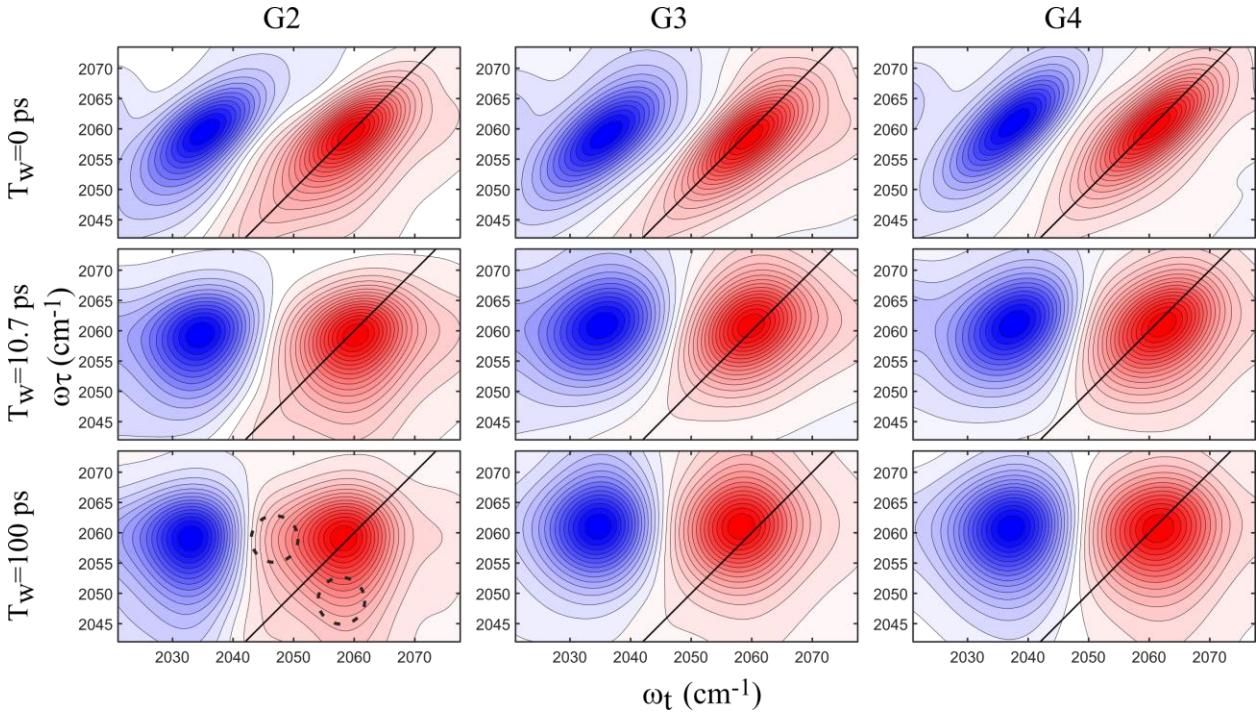

Figure 3.2. 2DIR spectra of 0.5M NaSCN in diglyme (G2), triglyme (G3) and tetraglyme (G4) at waiting time of 0 ps, 10.7 ps and 100 ps.

3.4 Discussion

The IR spectra show the presence a single peak in the CN stretch region indicating that the thiocyanate ion exists predominantly as a single species. The free thiocyanate band is determined from the IR spectrum of TBASCN (Figure 3.1) and found to be located at ~2054 cm^{-1} in all glymes. The observed band at 2060 cm^{-1} could arise from changes in the dielectric constant of the medium, but the concentration dependence shows a small shift on the order of a ~2 cm^{-1} for concentrations from 50 mM to 2.5 M. Thus, the shift in the vibrational frequency observed between sodium and TBA thiocyanate salts indicates that the majority of thiocyanate ions are present as ion pairs in all

the glymes. In addition, the spectra as function of concentration shows the rise of the another band located on the high frequency side (2074 cm^{-1}), which is assigned to the aggregates. The assignment of high frequency band to aggregates is consistent with a previous study in which was postulated the possibility of aggregation of thiocyanate ion with different metal ions.[184]

Table 3.1. The areas under each Voigt profiles are calculated and tabulated as a fraction of the total area under the peak.

Solvent	Free ion	Ion pair	Aggregate	FWHM of band
G2	0.34±0.04	0.64±0.04	0.030±0.003	13.7±0.6
G3	0.21±0.01	0.77±0.01	0.020±0.002	15.5±0.2
G4	0.23±0.01	0.75±0.01	0.020±0.002	15.9±0.2

The IR spectra were modeled with three Voigt profiles centered at 2054 cm^{-1}, 2060 cm^{-1} and 2074 cm^{-1} where each band represent free ion, ion-pairs, and aggregates, respectively. Modeling of the CN stretch reveals that more than 60% of the thiocyanate ions form ion pairs irrespective of the glyme. However, it also demonstrates that the G2 sample has a slightly lower amount of ion pairs compared to the other two glymes (Table 3.1). In addition, it shows that there are only very minor differences (less than 1 cm^{-1}) in the central vibrational frequencies of the ion pair peaks for each glyme. The similarity of the CN stretch central frequencies indicates that the interaction between the thiocyanate ion and sodium is very similar among glyme samples.[139, 141] Thus, it is likely that sodium and thiocyanate ions have a comparable average distance in all glymes because the separation between ions determines not only the averaged interaction energy between the pair, but also the averaged frequency of the nitrile stretch of the thiocyanate ion in the ion pair. This result is in agreement with a simulation study that showed that the average sodium to counter ion distance is similar for various glymes.[63] Finally, the full width half maxima (FWHM) for the

CN stretch bands are also very similar, though there is a very small difference in G2 sample (Table 3.1).

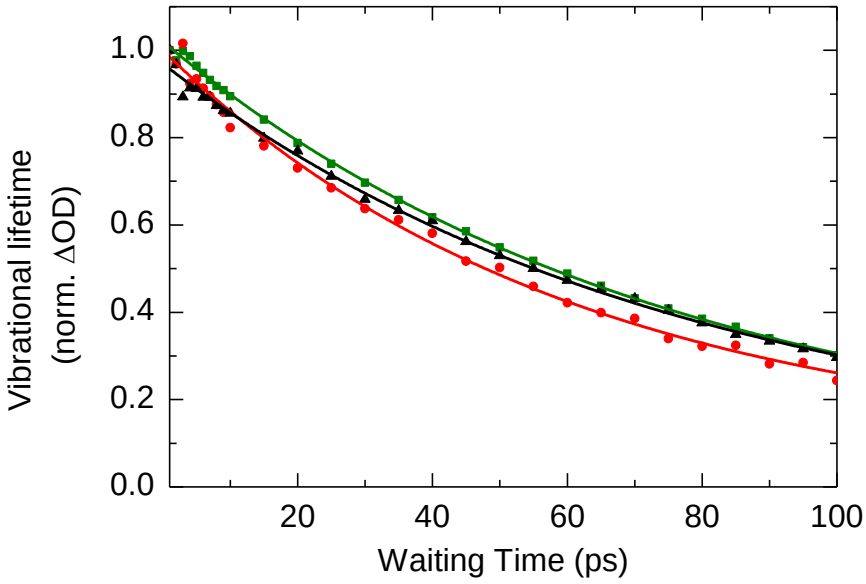

Figure 3.3. Measured vibrational lifetime of the 0.5M NaSCN in diglyme (green), triglyme (red) and tetraglyme (black).

It will be shown later in this study that the thermal motions of thiocyanate ion are responsible for the narrowing observed in the CN stretch band of the thiocyanate ion in G2 since the vibrational lifetime of this vibrational mode is very similar for all glymes, Figure 3.3, and comparable to those measured in aprotic solvents, such as acetone and dimethyl sulfoxide.[180]

The direct inspection of the 2DIR spectra reveal that there is no significant difference in the characteristic times of the frequency-frequency correlation function (FFCF) due to motions of the thiocyanate complex. For example, it appears that the positive peaks of all the samples start from elongated peaks along the diagonal and acquire a round shape at T_W=100 ps. The observation is indicative of comparable decorrelation dynamics in the three glyme samples. To characterize the dynamics of the thiocyanate ion in the ion pair, the FFCF is derived from the 2DIR using the central line slope method (CLS).[149] The CLS (Figure 3.4) shows a slight difference in the characteristic time scales of the FFCF since the CLS of G2 reaches a lower value at 100 ps when

compared to the other two samples. Note that the CLS does not change when measured at 2065 cm^{-1}, which correspond to ~5 cm^{-1} from the peak maximum. In addition, it is apparent that the FFCF consists of more than one component; i.e., one fast and one slow component which are more evident in log scale (Figure 3.4 inset). To obtain the characteristic time of the CLS, the curves are modeled following the standard Kubo formalism consisting of exponential functions.[185] In this particular case, a sum of two exponential functions is used to describe the CLS,

$$y = A_1 e^{-\frac{t}{\tau_1}} + A_2 e^{-\frac{t}{\tau_2}} \tag{3.2}$$

In Equation (3.2), A_n and τ_n represent the amplitudes and characteristic times of the n^{th} motions, respectively. The characteristic times derived from the modeling the CLS with Equation (3.2) are presented in Table 3.2.

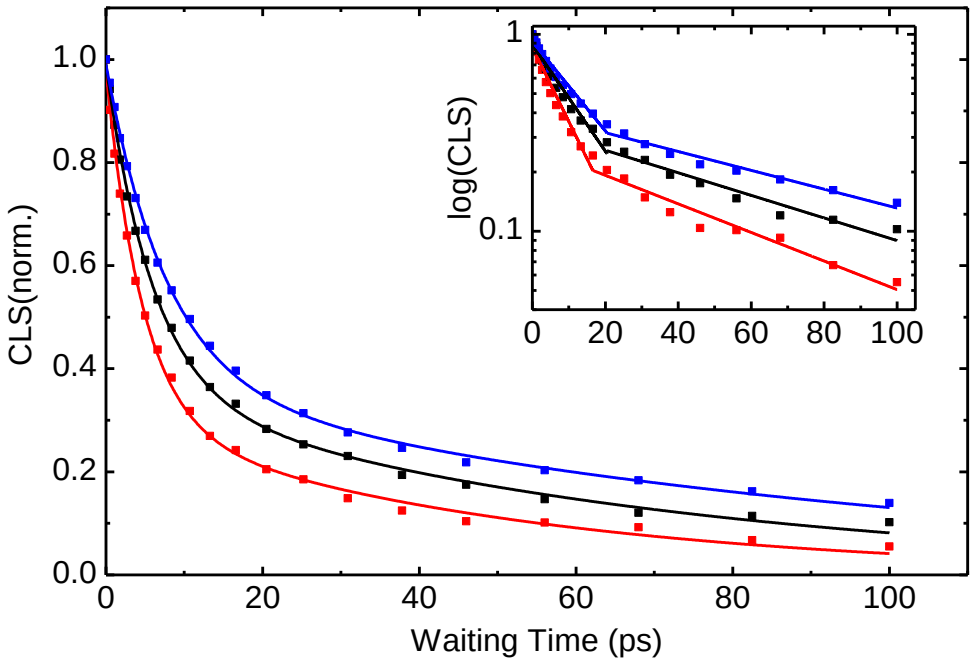

Figure 3.4. Waiting time evolution of the central line slope. Solid squares are the experimental CLS at each waiting time and the solid lines are the fitting curves with the double exponential function (Equation (3.2). Inset contains CLS in a log scale. Red, black, and blue squares correspond to 0.5M NaSCN in G2, G3, and G4, respectively.

The CLS modeling reveals a fast dynamical process on the order of a few picoseconds and a relatively slow dynamical process on the order of tenths of picoseconds. Interestingly, both the fast and the slow dynamics increase their characteristic times (slow down) as the glyme length is increased. While it is easy to assume that the motions of the glyme molecules produce the decays in the FFCF as observed in the CLS dynamics, it have been previously shown that the dynamics of the FFCF can be strongly affected by the molecular reorientation of the system.[186] To observe the degree of convolution between FFCF and reorientation dynamics, the anisotropy of the samples is determined.

Table 3.2. The characteristic times calculated for the experimental CLS (τ_1 and τ_2) and anisotropy (T_1 and T_2). The half cone angles (θ) of restricted diffusive motion of thiocyanate ion calculated using Equation (3.5). τ_{wc} and τ_r are characteristics times for restricted motion and complete reorientation.

Solvent	τ_1(ps)	τ_2(ps)	T_1(ps)	T_2(ps)	τ_{wc}(ps)	τ_r(ps)	θ°
Diglyme	4.6±0.2	51±5	7.5±0.8	114±8	8.0±0.9	114±8	33±1
Triglyme	6.0±0.3	68±5	9.0±0.9	162±13	10±1	162±13	31±1
Tetraglyme	7.8±0.3	95±6	7±1	152±13	7±1	152±13	27±1

The rotational reorientation dynamics observed via the experimental anisotropy reveals different dynamics for the different glymes samples. The anisotropy as function of waiting time were fitted with a biexponential function of the form:

$$y = B_1 e^{-\frac{t}{T_1}} + B_2 e^{-\frac{t}{T_2}} \tag{3.3}$$

where T_n and B_n are the characteristic rotational time scales and the amplitudes, respectively.

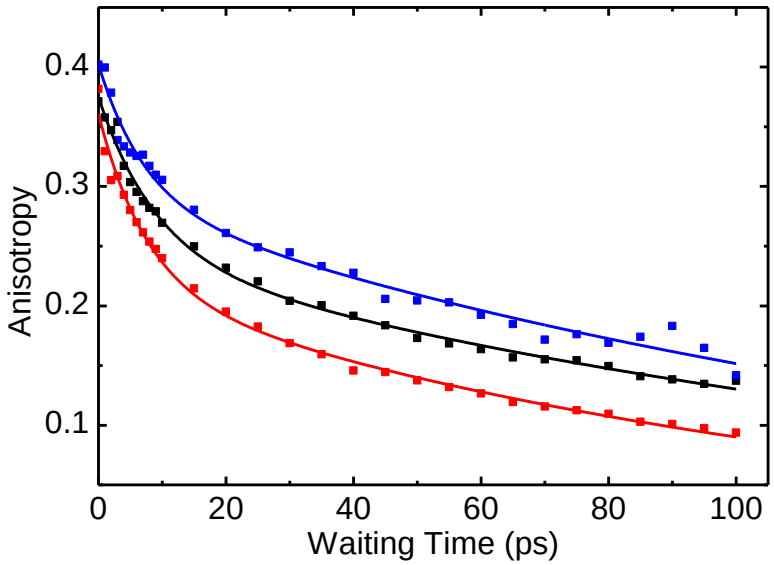

Figure 3.5. The experimental anisotropy at the new absorption band of 0.5M NaSCN in G2 (red squares), G3 (black squares) and G4 (blue squares). Solid lines represent the fitting curves with double exponential functions (Equation (3.3).

The characteristic times (Table 3.2) reveals two dynamical components, which do not show a clear correlation with the length of the glyme. However, the most interesting aspect of the anisotropy time evolution is its biexponential dynamics. While the presence of more than one anisotropy decay could be attributed to vibrational energy transfer among thiocyanate ions in an aggregate, dilution experiments (Figure 3.6) show that the lineshape of the nitrile stretch of thiocyanate is not significantly altered by dilution, which discard the presence of significant amount of aggregates. Thus, the biexponential decay of the anisotropy is interpreted in terms of restricted motions of the thiocyanate ion within the ion-pair complex. This model is consistent with the formation of ion pairs between thiocyanate and sodium ions, since the presence of the cation in the solvation shell of thiocyanate should limit its free rotation. In addition, the presence of glyme molecules chelating the sodium ion should slow down the 3D rotation of ion-pair complex and limit in-plane mobility of the anion.

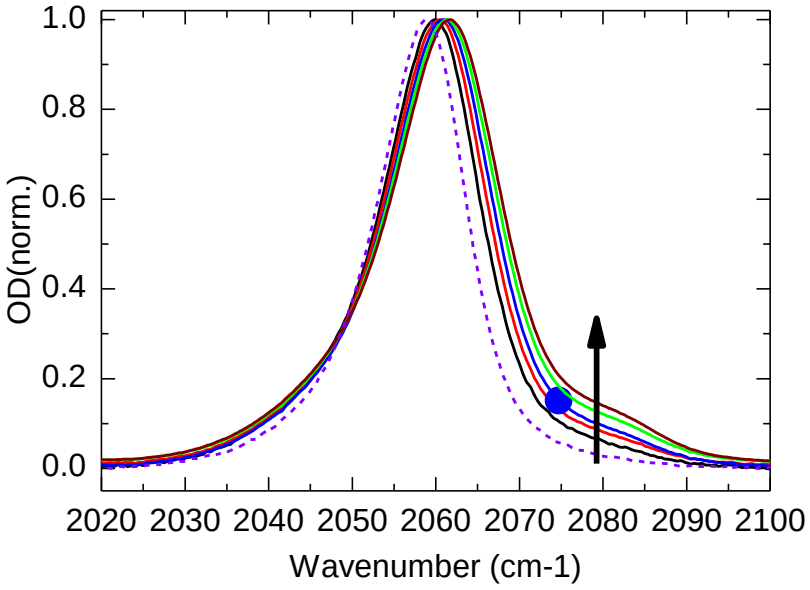

Figure 3.6. Concentration dependence FTIR spectra of NaSCN on diglyme. Direction of the arrow shows the increase of concentration from 0.5M to 2.5M. Dashed purple line is the 50mM solution.

The anisotropy for a restricted diffusion model (the wobbling in a cone, see Ref. [187] assumes that the thiocyanate ion tumbles within a cone with a half angle of θ and that the whole complex have a much slower diffusive orientational randomization. The mathematical formulation of this model is given by:[187]

$$r(t) = y_0\left(Q^2 + (1-Q^2)e^{-\frac{t}{\tau_{wc}}}\right)e^{-\frac{t}{\tau_r}} \tag{3.4}$$

where the τ_{wc} is the characteristic time constant of the diffusion in the cone and τ_r is the time constant for the complete orientational randomization of the complex. The y_0 describes the amplitude at T_w=0, which should have a value of 0.4 in the absence of ultrafast inertial motions.[141] The half angle of the cone, θ, is related to a square of an order parameter, Q, by:[187]

$$Q^2 = \left(\frac{1}{2}cos\theta(1+cos\theta)\right)^2 \tag{3.5}$$

The order parameter (Q) and the characteristic times (τ_{wc} and τ_r) are obtained by comparing the corresponding terms in Equations (3.3) and (3.4). The calculated characteristic times, order

parameters, and the half cone angle are tabulated in Table 3.2. The calculated half cone angles for all the glymes do not show a large difference indicating that the cavity where the thiocyanate ion is located within the sodium-glyme complex is approximately the same for all the glymes. Moreover, it is apparent that the cone angle decreases with the glyme size. The result indicates that longer glymes, like G4, form smaller cavities than short ones, such as G2, probably due to the presence of uncoordinated ends in the glyme molecule which limit the overall mobility of the anion. In addition, the results suggest that the sodium ion is fully coordinated in all glymes (with probably two solvent molecules[63]) because it is expected that a lower coordination of a sodium ion would result in large voids. These large voids should be observed in the anisotropy as large half cone angles, due to the lower restriction in the motions of the thiocyanate ion.

The assignment of the long time constant in the wobbling-cone model to the overall rotation is supported by computing the rotational time using Debye-Stokes-Einstein (DSE) hydrodynamic theory. In DSE theory, the rotational reorientation time, τ_{rot}, of a spherical particle of hydrodynamic volume, *V*, rotating in a fluid medium of viscosity, η, is expressed as: $\tau_{rot} = \eta V / k_b T$,where k_b and T are the Boltzmann constant and the temperature, respectively.[188] The complete rotational reorientation time of the G2-NaSCN system is computed to be τ_{rot}~185 ps using the DFT molar volume of 301 cm^3/mol for the G2-NaSCN complex and the experimental viscosity of 1.52 cP for the 0.5M NaSCN-G2 solution. As observed, the computed time is in the same order of magnitude as the slower decay of the anisotropy (Table 3.2) indicating that the slower component of the anisotropy is very likely to arise from the complete rotational reorientation of the molecule.

The biexponential behavior of the anisotropy suggests that the restricted reorientation motion is responsible for the fast decay of anisotropy observed for the CN stretch of thiocyanate

ion in the different samples. Moreover, the characteristic times of the anisotropy decay are slower or equal to those seen in FFCF. Thus, it is likely that the calculated parameters of the FFCFs via the CLS contain both the structural as well as the reorientation induced spectral diffusion.[189] However, the anisotropy effect on the FFCF is likely to be small because the fast reorientational dynamics has a small contribution in the overall decay of the anisotropy. Interesting, the small difference in time scales of the first component of both the FFCF and the anisotropy suggests that those decays are likely to be caused by the same molecular motion; i.e., the restricted motion of the thiocyanate ion in a cone.

The dynamics of the thiocyanate ion motions in the ion pair and its effect on the FFCF and anisotropy are explored by numerically simulating the wobbling-in-cone motion of the thiocyanate ion. In this case, the simulations are only performed on the G2-NaSCN ion-pair complex, but it is expected that the model can be applied to the other NaSCN-glyme systems by including the corresponding the structural and dynamical characteristics, such as the derived cone angle and the rotational decorrelation time. In the numerical simulation, the thiocyanate is modeled as a restricted Brownian rotator evolving stochastically with a Langevin dynamics (see Theoretical section). Note that the simulation does not include the overall reorientation of the system and the dimensionless time of the simulation was "corrected" with the fast anisotropy decay of NaSCN-G2 for easier comparison.

The anisotropy computed from the numerical simulation using Equation (3.1) shows that for a large spring constant ($1/\delta$), the anisotropy (Figure 3.7(a)) exhibits the expected decay to the order parameter determined by the cone angle; i.e. Q^2. However, FFCF computed from the autocorrelation of the instantaneous frequencies shows two decorrelation times which are both faster than the rotational reorientation (Figure 3.7(b) and Table 3.3). These observed results do not

agree with the experimental observations of the system. In contrast, a different time evolution is observed when the spring constant (1/δ) is small; i.e., a loose oscillator. In this case, the decorrelation time of the rotational reorientation is not significantly affected (Figure 3.7(a)), but the dynamics of the FFCF is significantly slowed down (Figure 3.7(b) and Table 3.3).

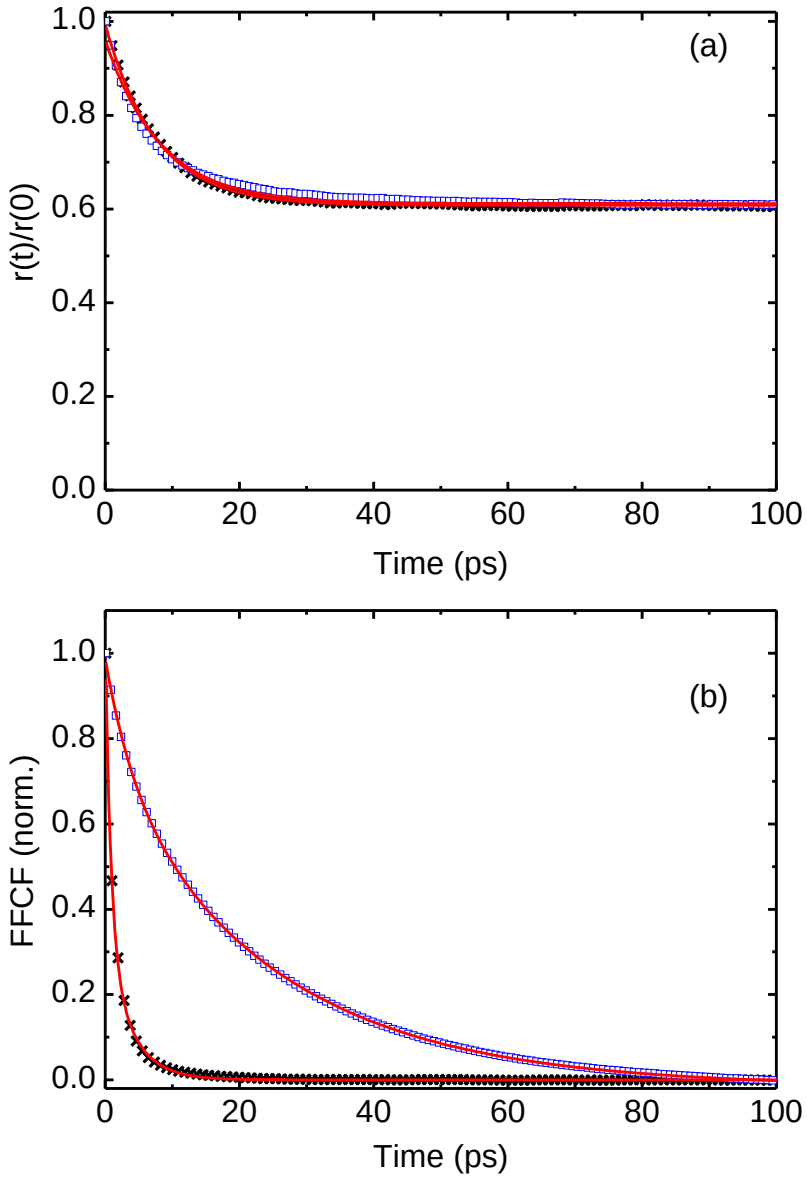

Figure 3.7. Simulated anisotropy, panel(a), and FFCF, panel(b), for larger spring constant (δ=0.05), (black crosses) and for smaller spring constant (δ=0.7), (blue squares). Red solid lines are the exponential fittings. Note that the time axes are normalized with respect to the fast decay of individual anisotropy decay.

In addition, a decrease in the value of the spring constant (1/δ) always results in slower dynamics and amplitude of frequency fluctuations for both FFCF decays (Figure 3.8). The dynamics observed for the anisotropy for the loose oscillator (i.e., small 1/δ) is expected since a lower value of the spring constant directly translates to larger fluctuations of the center of mass of the tethered rotor which do not change significantly its angular distribution along the tether. In contrast, large fluctuations in the position of the thiocyanate ion should directly translate to large fluctuations of the frequency and changes in the FFCF dynamics as shown by the simulations. Thus, for a loose oscillator the FFCF shows two decay times: one faster and one slower than the decorrelation time of the rotational diffusion.

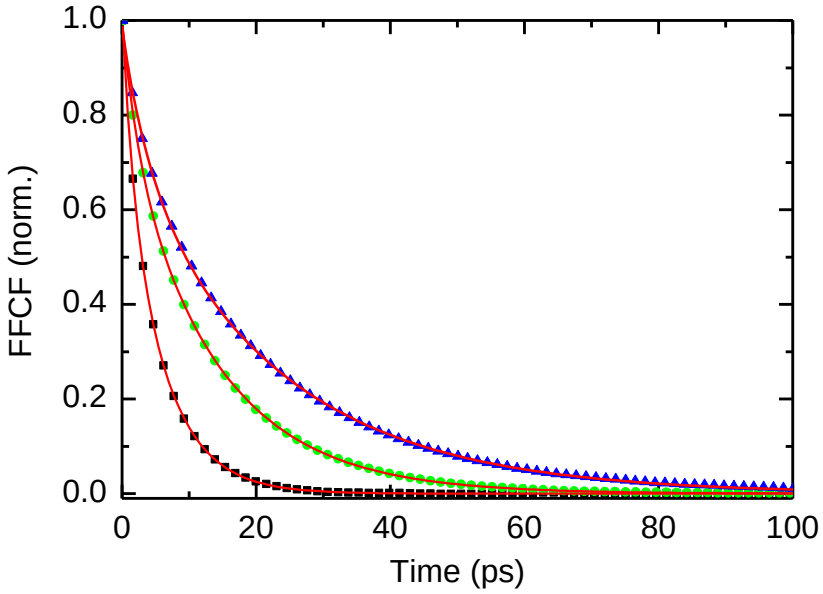

Figure 3.8. FFCF computed for different spring constants δ=0.3 (black squares), δ=0.5 (green circles) and δ=0.7 (blue triangles). Red line shows the fitting with two exponential decays.

Overall, the loose wobbling-in-a-cone model correctly reproduces the experimental observations. Interestingly, this model also shows that the second decay of the FFCF is caused by motions in the direction of the tether. Therefore, the second decay of the FFCF is indicative of the extent of the thiocyanate cavity along the direction of the S-N atoms of the anion, since lower

values of spring constant give slower second decay of the FFCF indicating that the thiocyanate ion can make larger displacements along this direction. Experimentally, the second decay of the FFCF increases its characteristic time when the glyme length is increased which demonstrates that larger glymes allow greater displacements of the thiocyanate ion in the cavity. This observation is also supported by the amplitude of the frequency fluctuations computed from the FTIR lineshape, where the fluctuation amplitude is larger for larger glymes. The structure parameters derived from the modeling and the experiments are in agreement with a previous study which showed that the shorter glymes, like G2, have on average their chains associated to the sodium ion while in longer glymes parts of the molecule remains uncoordinated.[65] Thus, longer glymes should produce larger cavities where the thicyanate ion can reside. In addition, it is expected that glymes with shorter chains will have faster motions than glyme with longer chains because of their molecular size."

Table 3.3. The characteristic times calculated from the simulated anisotropy and FFCF.

Characteristic times for two spring constants	τ_1(ps) for δ=0.05	τ_2(ps) for δ=0.05	τ_1(ps) for δ=0.05	τ_2(ps) for δ=0.05
Anisotropy	7.5±0.1	-	7.5±0.1	-
FFCF	0.86±0.01	3.67±0.05	3.24±0.03	22.50±0.02

The results of the simulation confirm that the slow dynamics observed for the FFCF is due to the drifting of the thiocyanate cavity with respect to the sodium center. However, it is also possible that the thermal motions induced a stochastic change in the sodium-thiocyanate distance perpendicular to C-N direction. The stochastic motion along this molecular coordinate was also simulated. The results show that the anisotropy and FFCF have the same trend as in the stochastic changes along the direction of C-N direction. However, the drifting of the thiocyanate ion along

Na-C direction might be less favorable than along the C-N direction since the motion of the SCN ion along C-N direction will permit the formation of an octahedral geometry by simply displacing the uncoordinated end of the glyme molecule. To test this last hypothesis, the drifting of the thiocyanate ion within the cavity is evaluated in terms of energetics by using DFT calculations. The optimized geometries for two different sodium-thiocyanate distances show that the thiocyanate ion tends to move along the S-N direction (Figure 3.9). Moreover, the energy difference between the optimized geometries of ~2.6 kJ/mol is well within the thermal energy (~2.5 kJ/mol), indicating that motions proposed to describe the simulated anisotropy and FFCF are likely to occur at room temperature.

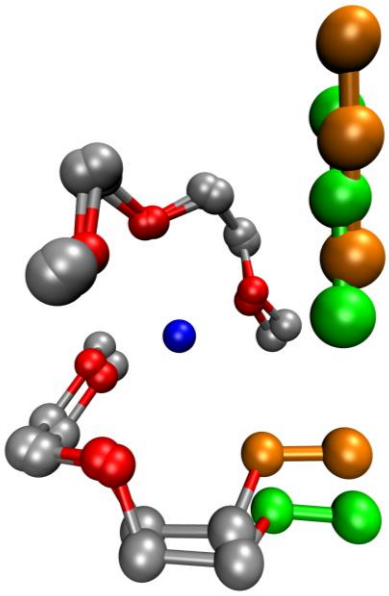

Figure 3.9. The drifting of the thiocyanate ion with respect to the sodium ion when sweeping the distance of Na-C.

3.5 Conclusions

This study shows that NaSCN forms free, contact ion pairs and aggregates when dissolved in glymes of different length, but predominantly exist as contact ion pairs irrespective of the glyme length. Moreover, the average distance between the cation and anion of ion pairs is found to be

similar despite the contrasting difference in chelating properties of the glyme when its length is increased. The vibrational dynamics of the ion pairs revealed from the 2DIR and anisotropy experiments provides evidence of a restricted rotational dynamics (i.e., wobbling-in-cone) in which the cone angle is similar in different glymes. A numerical simulation of the cone model, containing a drift along the C-N axis, correctly reproduces the experimental anisotropy and FFCF. The observed results indicate the cavity created by thiocyanate is approximately same for all Na-glyme complexes, but its extent and dynamics is defined by the length of the glyme molecule. DFT calculations support the motions and ion pair structure derived from the experimental data.

CHAPTER 4. MOLECULAR STRUCTURE, CHEMICAL EXCHANGE AND CONDUCTIVITY MECHANISM OF HIGH CONCENTRATION LITFSI ELECTROLYTES*

4.1 Introduction

The use of lithium-ion (Li-ion) batteries has gained widespread application in several fields including automobile and energy storage grids due to the high capacity and efficiency of this energy storage technology.[11, 190, 191] However, a battery having high energy density, high voltage, and fast charging rate has yet to be developed. New concepts and modifications to the chemistry of lithium-ion batteries have been introduced to enhance their performance.[20, 192-194] In particular, there has been a wave of new developments focused on the electrolyte.[96, 195-202] The electrolyte is one of the main components in a typical electrochemical cell because it is the medium where the charge transport between the electrodes occurs. Moreover, in Li-ion batteries, the electrolyte is responsible for forming the protective interface between the electrolyte and anode.[203-207] Thus, changes on the electrolyte can significantly affect the properties and performance of the overall battery. Recent studies have shown the feasibility of using high concentration electrolytes for the development of high voltage and high energy density Li-ion batteries.[98, 195-197, 208, 209]

The concentration of the lithium salt in a conventional Li-ion battery is typically ~1M and is primarily dictated by its conductivity.[119] While increasing the salt concentration decreases the overall conductivity of the electrolyte, a high concentration electrolyte has been shown to possess a better thermal stability than its low concentration counterpart, which is an advantage from a safety perspective.[195, 210] Currently, in commercial Li-ion batteries, a solid electrolyte interphase (SEI) is formed by the decomposition of solvent molecules during the first few cycles to prevent

* This chapter was previously published as Molecular Structure, Chemical Exchange, and Conductivity Mechanism of High Concentration LiTFSI Electrolytes. Susith R. Galle Kankanamge and Daniel G. Kuroda., *The Journal of Physical Chemistry B 2020 124* (10), 1965-1977 and reprinted by the permission of ACS publications

the degradation of the electrodes.[21, 203-206] In particular, it was found that the formation of a stable SEI on the cathode prevents the degradation of the electrodes at high voltage, which occurs due to the presence of excess free solvent molecules in the ~1M electrolyte.[210-213] This particular problem is avoided in high concentration electrolyte because of its limited amount of free solvent molecules prevents the deterioration of the electrodes.[96, 195, 196, 210] In addition, the large concentration of anions in the high concentration electrolytes contributes to the formation of a stable SEI.[197, 210]

High concentration electrolytes are simply made by dissolving lithium salts in a high dielectric solvents.[195, 196] Using this recipe, many studies have demonstrated that the molecular characteristics of the anion and solvent are critical for making the electrolytes because they significantly affect the electrolyte properties such as conductivity and electrochemical stability.[195, 197] On the anion side, it is now known that multi-dentate anions with large charge delocalization are needed.[119] Two anions that possess all the aforementioned properties are: bis(trifluoromethanesulfonyl)imide (TFSI-) and bis(fluorosulfonyl)imide (FSI-). On the solvent side, different solvents have been used for this purpose and some examples are water,[97] acetonitrile,[98] dimethylcarbonate,[195] and dimethoxyethane.[196] So far, it has been difficult to predict the macroscopic properties of the electrolyte in terms of its constituents largely because of the lack of a microscopic map detailing the arrangements and interactions occurring in these systems.

The structure and interactions of the molecular components (i.e., solvent, lithium salt ions) in high concentration electrolytes composed of organic solvents have not been extensively investigated experimentally[214-216] and computationally.[217] Henderson and co-workers derived the structure and interaction of TFSI- and Li^+ in concentrated electrolytes by analyzing the crystal structure of solvates as function of the solvent molecular structure.[105, 106, 108-110, 218] These studies revealed the existence of two TFSI- conformations (cisoid [C_1] and transoid [C_2]), which only

differ by the relative positions of the -CF_3 groups.[107] Moreover, it was found out that the type of the anion conformation governs the coordination with the lithium center.[107] For example, the transoid conformation is observed for solvent separated ion pairs, while cisoid conformation is found when TFSI- is directly coordinated to Li^+.[107] While $TFSI^-$ coordinates to Li^+ in different ways depending on the structure formed (i.e., solvent separated ion pairs [SSIP], contact ion pairs [CIP] and aggregates [AGG]), the solvent coordination to the cation always occurs via the carbonyl oxygen for carbonyl containing solvents.[105] Therefore, it has been deduced that the interactions observed in solvates should be maintained in high concentration electrolytes.[110, 112, 216] However, the chemical structure of the liquid electrolytes might be significantly different from that of the solid solvate due to the higher number of degrees of freedom in the liquid. Moreover, Watanabe and co-workers previously demonstrated that the structure of the high concentration electrolyte resembles more that of an ionic liquid than a traditional high concentration solution.[111, 112] Interestingly, while a few studies have been conducted to explore experimentally the structure parameters in high concentration electrolytes, none of them provided direct insights into the structure and dynamics of high concentration electrolytes.

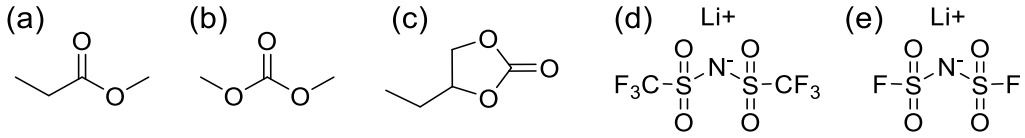

Scheme 4.1. Chemical structure of (a) methyl propionate (MP), (b) dimethylcarbonate (DMC), (c) butylenecarbonate (BC), (d) lithium bis(trifluoromethanesulfonyl)imide (LiTFSI) and (e) lithium bis(fluorosulfonyl)imide (LiFSI).

In this work, we investigated the structure and dynamics of high concentration electrolytes composed of LiTFSI salt and three carbonyl containing solvents (MP, DMC or BC) using IR spectroscopic and theoretical methods. Our experimental efforts focused on the carbonyl stretch of the solvents because it has been shown to be a good reporter of both the structure and dynamics

of the system.[108, 115-117, 122, 126, 219, 220] Moreover, the use of time-resolved 2DIR spectroscopy allowed us to obtain direct information about the different molecular processes in picosecond time scale occurring in the different solutions.[145] In addition, the experimental observations were complemented with DFT calculations and classical molecular dynamics simulations to interpret and corroborate our experimental findings.

4.2 Methodology

4.2.1 Sample preparation

Lithium bis(trifluoromethylsulfonyl)imide (LiTFSI, $LiN(SO_2)_2(CF_3)_2$, > 98%) was obtained from Alfa Aesar and dried at 130°C for 24 hours before use. Methyl propionate (MP, $C_4H_8O_2$, >99%) and dimethyl carbonate (DMC, $C_3H_6O_3$, 99%) were obtained from Acros Organics and 1,2-butylene carbonate (BC, $C_5H_8O_3$, 98%) was obtained from TCI Chemicals. All solvents were dried with 1-2mm molecular sieves for 24 hours prior to use. Solutions of LiTFSI in each solvent at 1:1.5, 1:2, and 1:3 Li^+:solvent molar ratios were prepared by simply mixing the components inside a N_2-filled glovebox at room temperature. After preparation, all the samples contained less than 150 ppm of water.

The cell (Harrick Scientific) for the FTIR experiments consisted of the sample sandwich between a pair of 2 mm calcium fluoride windows without a spacer. For the 2DIR experiments, the sample cell consisted of the sample between a CaF2 convex lens (focal length 1 m and path length >500 nm) and a 2 mm regular window. Detailed information of the lens sample cell can be found in Ref. [116].

4.2.2 Linear IR Spectroscopy

Fourier transform infrared (FTIR) experiments were performed using a Bruker Tensor 27 spectrometer with 0.5 cm^{-1} resolution and liquid nitrogen cooled narrow band MCT detector. All

samples were measured in transmission mode. Each FTIR spectrum was recorded as an average of 40 individual scans at 25 °C.

4.2.3 Two dimensional IR spectroscopy

Two dimensional infrared experiments were performed using a similar setup that is previously described in the literature.[221] Briefly, Ti:Sapphire amplifier (Spectra Physics Mai Tai and Spitfire) with a 5 kHz repletion rate was coupled to an optical parametric amplifier (Spectra Physics, 800C) and a difference frequency generation crystal ($AgGaS_2$) to produce ~60 fs broadband infrared pulses. The generated pulses were split into three identical pulses (k_1, k_2 and k_3) and later focused on the sample with a boxcar configuration.[145] The time intervals: τ (time between the first pulse and the second pulse), T_w (time between the second and the third pulse) and t (time between the third pulse and the photon echo) were controlled with four computer controlled translational stages (PI Micos). The generated photo echo with pulses with parallel polarization (<XXXX>) in the phase matching direction ($-k_1+k_2+k_3$) was heterodyned with a fourth pulse (local oscillator) and later dispersed by a Triax monochromator. Finally, the non-linear signal and local oscillator were detected with a liquid nitrogen cooled 64 element MCT array detector (Infrared Systems Developments). Here, 2D IR data were collected by scanning τ time from -3 ps to +3 ps in increments of 5 fs for each waiting time in order to collect both the rephasing and non-rephasing data by switching the time ordering.[145] Signals were collected for waiting times from 0 to 6 ps in steps of 0.5 ps with an additional measurement at 250 fs. In all the measurements, the local oscillator always preceded the photon echo signal by ~0.5 ps. The time domain signal, collected as a function of (τ, T, λ_t) via a monochromator-array detection, is transformed into the 2DIR spectra (ω_τ, T, ω_t) by means of Fourier transforms. A detailed explanation of the Fourier analysis has been described elsewhere.[175]

4.2.4 Ionic Conductivity and Viscosity Measurements

The ionic conductivity of the electrolytes was measured using a YSI 3200 conductivity meter combined with YSI 3250 cell probe. The temperature of the solutions was recorded with the integrated temperature probe of the cell probe. The viscosity of the solutions was measured using Brookfield DV-II+pro viscometer.

4.2.5 Density Functional Theory Calculations

Density functional theory (DFT) calculations were performed using the Gaussian 09 software and the 6-311++G** basis set was used at B3LYP level of theory.[222] One lithium ion with one TFSI ion and one lithium ion with two TFSI ions were geometrically optimized separately for three different solvents, DMC, MP and BC, where the number of solvent molecules interacts with the lithium center was selected from one to two. All DFT computations present in the main text were performed in the gas phase. The vibrational frequencies of each system were calculated and no imaginary frequencies were observed indicating that the system was in a minimum of energy.

4.2.6 Molecular Dynamics Simulations

Classical molecular dynamics (MD) simulations were performed using SANDER module of the AMBER 16 program package.[223] Simulations were only performed on the cyclic carbonate based electrolyte since the other two molecules have conformational isomers which required a more precise description of the system. The BC and LiTFSI were modeled using the general AMBER force field (GAFF) and a charge scaling factor of 0.8 was used to correct the overestimate of electrostatic point charge.[224] Moreover, the non-bonding parameters of the lithium ion were modified according to the values presented in Ref. [225] The Packmol software package was used to build the electrolyte system in a cubic box of 30x30x30 Å with the LiTFSI to BC ratio of 1:2.

Periodic boundary conditions were imposed in the simulation. Particle mesh Ewald methodology was used to describe the long-range electrostatic interaction with the cutoff of 12 Å. The SHAKE algorithm was used to constrain the bonds involving hydrogen. In the simulation, the system was initially energy-minimized for 200 steps using the steepest descent method followed by 300 steps of conjugated gradient method. After the minimization, the system was equilibrated at 500 K in an isothermal-isobaric ensemble (NPT) for 5 ns with a time step of 2 fs. The system was cooled down with another NPT run at 300 K for 3 ns. The Langevin thermostat was used in both NPT runs. The density of the system was used to check that the system has reached equilibrium. Finally, the system was equilibrated in canonical ensemble (NVT) for 1 ns with a time step of 2 fs before performing the production run at the microcanonical ensemble (NVE). The production run was recorded for 10 ns in 100 fs steps.

4.3 Results

The characterization of the solvation of LiTFSI at high concentrations in different solvents (i.e., MP, DMC and BC) was first performed using linear IR spectroscopy. These experiments focused on the carbonyl stretch of the solvent molecules located in the 1700-1820 cm^{-1} region of the IR spectrum. The IR spectra of LiTFSI in MP (Figure 4.1) as a function of the Li^+:solvent ratio show two main bands centered at ~1714 cm^{-1} and ~1741 cm^{-1}, where the band located at higher frequency decreases as the salt concentration increases. The higher frequency band is assigned to the free carbonyl stretch mode while the lower frequency band is assigned to the coordinated carbonyl stretch mode, which is in agreement with previous assignments.[116, 117, 120, 219, 226] The difference spectra, using the 1:3 ratio spectrum as a reference, shows a third band growing between the two main bands as the Li^+ concentration increases. Simultaneously, two negative peaks appear on either side of the positive peak. While the negative peak at high frequency is caused by a

decrease of free carbonyl band, the negative peak at low frequency is likely the product of a frequency shift and bandwidth change in the coordinated peak possibly due to a change in the dielectric constant of the solution[227] and changes in the dynamics of the solution with concentration.[116].

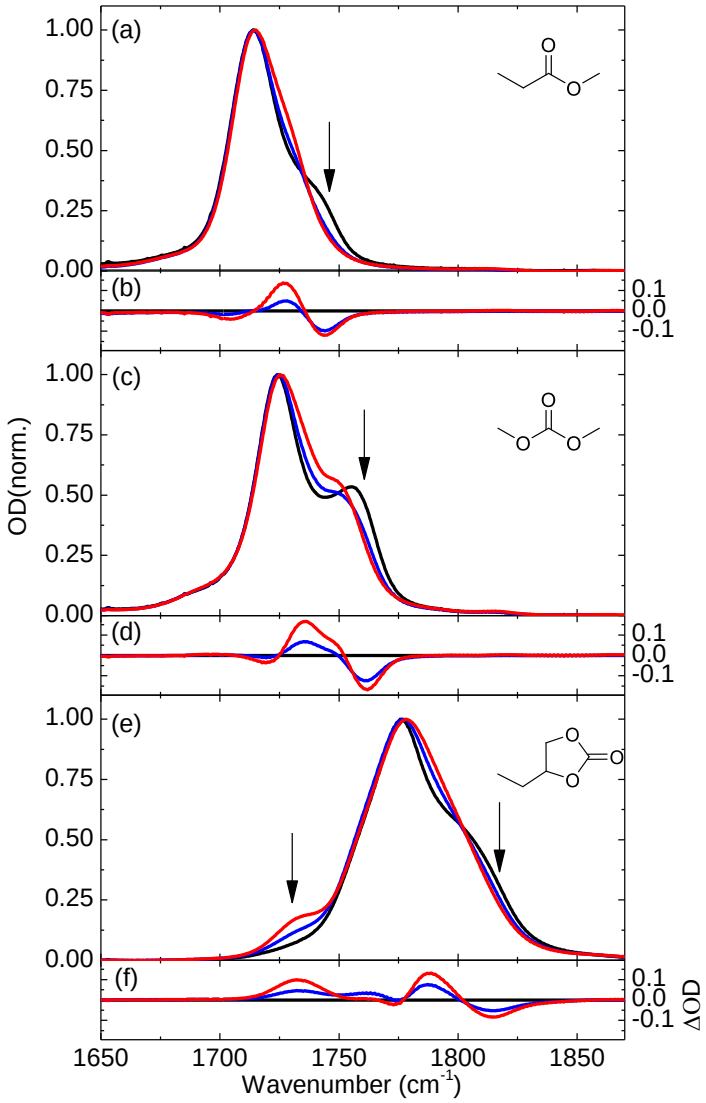

Figure 4.1. The FTIR spectra of LiTFSI in (a) MP, (c) DMC and (e) BC at Li^+:solvent ratio of 1:3 (black), 1:2 (blue) and 1:1.5 (red). The (b), (d) and (f) panels represent the difference spectra with respect to the 1:3 ratio mixture for MP, DMC and BC solvent, respectively. Arrows mark the positions of the less visible peaks as discussed in the text.

A similar pattern is observed for LiTFSI in the other two solvents (Figure 4.1) where the coordinated and free bands are located at ~1724 cm^{-1} and ~1756 cm^{-1} in DMC and at ~1777 cm^{-1}

and ~1814 cm^{-1} in BC. These observed changes in the FTIR spectra with salt concentration follow the trends previously seen for the carbonyl stretch of BC and DMC.[116] However, the intensity of the higher frequency peak and the separation between two observed peaks differ for DMC and BC when compared to MP. Overall, the frequency separation between the peaks follows the trend: $\Delta\nu(BC) > \Delta\nu(DMC) > \Delta\nu(MP)$. In addition, the difference spectra of both DMC and BC solutions show the growth of a band in between the low and high frequency bands in close similarity to that of the MP electrolytes. However, the spectra differ significantly in the width of the carbonyl stretch, which is clearly broader for BC than for the other two solvents. Finally, the spectra of the BC electrolyte show an extra peak, which rises with increasing salt concentration and appears on the lower frequency side of the main band (~1731 cm^{-1}).

The molecular structure and dynamics of the high concentration electrolytes were also investigated by means of 2DIR spectroscopy. Figure 4.2 shows the 2DIR spectra collected at different waiting times (T_w) for the 1:2 molar ratio solutions. The 2DIR spectrum for the MP electrolyte at T_w=0 ps shows a pair of peaks along the diagonal line where the red contoured peak (positive) [at $\omega\tau$, ωt = ~1713, ~1710] arises from the transitions between the ground and first excited vibrational states (v=0↔1) while the blue contoured peak (negative) [at $\omega\tau$, ωt = ~1713, ~1693] appears due to the transition between first and second excited vibrational states (v=1→2). The blue peak is downshifted by ~17 cm^{-1} with respect to the red peak due to the anharmonicity of the carbonyl stretch potential and is in agreement with previous studies.[116] As in the IR spectra (Figure 4.1), the coordinated and free carbonyl bands for MP and BC are not resolved in the 2DIR spectra for any of the studied waiting times. In contrast, the DMC spectrum at T_w=0 ps shows the same two peaks observed in the FTIR spectra (Figure 4.1).

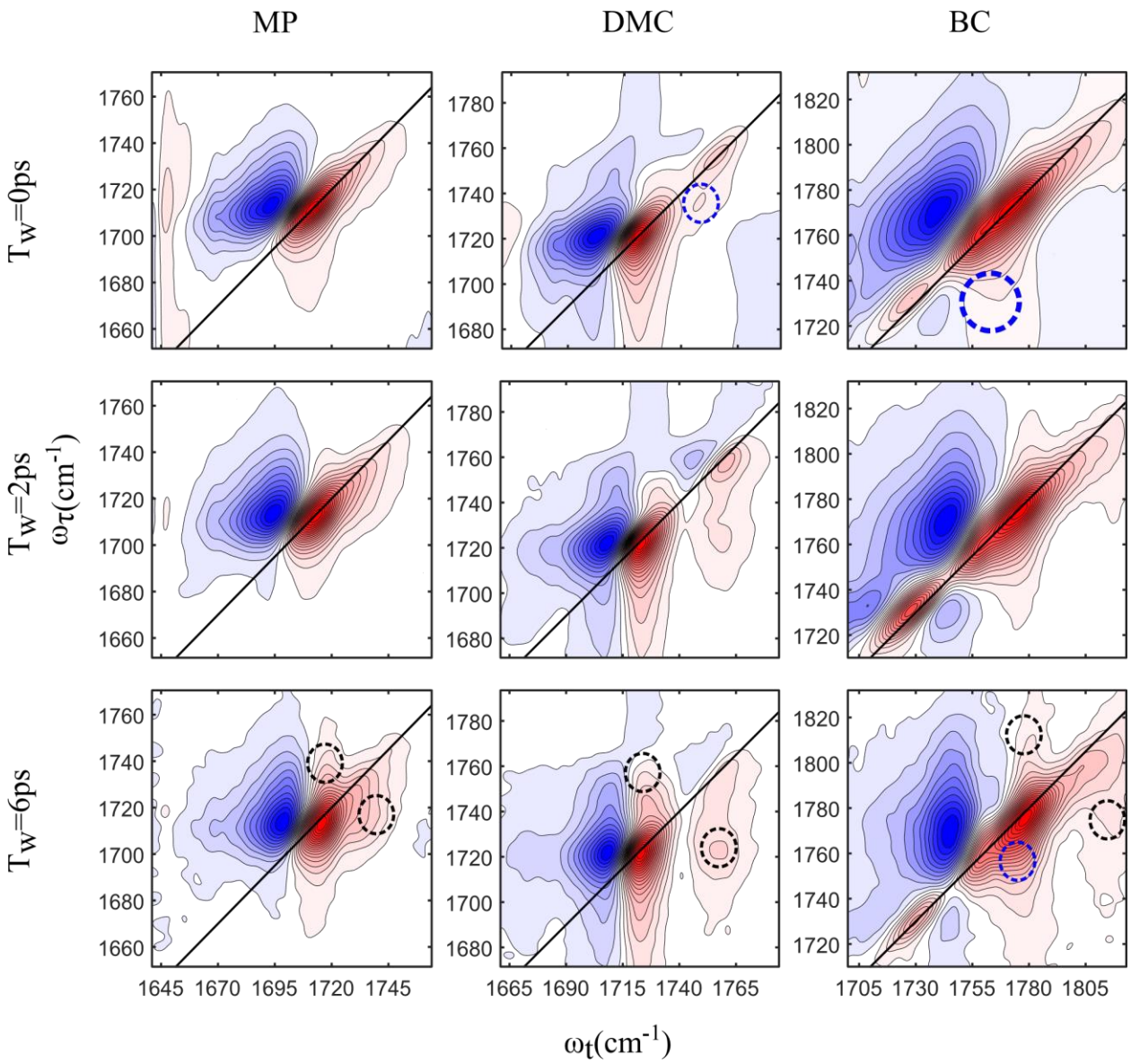

Figure 4.2. The 2DIR spectra of LiTFSI in MP, DMC and BC of 1:2 Li^+:solvent ratio at different waiting times. The positions of the cross peaks are marked in black circles (chemical exchange) and blue circles (vibrational coupling).

The T_w evolution of the 2DIR spectra (Figure 4.2) suggests that the carbonyl stretch modes experience significant changes with time in all samples. Initially, at T_w = 0 ps, all samples have peaks elongated along the diagonal line, but as T_w progresses the shape of the peaks becomes more upright manifesting the spectral diffusion process.[145] However, not all the electrolytes show the same time evolution. For example, the peaks at T_w = 6 ps remain fairly elongated for the BC

electrolyte compared to MP and DMC electrolytes. Furthermore, a substantial difference is observed in T_w dependence of 2DIR spectra due to the growth of off-diagonal features (i.e., cross peaks). In the MP electrolyte, the presence and growth of cross peaks at [ω_τ, ω_t = ~1713, ~1741] and [ω_τ, ω_t = ~1741, ~1713] is only evident at longer waiting times, while for the DMC electrolyte, a cross peak appears at T_w = 0 ps at [ω_τ, ω_t = ~1736, ~1748] indicating the presence of vibrationally coupled transitions between the symmetric and asymmetric modes of $Li(TFSI)_2(DMC)_2$.[115-117, 132] In addition, the 2DIR spectra of the DMC electrolyte show the appearance and growth of additional cross peaks at [ω_τ, ω_t = ~1724, ~1756] and [ω_τ, ω_t= ~1756, ~1724] with waiting time, which is similar to the 2DIR spectral evolution observed for the MP electrolyte. In the case of the BC electrolytes, the 2DIR spectrum at T_w = 0 ps shows a cross peak between the lower part of the main band and the isolated lower frequency band, but it does not appear to show changes in intensity with T_w. Additionally, the 2DIR spectra of the BC solution presents three other cross peaks at [ω_τ, ω_t = ~1777, ~1814], [ω_τ, ω_t = ~1814, ~1777] and [ω_τ, ω_t = ~1757, ~1777], which grow with the waiting time.

4.4 Discussion

It has been previously shown that the preferred coordination number for Li^+ is four.[116, 126, 203, 228-240] It is also known that in dilute organic-based electrolytes, Li^+ exists as free ions, solvent separated ion pairs, contact ion pairs and aggregates,[115, 241, 242] but the number of solvent molecules and Li^+ ionic speciation directly depends on the availability of solvents in the electrolyte system. In the case of high concentration electrolytes, the ratio of solvent molecules to Li^+ is lower than four; hence, it is expected that Li^+ will not be fully solvated by four solvent molecules. However, it has been previously demonstrated that high concentration lithium salt solutions in organic solvents do not tend to form nanoheterogeneous structures.[243] Therefore, it is expected that this

solution will be more homogeneous at the microscopic level, where Li^+ forms extended aggregates with the anion and the solvent molecules will interact with Li^+ to fulfil its coordination number of four.[63, 101, 210] This structure is reminiscent to that previously seen in lithium solvates.[107-109, 218] Thus, the formation of lithium centers with one or two solvent molecules in its solvation shell is likely to occur in large proportion in solutions with 1:2 molar ratio, while lithium centers containing more than two solvent molecules should have low occurrences. On the anion, the limited availability of solvent molecules at 1:2 molar ratio forces TFSI- to adopt both bidentate and monodentate coordinations with Li^+ and to coordinate of more than lithium center to fulfill the Li^+ coordination number of four, as previously seen in the crystal structure of LiTFSI and ethylene carbonate solvates.[210] Thus, it is reasonable to assume that the FTIR spectra should have the spectral signature corresponding to the different coordinating species (Scheme 4.2): $Li(TFSI)_1(Solvent)_2$, $Li(TFSI)_2(Solvent)$ and $Li(TFSI)_2(Solvent)_2$.

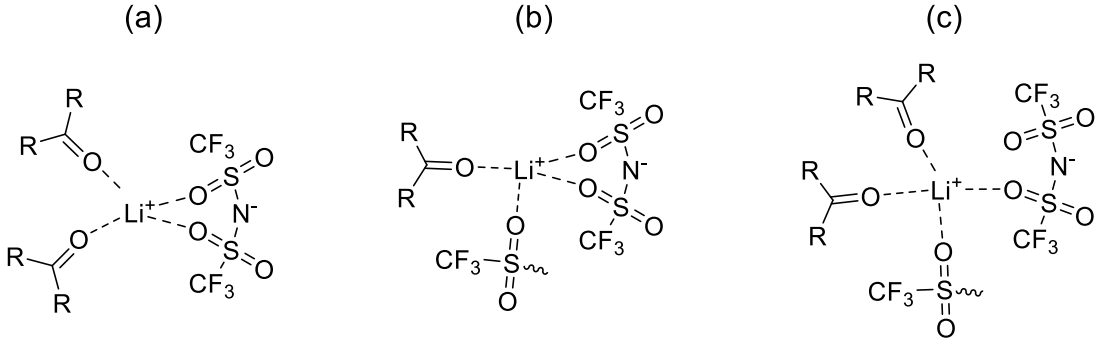

Scheme 4.2. (a) $Li(TFSI)_1(Solvent)_2$, (b) $Li(TFSI)_2(Solvent)$ and (c) $Li(TFSI)_2(Solvent)_2$

The FTIR spectra as a function of concentration (Figure 4.1) show the rise and disappearance of different bands. In particular, all the solvents show more than one band at the ratio of [Li^+:solvent]=1:1.5. However, the presence of multiple bands could arise from the strong vibrational coupling between carbonyl stretches of two solvent molecules coordinating the same lithium center, such as in the case of $Li(TFSI)_1(Solvent)_2$, and $Li(TFSI)_2(Solvent)_2$, which split the

transition in two.[226] This splitting is a consequence of having two strongly coupled and degenerated transitions. The vibrational Hamiltonian of carbonyl stretches is represented by:

$$\widehat{H} = \begin{bmatrix} \omega_{10} + \delta\omega^{a}(t) & \beta(t) \\ \beta(t) & \omega_{10} + \delta\omega^{b}(t) \end{bmatrix} \tag{4.1}$$

where ω_{10} is the frequency of the two carbonyl stretches coordinating Li^{+} in the site representation, and $\beta(t)$ and $\delta\omega^{j}(t)$ are the coupling constant and the frequency fluctuation of the j^{th} site, respectively. For this vibrational Hamiltonian, the frequencies of the mixed states are given by:

$$\omega_{\pm} = \frac{2\omega_{10} + \delta\omega^{a}(t) + \delta\omega^{b}(t) \pm \sqrt{\left(\delta\omega^{a}(t) - \delta\omega^{b}(t)\right)^{2} + 4\beta(t)^{2}}}{2} \tag{4.2}$$

where $\omega_{\pm}$ represent the frequencies of the symmetric (+) and asymmetric (-) stretches. In the case of small frequency fluctuations, the solution reduces to

$$\omega_{\pm} = \omega_{10} \pm |\beta(t)|, \tag{4.3}$$

which demonstrates the splitting of the two degenerate transitions.

The presence of more than one peak in the FTIR band cannot be simply assigned to different species. To disentangle the IR carbonyl signatures, the stretching frequencies for the possible solvation shells of Li^{+} were computed using DFT. As predicted, the calculated vibrational transitions (Figure 4.3) show that the solvation shells containing two solvent molecules (i.e., $Li(TFSI)_1(Solvent)_2$ and $Li(TFSI)_2(Solvent)_2$) have two well separated transitions in the carbonyl stretch region, in which the frequency separation denotes the vibrational coupling between transitions. Interestingly, the transition dipole magnitudes of carbonyl stretches are not equal for $Li(TFSI)_2(Solvent)_2$ in the different solvents. For example, the DMC and MP structures show a difference in the transition dipole magnitude for the two carbonyl vibrational modes, while in the BC species, dipoles are almost equal. Moreover, the computations demonstrate that the number

and coordination of TFSI- in the Li^+ solvation shell defines the overall central frequency of the carbonyl stretch transitions (Figure 4.3). This last result is expected since the additional TFSI- lowers the overall charge density of the lithium ion and diminishes its influence over the carbonyl group. Finally, the separation between the transitions corresponding to the solvation shell containing two solvent molecules (i.e., structures of the form $Li(TFSI)_x(Solvent)_2$) appears to be governed by the chemical structure of the solvent. Note that similar trends in vibrational frequency positions and intensities are observed when a polarizable dielectric medium is used.

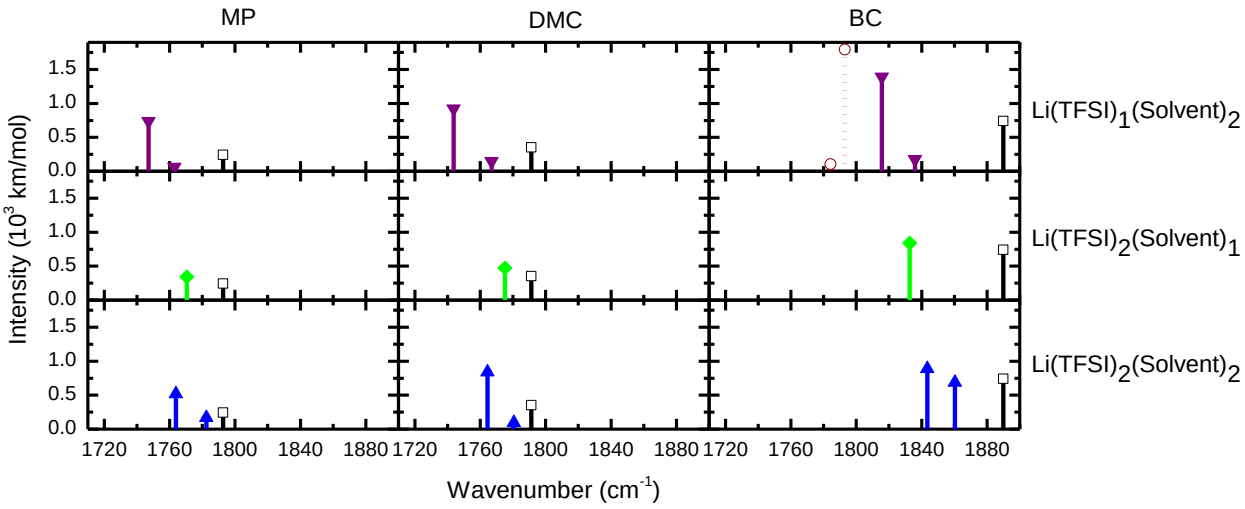

Figure 4.3. DFT frequency calculations of MP (left), DMC (middle) and BC (right), with different geometries. The top panels represent the frequencies of the coupled transitions of two carbonates which are coordinated to LiTFSI complex. The middle plots correspond to the geometry of a single carbonate coordinated to $Li(TFSI)_2$ complex. The bottom panels show the coupling of two carbonates which are coordinated to $Li(TFSI)_2$ complex. For BC, coupled frequencies of the two carbonates with opposing dipole direction are calculated (brown dashed lines). The frequency of the free solvent molecule is denoted with black open-square in each plot.

The computed DFT frequency separations and transition dipole magnitudes for the carbonyl stretch transitions in the different Li^+-solvent complexes appear to explain the overall carbonyl stretch lineshape and its concentration dependence. First, the frequency separations between $Li(TFSI)_2(Solvent)_2$ and $Li(TFSI)_1(Solvent)_2$ justify the bandwidth of the carbonyl stretch bands because of the similarity between the frequency separation and the experimental linewidth

trends (i.e., $\Delta\nu(BC) > \Delta\nu(DMC) \approx \Delta\nu(MP)$). Second, the computations predict that the carbonyl band of $Li(TFSI)_2(Solvent)_1$ should be located in between the free and the $Li(TFSI)_1(Solvent)_2$ species. The peak corresponds to the $Li(TFSI)_2(Solvent)_1$ is definitely seen in all samples as a growing peak when the Li^+:solvent ratio is increased from 1:3 to 1:1.5. Third, the position of the $Li(TFSI)_1(Solvent)_2$ carbonyl band is predicted to have the lowest frequency position of the three species. The position of this species explains why the maxima location of the carbonyl band remains unaltered for the investigated Li^+:solvent ratio since $Li(TFSI)_1(Solvent)_2$ is the most likely species to be formed at 1:3 to 1:1.5 ratios. Finally, the peak at the highest frequency, which decreases when the Li^+ concentration is increased, corresponds to "free" solvent molecules. While it sounds counter intuitive to propose the presence of free solvent molecules in such high concentrated solution, the molecular interactions in these solutions are strongly dictated by the ion-ion forces,[111] and weakly constrained by ion-solvent interactions. In this particular case, the existence of "free" solvent molecules evidences the presence of intermediate states in which a solvent molecule diffuses in and out from a lithium center, as it hops between different centers. This band assignment is in agreement with the observation of a fast coordination/de-coordination of solvent molecules in these high concentration electrolytes (see below).

The Li^+ solvation shell deduced from the FTIR and DFT computations is also in agreement with the MD simulation. The integrated g(r) for the Li^+-O(TFSI) is ~3.4 at 3.55Å (Figure 4.4), indicating that on average more than one TFSI- coordinates with a lithium center. In other words, TFSI- has both bidentate and monodentate coordination with Li^+. The bidentate coordination of $TFSI^-$ to Li^+ results in a TFSI- conformation where its nitrogen atom points away from the lithium center. As a result, the nitrogen atom is positioned closer to a different lithium center (Figure 4.4). The g(r) of Li-N(TFSI) confirms the bidentate arrangement through the presence of two peaks at

4.45Å and 2.85Å, where the latter accounts for the low probability of finding the nitrogen atom pointing away from one lithium center (Figure 4.4). The complete coordination structure of Li^+ is derived from the g(r) of Li-O(carbonyl) (Figure 4.4). The integrated g(r) shows that on average 2.5 of BC molecules coordinate each Li^+. Note that the coordination number of BC exceeds the Li^+:solvent molar ratio of the system due to the sharing of BC molecules between different lithium centers (Figure 4.4). Thus, the Li^+ solvation shell arrangement derived from the MD simulations agrees with the presence of the previously proposed species; i.e., $Li(TFSI)_1(Solvent)_2$, $Li(TFSI)_2(Solvent)$ and $Li(TFSI)_2(Solvent)_2$.

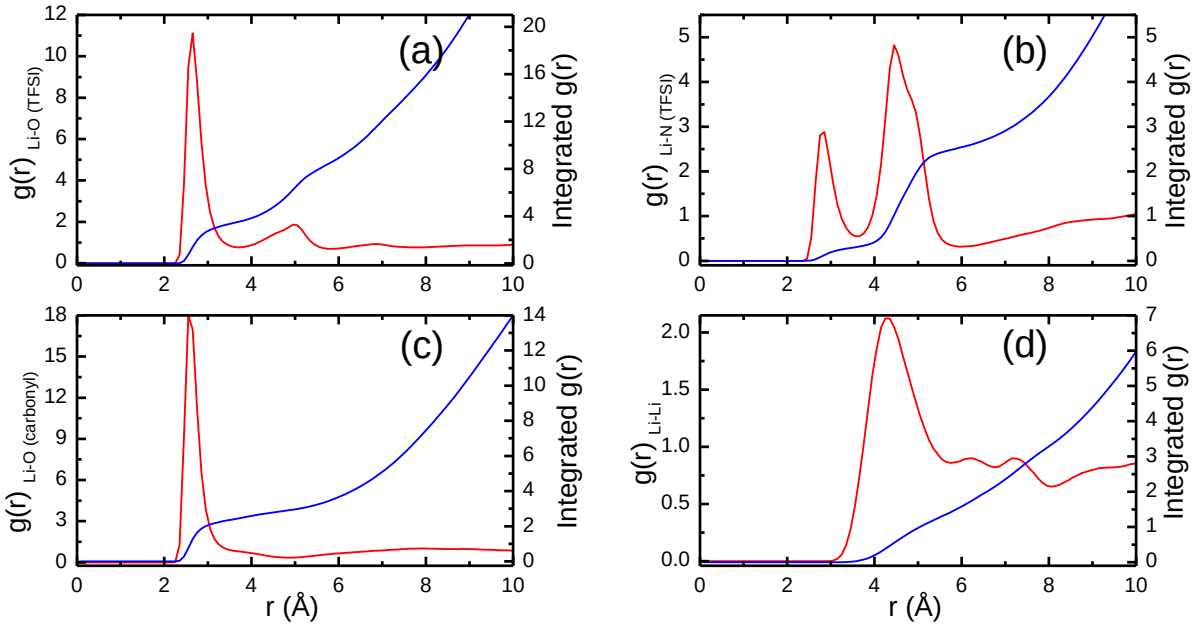

Figure 4.4. The radial distribution function, g(r), and the integrated g(r) obtained from MD simulations for (a) Li-O_{TFSI}, (b) Li-N_{TFSI}, and (c) Li-$O_{carbonyl}$ and (d) Li-Li

Another important feature observed in the FTIR spectra (Figure 4.1) as well as 2DIR spectra (Figure 4.2) is the low frequency band in the BC sample. This band rises when the Li^+ concentration is increased. This lowest frequency band in the BC carbonyl spectrum was previously observed in Li^+ solutions of BC and was attributed to the formation of ion pairs and aggregates.[116] However, the solution of Li^+ with TFSI- as the counter ion at 1:2 molar ratio of

Li^+:solvent also shows this band (Figure 4.1). Therefore, the peak appearing at the lower frequency side of the carbonyl band is not likely to arise from the carbonyl groups interacting with a single Li^+, but from carbonyl groups of two different and adjacent Li^+ centers forming a dimer (Scheme 4.3).

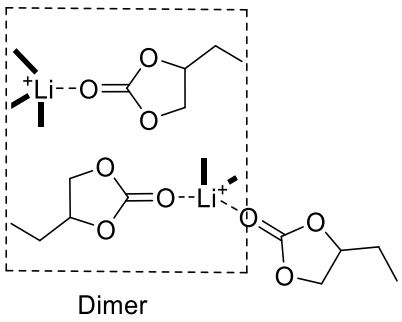

Scheme 4.3. The proposed structure of the BC dimer. Broad black lines represent the coordination of Li^+ with either solvent molecules or anions.

The dimer formation by BC carbonate molecules in the solvation shell of Li^+ is not new since it has been previously observed in a LiTFSI:EC solvate[210] and predicted theoretically in another cyclic carbonate, propylene carbonate.[244] In the solvate structure, two EC molecules coordinating two different lithium centers are observed to be an arrangement where both EC molecules are almost parallel to each other, but with their dipoles are pointing in opposite directions.[210] This type of structure was predicted to have a stabilization energy of ~20 kJ/mol.[244] The DFT calculated frequencies of the dimeric BC structure (dashed lines Figure 4.3) are in agreement with the assignment of the low frequency band in the FTIR spectra. Therefore, it is proposed that the dimeric BC structures between two different Li^+ are the cause of the low frequency band in high concentration BC electrolytes. In addition, the high transition dipole predicted for the dimer transition and the small area of the dimmer band observed experimentally demonstrate the small occurrence of such a structure in the BC electrolyte. The assignment of this low frequency band to a dimer is also consistent with the 2DIR spectra where a cross peak between

this band and the main carbonyl band of BC at T_w = 0 ps (Figure 4.2 at [ω_τ, ω_t = ~1732, ~1767]) is observed. This cross peak arises from the vibrational coupling between the high intensity dimer transition and the other two carbonyl groups solvating Li^+ which do not form the dimer (Scheme 4.3).

Table 4.1. Measured conductivity and viscosity of LiTFSI in different solvents at 1:2 salt:solvent ratio. All the solutions are measured at 25°C.

	Conductivity ($mS.cm^{-1}$)	Viscosity (cP)	Viscosity-Conductivity product
MP	2.3	21.6	49.7
DMC	1.2	53.7	64.9
BC	0.2	323	64.6

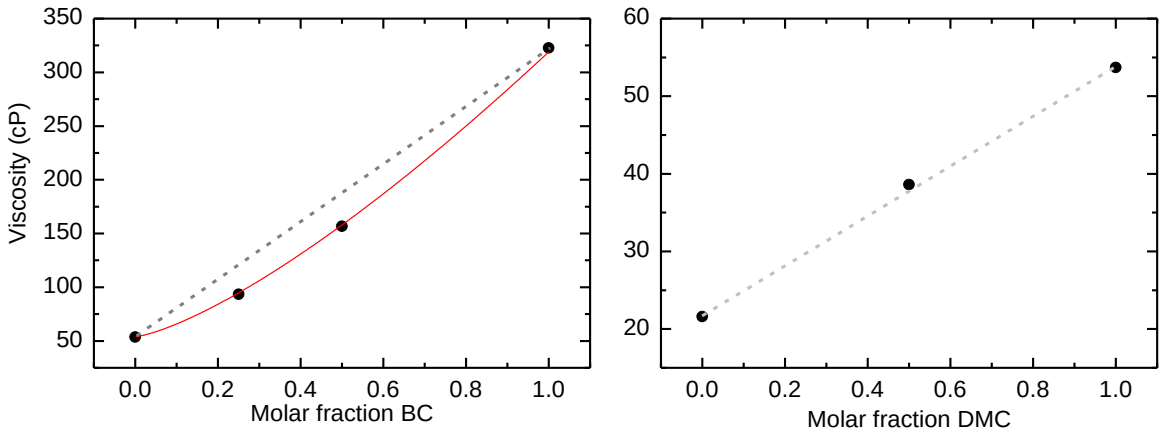

Figure 4.5. The viscosity of 1:2 lithium:solvent in mixture of BC/DMC (left) and DMC/MP (right).

The presence of the BC dimer between different Li^+ should impose a microscopic ordering to the solution that should manifest macroscopically. Indeed, the viscosity of the BC solutions exhibits the microscopic ordering at the macroscopic level since the electrolyte shows a viscosity more than six times larger than that of the MP and DMC electrolytes (Table 4.1). The difference between the viscosities of the electrolytes is due to the lack of dimerization in DMC or MP caused

by the absence of strictly planar structures in these two linear molecules.[245, 246] While one can propose that the difference in the viscosity is due to the interaction potential between the solvent molecule and Li^+, DFT computations predict a similar Li^+---solvent energetics for all the solvents (Figure 4.6). Furthermore, a non-linear change in viscosity is observed for electrolytes made of a mixture of BC and DMC, while the viscosity changes linearly for electrolytes made of DMC and MP, Figure 4.5. The non-linear behavior of the viscosity in the BC-DMC electrolyte evidences the non-ideal behavior of the BC-DMC solution due to the existence of the BC-BC dimer interaction, which is not present in the DMC-MP electrolyte. In terms of non-ideal solutions, the non-linear viscosity is a result of the excess free energy caused by the difference in the interaction potential between BC-BC, DMC-DMC, and DMC-BC.

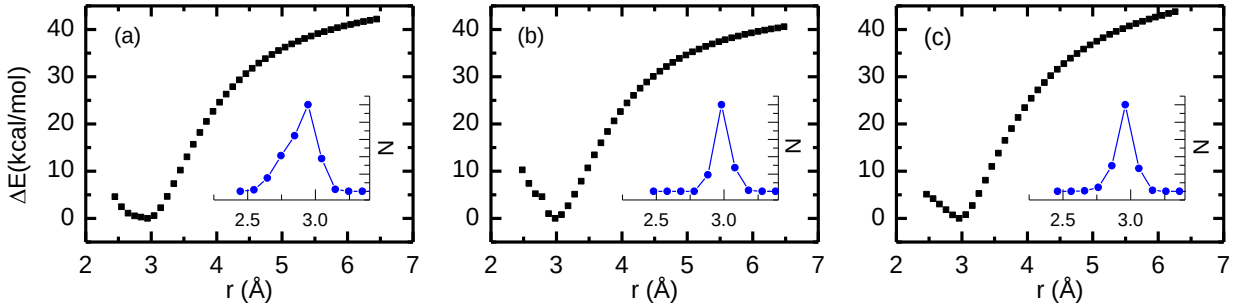

Figure 4.6. The potential energy scan as a function of the distance between the lithium cation and carbonyl carbon of each solvent: (a) MP, (b) DMC, and (c) BC. The insets represent the Boltzmann distribution in each system.

The results showed so far reveal that ionic and molecular species coordinate simultaneously the different lithium centers in high concentration electrolytes. In addition, the ordering in the molecular structure appears to extend beyond a single Li^+ due to the bridging of TFSI- and dimer formation only in the case of BC. The dynamics of the molecular components around the lithium center is investigated via 2DIR spectroscopy. In particular, the motions of the solvent molecules are derived from temporal dependence of decorrelation between pump and probe frequencies of the carbonyl stretch in the 2DIR spectra, which is computed by measuring

the nodal slope.[247] This decorrelation metric is usually assigned to the motions of the environment.[145] However, the carbonyl frequencies in coordinated band do not provide direct information of the molecular motions bound to Li^+, because the strong coupling gives rise to mixed states Equation (4.2).[116] Thus, the decorrelation of the mixed state frequencies does not have a direct correspondence with individual carbonyl frequency fluctuations and the FFCF dynamics represents a change in the geometrical structure of the carbonyl groups, i.e. the relative angle or the distance between carbonyl groups.[116]

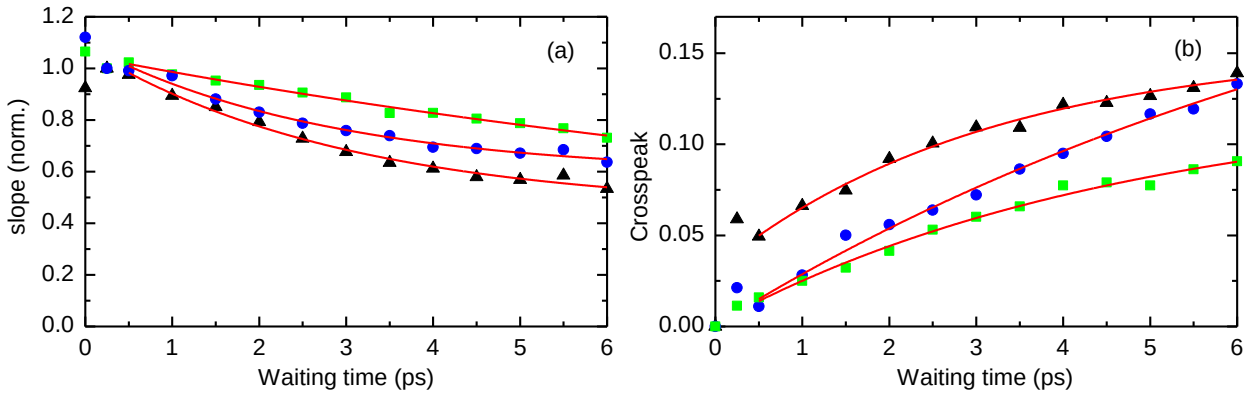

Figure 4.7. Inverse slope (normalized at 250 fs) of the coordinated carbonyl stretch, (a) and the cross peak growth, (b), of electrolytes made of MP (blue), DMC (black) and BC (green) at 1:2 molar ratio. The exponential fittings are represented with red lines.

The slope time evolutions for the carbonyl band of the three solutions are shown in Figure 4.7. The slope dynamics shows a decrease in its value with waiting time for all the samples and is well modeled with a single exponential decay of the form: $f(t) = y_o + Ae^{-t/\tau}$, where τ is the characteristic time of exponential decay. In this model, the exponential decay and the offset (y_0) represent two dynamical processes with fast and slow dynamics, respectively. The modeling parameters (Table 4.2) evidence that MP and DMC have fast decorrelation dynamics with a similar time scale of ~3 ps, but the amplitude of the slow dynamic component is larger for MP. In contrast, the dynamics for the fast component of the BC electrolyte presents an almost linear decay to zero

exposing the very slow motions shown by the BC molecules. In all samples, the second component (offset) of the FFCF dynamics is assigned to the interchange between possible arrangements of different Li^+ solvation shells. The assignment of slow motions to different solvation shell structures explains the large offset seen for MP and DMC (Table 4.2), since both molecules have a large number of conformers from their mobile alkyl chains. In addition, the conformational changes in MP and DMC perturb their molecular dipole directions[248] creating a large number of different solvent coordination angles, or equivalent, transitions. In contrast, the rigid structure of the cyclic carbonate and the formation of dimers significantly restrict the changes in the dipole direction and structure deformation, respectively. As a result, BC electrolytes present an overall slow dynamics with a negligible slow component.

Table 4.2.The calculated characteristic time of the slope (τ with amplitude of A and offset y_0) and the cross peak growth (τc with amplitude of B and offset z_0).

solvent	A	τ (ps)	y_0	B	τ_c (ps)	z_0
MP	0.50±0.02	2.8±0.5	0.59±0.03	0.26±0.07	9±3	0.27±0.07
DMC	0.62±0.03	3.0±0.4	0.45±0.03	0.12±0.01	3±1	0.15±0.01
BC	1.04±0.01	17.3±0.7	--	0.12±0.01	5±1	0.13±0.02

The 2DIR spectra also reveal the presence of cross peaks (Figure 4.2). While intra-band cross peaks originate from vibrational coupling between two or more vibrational modes,[249] the cross peaks between vibrational transitions corresponding to different chemical species are caused by chemical exchange.[250] In particular, the cross peak between the main carbonyl band and the high frequency band is proposed to arise from solvent molecules coordinating and de-coordinating from the lithium center. Note that this mechanism is not similar to that proposed by Cho and coworkers,[241] because these concentrated solutions are dominated by ion-ion interactions rather

than by ion-dipole interactions, as demonstrated by Watanabe group.[111] The dominating ion-ion interactions in the high concentration electrolyte allow us to postulate that the molecular mechanism behind the coordination and de-coordination of solvent molecules from Li^+ is a consequence of the change in the Li^+-TFSI- interaction. In particular, the variation in the ion-ion interaction is likely to arise from conformational changes of a nearby TFSI- since it has been previously shown that the energetics of the conformational change of TFSI- is low and thermally allowed.[251-253] In other words, the conformational changes of a TFSI- are likely to vary the total coordination number of a neighboring lithium center and as a result, a solvent molecule is expelled from the Li^+ solvation shell to reestablish the coordination number of four. However, the expelled or "free" solvent molecule will "rapidly" establish a new interaction with the same or another Li^+ due to the close proximity among lithium centers in the high concentration electrolyte (Figure 4.4). Hence, the existence of cross peaks between coordinated and free carbonyl bands evidences the formation and disappearance of transient states where the solvent molecule is temporally located in between lithium centers.

The proposed mechanism for the cross peaks observed in the 2DIR spectra was validated with the MD simulation. In this mechanism, the hypothesis in which coordination of TFSI- affects the number of solvent molecules interacting with the lithium center is first tested. To this end, the correlation between the number of oxygen atoms from BC carbonyl and TFSI- sulfone groups is derived from the MD simulations. The results show that the number of BC oxygen atoms and TFSI- ion are inversely correlated, Figure 4.8, with a correlation number of 0.73 indicating a strong correlation.[254]

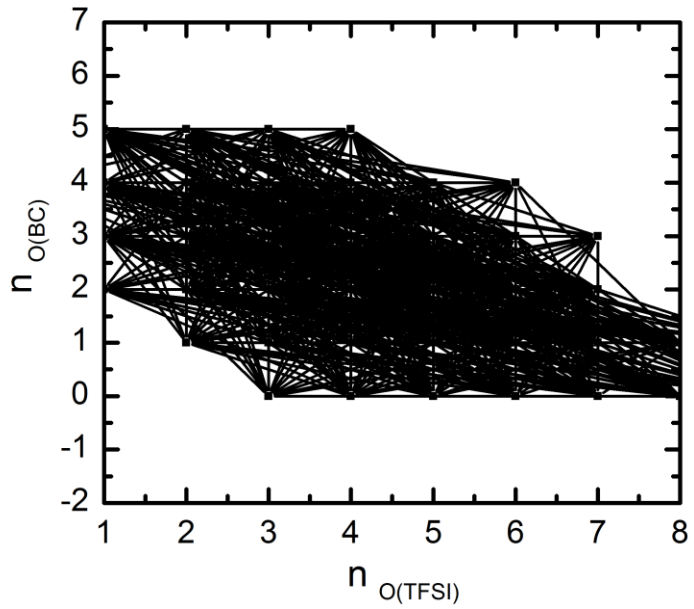

Figure 4.8. The number of oxygens of BC vs $TFSI^-$ ion which are coordinated to the lithium center.

$$Li(TFSI)(Solvent)_2 + TFSI \leftrightarrow Li(TFSI)_2(Solvent)_2$$

$$Li(TFSI)_2(Solvent)_2 \leftrightarrow Li(TFSI)_2(Solvent) + Solvent$$

Scheme 4.4. Molecular mechanism giving rise to the change in the coordination of Li^+.

The observed correlation between the number of species coordinating Li^+ demonstrates that the de-coordination of one BC molecule from the lithium center is in fact related to the changes in the coordination of TFSI-. Thus, a mechanism is proposed consisting of a TFSI- coordinating Li^+ rearrange to coordinate a different Li^+ and triggers the expulsion of the solvent molecule (Scheme 4.4).

In accordance with the proposed coordination and de-coordination model, the intensity of the cross peaks grows as a function of waiting time (Figure 4.7). Modeling of the cross peak growth with an exponential function reveals that the dynamics of the carbonyl coordination and de-coordination process is similar for the three solvent molecules (Table 4.2). However, it is apparent that MP has a larger time constant than the other two carbonates. To understand the difference in the dynamics, the potential energy between Li^+ and a solvent molecule was calculated via DFT

computations. Note that these calculations only consider a solvent molecule and a Li^+ because according to the mechanism the solvent exchange occurs from the same intermediate state (i.e., $Li(TFSI)_2(Solvent)_2$), which is the same for all the samples. The potential energy surfaces of the C=O…Li^+ coordinate for all the solvents show a similar potential barrier (Figure 4.6) indicating that the energetics is not responsible for the difference in the dynamics. However, the C=O…Li^+ potential surface reveals that the minimum the well is less concave for MP than for the other two solvents (Figure 4.6). In terms of Kramer's theory, the result demonstrates that MP will have a higher probability of remaining in the well, or equivalent, slow dynamics.[255] These theoretical calculations also establish that the trend of the chemical exchange dynamics is defined exclusively by the interaction potential between Li^+ and the carbonyl group of the solvent molecule.

The dynamics of the solvent coordination and de-coordination process was also derived from the MD simulation. The MD simulations reveal that there is a large variety of solvation shell structures as seen in the histogram of BC carbonyl oxygen atoms in the solvation shell of Li^+ (Figure 4.9). Hence, the chemical exchange rate is obtained from the residence time, which is defined as the time that a solvent molecule resides close to a lithium center.[256] In this case, a solvent molecule is considered to be residing a Li^+ if the oxygen of the carbonyl group is within 3.15 Å of Li^+. The autocorrelation function of the residence time (R(t)) of all the BC molecules in the trajectory was calculated as $\langle R(t)R(0)\rangle$. The correlation function (Figure 4.9) shows a temporal dependence that is well modeled with three exponential decays of the form: $f(t) = A_1 e^{-t/\tau_1} + A_2 e^{-t/\tau_2} + A_3 e^{-t/\tau_3}$, where A_i and τ_i correspond to the amplitude and the characteristic time of the i^{th} dynamical component, respectively. The characteristic times of the autocorrelation, as estimates of the time scale for the chemical exchange process, reveal components with time constants of ~10 ps, ~200ps, and ~1ns. While the fast correlation decay confirms that the

coordination and de-coordination of solvent molecules from the lithium center is a thermally allowed process with a picosecond time constant, the slow decays of the autocorrelation are likely to arise from the low probability of exchanging both solvent molecules simultaneously in agreement with the proposed mechanism (Scheme 4.4). This result further supports our hypothesis for the chemical exchange being the mechanism for the observed cross peaks between the coordinated and free peak of the carbonyl bands. In addition, the derived time constant for the chemical exchange dynamics is in reasonable agreement with the experimental one.

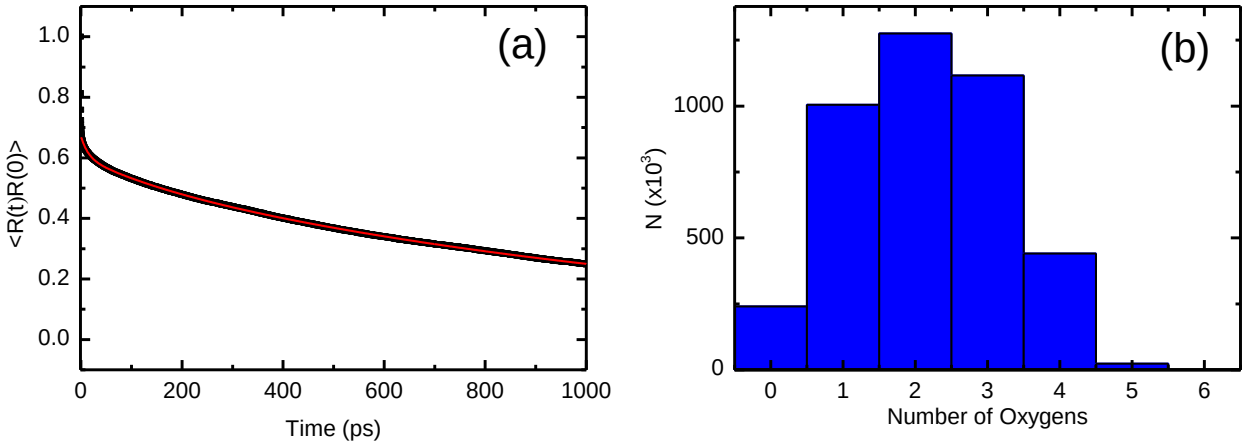

Figure 4.9.(a) The autocorrelation function (black squares) and modeling (red line) of the residence time of O-BC at the cutoff value of 3.15 Å from the lithium center and (b), the histogram of number of oxygen resides within the cutoff value.

The coordination and de-coordination of the solvent molecule is a consequence of the change in the coordination of TFSI- with the lithium center. This mechanism is expected to be the same molecular mechanism that enables charge transport through the high concentration electrolyte and was previously postulated by Watanabe group.[100, 101, 103] In particular, it has been proposed that the exchange of the solvent/anion from the lithium centers in a solvent/anion bridged-structured electrolyte results in a hopping-based (non-vehicular) conduction mechanism in lithium bis(fluorosulfonyl)amide (LiTFS) based electrolytes.[101, 103] Hence, we propose the same

type of ionic conduction mechanism exists for the high concentration electrolytes studied here. This proposed conduction mechanism is supported by the high conductivity exhibited by all the electrolytes (Table 4.1) since a high conductivity is not expected via a vehicular type conduction mechanism in electrolytes dominated by ion-ion interactions.[66] In the case of the three investigated electrolytes, the conductivity of the cyclic carbonate based electrolyte appears to be lower than that of its linear analogues. However, the viscosity weighted conductivities (Table 4.1) show similar values, indicating all electrolytes should have the same number of charge carriers.[66] Furthermore, it is observed that the MP electrolyte has the lower viscosity-weighted conductivity and the slower chemical exchange dynamics, while DMC and BC have the faster exchange dynamics and the higher viscosity-weighted conductivities. The observed correlation between conductivity and chemical exchange rate arises from the close relationship between the number of TFSI- and solvent molecules coordinating the same Li^+, as previously demonstrated. In other words, the coordination and de-coordination of solvent molecules directly track the change in the TFSI- coordination type and number to a lithium center. Thus, the exchange of solvent molecules from Li^+ solvation shell directly follows the making and breaking of ionic structures in the high concentration electrolyte, or equivalent, and its conductivity; giving that the change of the TFSI- coordination to Li^+ is the molecular process most related to the conductivity,

4.5 Conclusion

The structural interactions and the motions of three different high concentration electrolytes were investigated. The linear vibrational spectra and DFT calculations suggested that the anions and solvent molecules present a similar coordination with the lithium center in the three electrolytes. The experiments also reveal the presence of multiple anions coordinating with the lithium centers, which creates short range ordered clusters in all the electrolytes. The presence of

additional interaction in cyclic carbonate based electrolyte is also derived. This interaction results in the formation of BC dimers from molecules coordinated to different Li^+ and this gives rise to an additional structural ordering in the BC electrolyte, which is directly observed in its viscosity. Our experiments also reveal that the process of coordination and de-coordination of solvent molecules from lithium centers is directly related to the coordination between the anion and the cation. However, the characteristic time of the chemical exchange process is found to be governed by the chemical nature of the solvent molecules. Overall, our experiments reveal the connection between the molecular characteristic of the electrolyte components and indicate that small changes in the solvent-solvent interaction potential have drastic effects in the macroscopic properties of the electrolytes, such as its viscosity.

CHAPTER 5. IONIC CONCENTRATION CHANGES IN BATTERY ELECTROLYTES UNDER ELECTRIC FIELD: AN IN-SITU IR SPECTROSCOPIC STUDY

5.1 Introduction

Over the past three decades, lithium-ion battery technology has been dominant in the energy storage fields due to the high energy density. However, the expansion of the current lithium-ion battery technology to fields such as automobile and grid energy storage has brought the attention of the scientific community to perform constant modifications to the current technology. The electrolyte is one of the main components of the battery which sometimes becomes the performance limiting factor of the overall battery, i.e operating voltage, charging and discharging rate, working temperature, etc. A new class of electrolyte system is currently being tested to replace state of the art carbonate-based electrolytes with better performance and better safety features. Therefore, numerous studies have been performed to understand the microscopic structural and dynamical factors that determine the properties of these electrolytes.

The solvation structure of the lithium in organic-based solvents has been investigated using different tools, IR spectroscopy,[113-117] Raman spectroscopy,[118-123] NMR,[123-127] X-ray scattering,[130, 131] computational studies.[225, 228, 257-259] However, only the time-resolved IR techniques have the ability to capture the fast picosecond scale dynamic processes in these systems.[113] Nevertheless, now it is the common understanding that the current $LiPF_6$/carbonate-based electrolytes are composed of free lithium ions, which are coordinated in a tetrahedral manner by four carbonates, solvent separated ion pairs, where a close by anion participate in the first solvation-shell of lithium, and contact ion pairs, in which direct contact between lithium and anion is observed.[115, 116, 235] In addition, a sub-picosecond scale chemical exchange mechanism of the solvent molecules has been identified in these electrolyte systems.[235] However, most of these findings are performed when the

electrolyte is at rest, i.e. no external electric field. While the solvation-shell at rest is important in developing better electrolytes, the understanding of solvation-shell and ionic speciation during the charging and discharging processes provide more insight into electrolyte development. The electrolytes can experience concentration polarization during the working conditions due to the relatively different transference numbers and salt diffusion coefficients of ions and also the formation of a solid electrolyte interface.[260] Hence, the solvation structure and dynamics of the lithium ions are essentially different from that of the lithium ions at rest condition. Further, the heterogeneity of the electrolyte medium reflects the resistance of ion diffusion processes. Thus, understanding of concentration profile, ionic speciation, and dynamics of electrolytes during the working conditions provides more information that is required to improve the quality of the battery electrolytes.

Several in-situ studies about the ionic concentration distribution of an electrolyte between two electrodes have been reported in the literature. Matilda *et al.* discover an in-situ way to map the lithium-ion concentration of an electrolyte using NMR for the first time.[261] The pulse field gradient NMR allowed them to directly probe the ^{7}Li concentration in the electrolyte. The conventional 1M $LiPF_6$ based electrolyte system was placed between two lithium metal electrodes where the separation is about 10 mm. Additionally, the viscosity of the electrolyte was increased with the addition of a polymer to reduce the ionic convection. They observed approximately a 40% - 60% change in the lithium concentration at each electrode after several hours of constant current through the cell. Following their work, a few other in-situ NMR studies of mapping of lithium concentration are reported using an improved version of the cell.[260, 262, 263] Importantly, Sergey *et al.* were able to clearly identify the concentration gradients of both cation and anion on anode and cathode through ^{7}Li and ^{9}F probes and the gradients appeared in lesser time compared to Matilda

et al. work due to the shorter distance between the electrodes.[260] Chien *et al.* were able to reduce the separation between the electrodes by using a solid electrolyte system which is made of $Li_{10}GeP_2S_{12}$ and observed a similar result.[264] The cell design in these NMR techniques results in a millimeter-scale separation between the electrodes while the electrode separation is in the micrometer scale in real batteries. Raman microscopic techniques have been employed to observe the concentration profile of the electrolytes in which the electrodes are placed in real battery configurations.[265-268] While most of the Raman studies focus on morphology around the electrodes or the solid electrolyte interface, the study by Brissot *et al.* observed a clear difference between the optical absorbance of probe molecule which is similar to NMR studies.[266] Neverthless, none of these studies provides a comprehensive picture of the solvation studture of lithium ions under the influence of external electric field. In addition, the lack of time resolution in these techniques hinders the ability to obtain the fast dynamical changes that undergo during the battery operational conditions.

Therefore, in this study, we conducted an initial approach to observe the structural and dynamical information of battery electrolytes during the operational conditions using linear and multidimensional IR tools which have the time resolution to observe fast dynamical changes occurring in these systems. However, the experimental setup and techniques used in this project are still in the initial stage and require further improvement to observe the microscopic structural characteristics. Nevertheless, our results suggested that a concentration gradient in the electrolyte is built when an external electric field is applied to the cell.

5.2 Methodology

5.2.1 Sample preparation

Lithium thiocyanate(hydrated, $LiSCN.12H_2O$) was obtained from Alfa Aesar and dried at 140°C for 48 hours before use. Lithium tricyanomethanide - Acetonitrile Complex ($LiC_4N_3.CH_3CN$, >98%) was obtained from TCL chemicals and used without further treatment. Lithium 4,5-dicyano-2-(trifluoromethyl)imidazole (LiTDI, >95%) was obtained from Alfa Aesar and dried at 140 °C for 15 h under vacuum before use. Lithium bis(trifluoromethylsulfonyl)imide (LiTFSI, $LiN(SO_2)_2(CF_3)_2$, > 98%) was obtained from Alfa Aesar and dried at 130°C for 24 hours before use. Poly(methyl methacrylate) (molecular weight ~ 30 000 $gmol^{-1}$) was obtained from Acors Organics and used without further treatment. 1,2-butylene carbonate (BC, $C_5H_8O_3$, 98%) was obtained from TCI Chemicals. acetonitrile (ACN, 99%) was obtained from Fisher Biotech. All solvents were dried with 1-2mm molecular sieves for 24 hours prior to use. All lithium solutions were prepared by simply mixing the components inside a N_2-filled glovebox at room temperature. However, for the last experiment polymethyl methacrylate (PMMA) (40%) was added to 10 mM lithium thiocyanate in acetonitrile solution. The addition of the polymer into the electrolyte system serves in two ways to improve the quality of the experiment. First, it increases the viscosity of the electrolyte and that results in a slow down of ionic diffusion and convection. Second, the polymer enforces the interaction between lithium and thiocyanate and allows us to observe different ionic speciations in the electrolyte system.

5.2.2 Cell Design

The typical FTIR cell with a pair of 2 mm round CaF_2 windows was used for the measurement. The cell electrodes were prepared by cutting 25 µm aluminum foil in a quarter circle shape with a tail to connect to the external power supply. The electrodes were placed on the top

and bottom edges of the CaF_2 window leaving the middle part to drop the electrolyte solution. The electrodes and the electrolyte were then sandwiched with the other CaF_2 window.

For every experiment, the initial spectrum is obtained when the cell was at 0V. During the LiTDI experiment, the cell voltage was increased until a considerable amount of current passes through the cell (8 μA) and then maintained the constant voltage through the cell. The FTIR spectrum was collected every 5 minutes for 30 minutes. Note that the current through the cell kept decreasing during the experiment indicating either the formation of the solid electrolyte interface or the polarization layer on the electrodes.

5.2.3 Linear IR Spectroscopy

Fourier transform infrared (FTIR) experiments were performed using a Bruker Tensor 27 spectrometer with 0.5 cm^{-1} resolution and liquid nitrogen cooled narrow band MCT detector. All samples were measured in transmission mode. Each FTIR spectrum was recorded as an average of 10 individual scans at 25 °C.

5.2.4 Two dimensional IR spectroscopy

Two dimensional infrared experiments were conducted using a similar way which was previously described.[221] Briefly, the combined 5 kHz repletion rate Ti:Sapphire amplifier (Spectra Physics Mai Tai and Spitfire) with an optical parametric amplifier (Spectra Physics, 800C) and a difference frequency generation crystal ($AgGaS_2$) produces ~60 fs broadband infrared pulses. The generated pulses were equally split into three pulses (k_1, k_2 and k_3) and later focused on the sample with a boxcar configuration.[145] The time intervals between each pulse: τ (first pulse and the second pulse), T_w (second and third pulse) and t (third pulse and the photon echo) were controlled with four computer controlled translational stages (PI Micos). The generated photo echo with pulses with parallel polarization (<XXXX>) in the phase matching direction ($-k_1+k_2+k_3$) was heterodyned

with a fourth pulse (local oscillator) and later dispersed by a Triax monochromator. Finally, the non-linear signal and local oscillator were detected with a liquid nitrogen cooled 64 element MCT array detector (Infrared Systems Developments). Here, 2D IR data were collected by scanning τ time from -3 ps to +3 ps in increments of 5 fs for each waiting time in order to collect both the rephasing and non-rephasing data by switching the time ordering.[145] Signals were collected for a few waiting times. In all the measurements, the local oscillator always preceded the photon echo signal by ~4.5 ps. The time domain signal, collected as a function of (τ, T, λ_t) via a monochromator-array detection, is transformed into the 2DIR spectra (ω_τ, T, ω_t) by means of Fourier transforms. A detailed explanation of the Fourier analysis has been described elsewhere.[175]

5.3 Results and Discussion

The characteristics of the lithium solvation-shell under the influence of an external electric field are initially studied with linear infrared spectroscopy. Unlike the ^{7}Li NMR techniques, the IR spectroscopy cannot directly probe the lithium concentration in the electrolyte. Thus, the lithium concentration profile is indirectly obtained by probing a suitable anion that has vibrational modes sensitive to the environment. TDI ions in a 10mM LITDI in butylene carbonate (BC) electrolyte system are used as the first reporter of the concentration gradient in a lithium electrolyte. The nitrile band of TDI ion in the region of 2200 cm^{-1} to 2250 cm^{-1} is identified to be a good and sensitive IR reporter in several molecular systems.[132, 269]

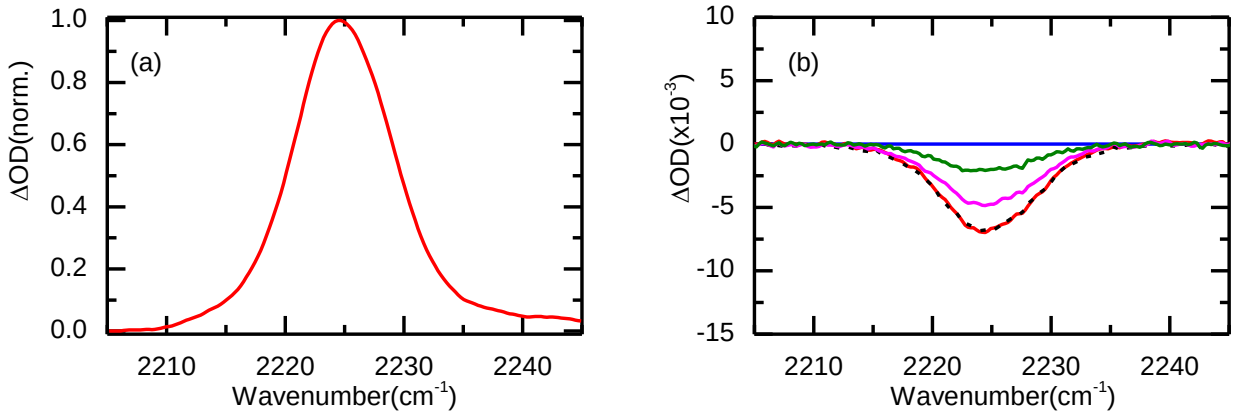

Figure 5.1. The normalized FTIR nitrile band of the 10 mM LiTDI in BC (left). The right plot shows the difference spectra of 0V[initial]-0V[initial] (blue), 5.2V-0V[initial] (red), 0V[0 mins]-0V[initial] (black-dashed), 0V[200 mins]-0V[initial] (pink) and 0V[900 mins]-0V[initial] (green).

The first graph of Figure 5.1 represents the normalized nitrile band which appears to be a single peak centered at ~2225 cm^{-1}. The TDI ions are expected to be in free form at 10 mM concentration due to the strong dielectric medium of BC.[20, 270] In fact, the peak at 2225 cm^{-1} was assigned to be the free ion band in a previous study.[132] During the experiment, the linear IR spectra at two different voltages, 0V and 5.2V, were collected and the IR beam was directed close to the negative terminal.

The difference spectrum of the FTIR collected at 5.2V and FTIR collected at 0V, Figure 5.1(b), shows a decrease in the intensity of the free TDI band which is a result of a change in TDI concentration at the negative electrode. It is reasonable to assume that the positive and negative ions move along and against the external electric field, respectively, and eventually create a concentration gradient in the electrolyte. However, a combination of undergoing effects such as ionic diffusion, ionic migration, convection, and redox reactions at the electrodes are responsible for an event of concentration gradient build-up.[271, 272]Therefore, the experimental evidence shows that the migration of the ions due to the external electric field overcomes the effects of the ionic diffusion, which occurs due to the concentration gradient, and ionic convection, which is a result

of the thermal random movement of the ions. In addition, the slower electrochemical reactions at the electrodes compared to the ionic migration will help to build a concentration gradient in the electrolyte system.

The TDI ion concentration at the negative electrodes starts increasing upon the disconnection (and short-circuited) of the cell, Figure 5.1. Blue dotted line is the immediate difference spectrum after the disconnection, pink and green lines are the difference spectra at 200 and 900 minutes. This clearly indicates that the concentration gradient vanishes with time due the ionic diffusion and convection. However, the recovery process is extremely slow compared to the initial concentration gradient build-up process. Note that the cell never recovered to the original concentration, or at least during the experimental time window, which indicates that some of the TDI ions might have consumed during the electrochemical reaction at the negative electrode, hence lowering the overall TDI concentration in the cell electrolyte.

The usual electrochemical window of the BC-based electrolytes varies around 4.2 V, but the cell was kept at 5.2 V during the first part of the experiment.[273] This might result in oxidation of the solvent molecules during the initial part of the experiment and affects the final linear IR spectra. The decrease in solvent molecules of the cell should increase the TDI concentration of the electrolyte and increase the band intensity of the spectrum. However, this effect can be negligible compared to ionic migration since the free TDI band kept decreasing while the electric field is applied and the band intensity never increased beyond the original intensity during the recovery process. One can also assume the changes observed in the difference spectra are only due to the heating effects that arise as a current passes through the electrolyte. Therefore, a controlled experiment with a lower current and a lower voltage with a different vibrational probe was performed.

The first graph of Figure 5.2 shows the asymmetric stretching of the nitrile groups of tricyanomethanide ion (TCM) in the region of 2130 cm^{-1} to 2200 cm^{-1}. The TCM was identified to be a good and sensitive vibrational reporter due to the coupled nitrile transitions, hence a small perturbation to the ion will split the asymmetric degenerate states and give rise to an additional peak.[274, 275] The linear IR spectra at 0 V is fairly symmetric indicating most ions are in free form. The TCM band that was collected close to the negative electrode starts to decrease upon applying an external voltage of 0.5 V, and the measured current was approximate 1 µA through the cell. The difference spectrum (black) shows a clear decrease in the band after 225 minutes of the external voltage. Note that the change in the absorption band is significantly smaller in TCM ion compared to the TDI ion due to the different conditions used in two experiments. However, it is worth mentioning that the transition dipole of TCM is much greater than that of TDI ion,[274] thus, the TCM probe shows larger changes in the spectrum with the smaller changes in the concentration compared to the TDI probe. The time that took to establish a considerable amount of concentration gradient is high compared to the previous experiment indicates that the ionic migration due to the external field is in a similar order as of ionic diffusion and convection.

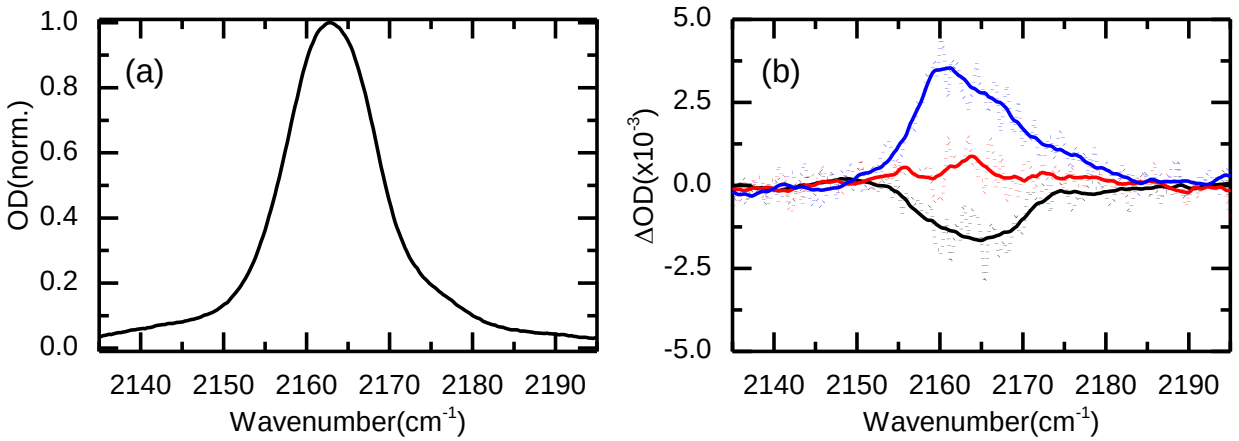

Figure 5.2. The linear spectrum of 10 mM LiTCM in BC (left). The right graph represents the difference spectra of 0.5V[225 mins]-0V[initial] (black), 0V[840 mins]-0V[initial] (red),

0.5V[480 mins]-0V[initial] (blue), each dotted plots represents the raw data and smooth data is represented by solid lines.

The built-up concentration gradient was recovered to the original concentration after 840 minutes of the short-circuited cell. The smoothed difference spectrum shows no significant changes in the TCM band and the raw difference spectrum shows only the experimental noise. This further confirms that the ionic migration, diffusion, and convection were at a similar rate in this experiment. In addition, the decomposition of the solvent molecules does not play a role in this system since the operating voltage is way more below the redox potential of the solvent.[273] An increase of the TCM band is observed when the external potential is applied in the reverse directions, i.e. change the electrode polarization to be positive. The difference spectrum of FTIR collected after 480 minutes and FTIR collected at 0V clearly shows a positive peak in the TCM region. This confirms that the changes observed in the linear IR spectra are not the result of heating effects that arise due to a current passes through the cell.

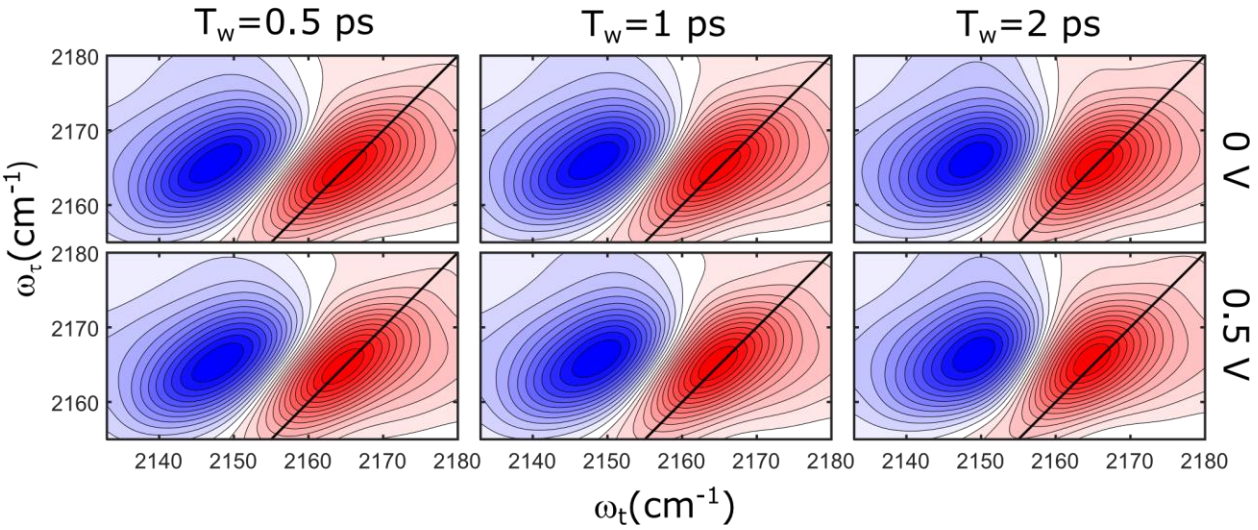

Figure 5.3. The 2DIR spectra of 10 mM LiTCM in BC at 0V (top row) and 0.5V (bottom row) and the three columns represent spectra collected at different waiting times.

The changes that occur when an external electric field is applied were investigated by means of two dimensional infrared spectroscopy. Figure 5.3 shows the 2DIR spectra collected at

three different waiting times for the system being at 0 V and 0.5 V. In each spectrum, a pair of peaks along the diagonal line is present and the red contours (positive peak) [at ω_τ, ω_t= ~2165,~2162] corresponds to the transition between the vibrational ground state and first excited state ($\nu = 0 \leftrightarrow 1$) and the blue contours (negative peak) [at ω_τ, ω_t= ~2165,~2145] arises due to the vibrational transitions between first and second excited states ($\nu = 1 \rightarrow 2$). The negative peak is redshifted by ~17 cm^{-1} due to the anharmonicity of the asymmetric stretching of the nitrile bands. As observed from the linear IR spectra, only a single peak is observed on the positive peak that corresponds to the free ion. The time evolution shows that the elongated peaks are getting rounder in shape at higher waiting times.

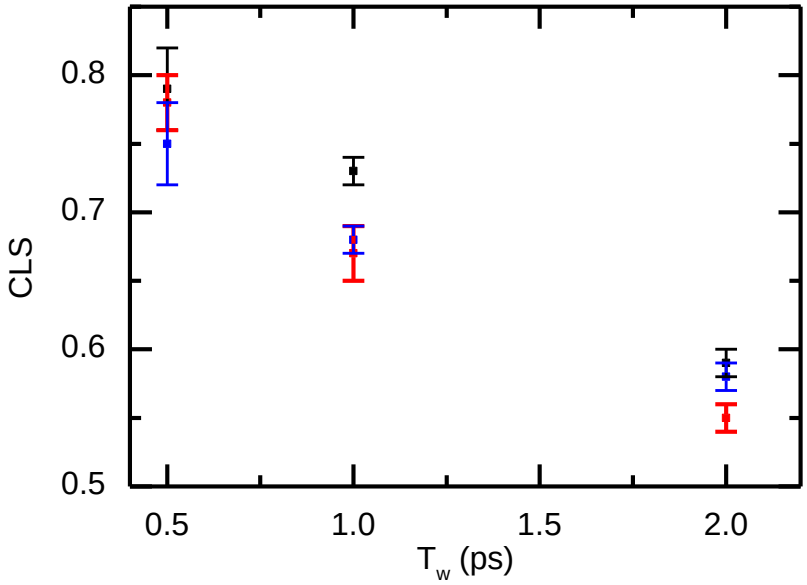

Figure 5.4. The central line slope values at different voltages, 0V [0 mins] (black), 0.5V [120 mins] (red) and 0.5V [240 mins] (blue).

The change in peak shape with the waiting time, called spectral diffusion, arises due to the loss of correlation between the pump frequency and probe frequency as a result of the fluctuations in the molecular environment. The spectral diffusion is quantified by calculating the central line slope (CLS)[149] of each spectrum and compared the values to determine the effects on the

concentration gradient by the external field. Figure 5.4 shows that the CLS values of each waiting time at 0 V and 0.5 V are similar within the experimental error. While it is tempting to assume the dynamics of the ions is faster when the electric field is applied due to the external force on ions, the ionic ordering along the field makes the dynamics slower. However, the real dynamical effects are not observed within the experimental time window of the 2DIR experiment which is mainly determined by the vibrational lifetime of the molecular probe. Thus, a proper molecular reporter with a larger vibrational lifetime is required to see the possible slower dynamical changes that may occur when an electric field is passed through the cell.

So far, the molecular probes under-study characterize the build-up of the concentration gradient through free band growth or decrease and it is still missing the vital information of the speciation changes under the external field. To this end, the polymer electrolyte system was used. It is worth mentioning that increase of the salt concentration of the electrolyte will benefit from consisting of different ionic speciations, but it will hinder the ability to distinguish very small population changes of the species due to the large ensemble-averaged IR measurements.

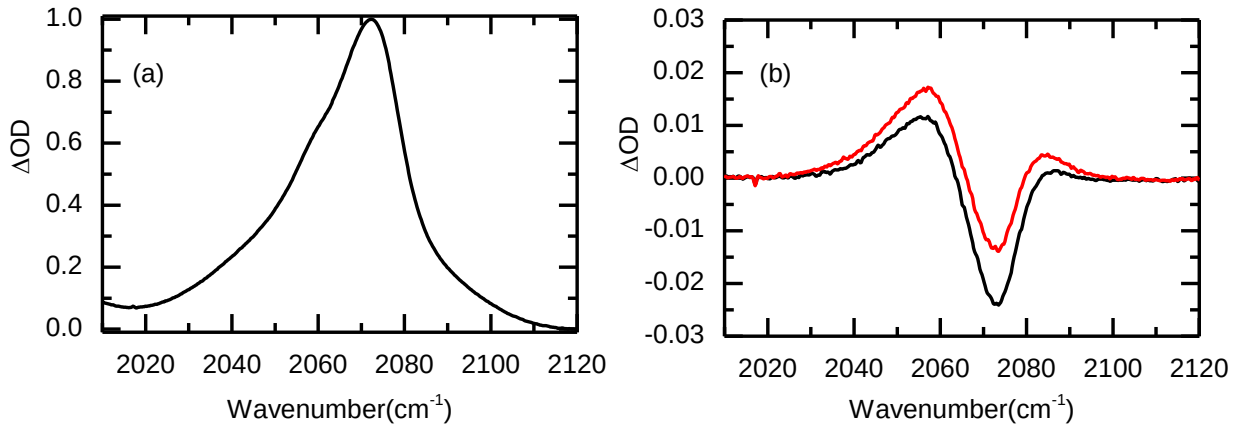

Figure 5.5. The linear IR spectrum of 10 mM LiSCN in ACN/40%PMMA (left). The right graph represents the difference spectra of 2V[3hrs]-0V[initial] (black) and 0V[26 hrs]-0V[initial] (red).

The first graph of Figure 5.5 represents the nitrile stretch of thiocyanate ion in the region of 2010 cm^{-1} to 2120 cm^{-1} and the band centered around 2072 cm^{-1} with a tail on the lower

frequency side. Thiocyanate ion has been previously used as a probe in different molecular systems due to the high sensitivity to the environment.[135, 221] In addition, the thiocyanate ion was identified to have a free ion peak around 2050 cm^{-1}, ion paired peak around 2060 $cm^{-1,}$ and aggregates around 2080 cm^{-1} in several systems.[221] Thus, it can be inferred that the thiocyanate mainly presents as the aggregate form in the electrolyte system under study and the lower frequency tail indicated the presence of free and ion paired species. The cell was then connected to a 2 V external electric field where the current passes through the cell was recorded as 1 μA and the linear IR spectra were collected near the positive electrode in every 15 minutes for 5 hours. The difference spectrum of FTIR collected at 2 V (after 3hrs) and 0 V, black curve of Figure 5.2(b), shows a decrease in the aggregate peak and an increase in the free/ion paired peak indicating the breaking of aggregate into free ions and ion paired at the positive electrode as a result of lithium ions and thiocyanate ions move away and move towards the positive electrode, respectively. While this result agrees with the building of concentration gradient in the sample, the recovery process of the free ion and ion pairs, when the cell is short-circuited, do not follow the expected trend, rather kept increasing. Note that the viscosity of the electrolyte systems is relatively high, hence the ionic diffusion and convection rates are expected to be slower to establish the initial equilibrium state. However, the aggregate peak kept increasing after short-circuited the cell indicating the reformation of aggregates occurs on a faster time scale. Nevertheless, the reproducibility of this experiment was questionable.

The 2DIR tool can be used to distinguished the fast chemical exchange processes where the probe molecules undergo different chemical speciations between the pump and probe pulses. Figure 5.6 shows the measured 2DIR spectra at two waiting times for both 0 V and 2 V (after 3hrs). At early waiting times, the positive peaks are elongated along the diagonal line and show

the presence of multiple peaks as observed from the linear spectra. The two peaks are well resolved at higher waiting times due to the spectral diffusion. It is interesting to observe cross peaks [at ω_τ, ω_t= ~2060,~2078 and at ω_τ, ω_t= ~2076,~2035] [at ω_τ, ω_t= ~2050,~2062] even at 0 V. This indicates the thiocyanate is involved in the exchange mechanism that is stated in equation (5.1) at room temperature. However, the cross peak intensities remain unchanged upon the external electric field which implies the rate of breaking the aggregates into free or ion pairs is not affected by the external field, rather the rate-limiting step is governed by the thermal motions.

$$[Free\ ion] \leftrightarrow [ion\ pairs] \leftrightarrow [aggregates] \tag{5.1}$$

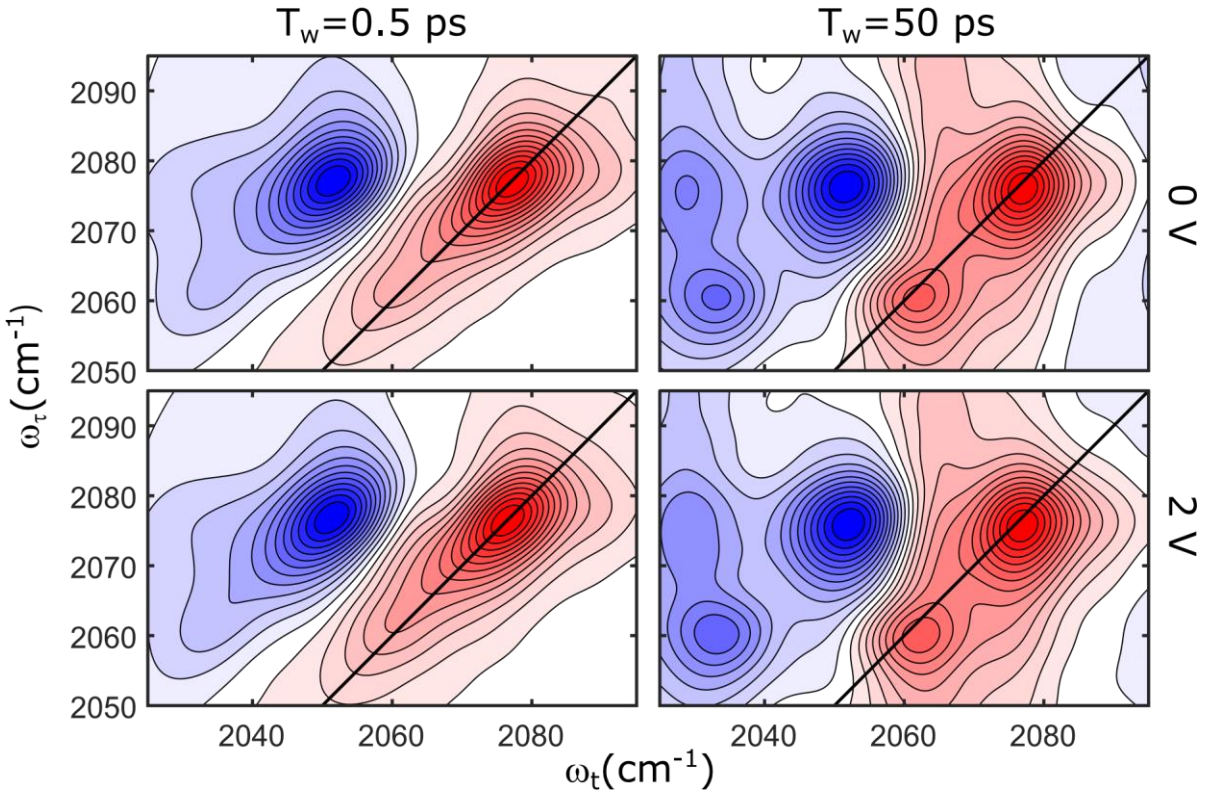

Figure 5.6. The 2DIR spectra of 10 mM LiSCN in ACN/40% PMMA measured at two waiting times for 0V and 2V.

All the experiments performed so far support the idea of building a concentration gradient in the electrolyte once the cell is connected to an external voltage source, but to obtain such a

concentration profile along the electrolyte space coordination is quite challenging in our FTIR setup due to relatively comparable IR beam size to the separation between the electrodes. Therefore, a modified setup with a smaller beam is required to obtain a proper electrolyte concentration profile. In addition, the separation between the electrodes is in the micrometer scale in real batteries, hence, the sample cell or the measurement technique needs to be modified to imitate the real battery conditions. Moreover, the contact area of the electrodes in these experiments is very low compared to the real batteries conditions, thus preventing the rate of the ionic migration under the influence of the electric field. This restriction was imposed in these experiments in order to keep the optical density of the sample within a reasonable value.

5.4 Conclusion

The concentration profile of an electrolyte system in an external electric field was investigated by IR spectroscopy. Initially, a dilute electrolyte system composes of LiTDI was studied by indirectly probing the lithium concentration. The nitrile vibrational mode of TDI ion showed a change in the concentration with the external voltage and the changes were slowly recovered upon the disconnection of the cell from the external source. The observed effects were confirmed with a similar experiment where a TCM ion was used to probe the concentration changes. The changes of the spectra in opposite directions upon the switching of the voltage polarization further confirm the build-up concentration profile in the electrolyte. The slower dynamical changes that occur with the external field could not observe from the time-resolved IR spectroscopy due to the probe's shorter vibrational lifetime. The final experiment reveals the changes in the ionic speciation and their dynamics with the electric field. The requirements of further development of the methods and techniques were identified to properly obtain the structural and dynamical information of these systems.

APPENDIX A: COPYRIGHT RELEASE 1

Molecular structure and ultrafast dynamics of sodium thiocyanate ion pairs formed in glymes of different lengths. S. R. Galle Kankanamge and D. G. Kuroda, *Phys. Chem. Chem. Phys.*, 2019, 21, 833

DOI: 10.1039/C8CP06869K

(link)https://pubs.rsc.org/en/content/articlelanding/2019/CP/C8CP06869K

Reproduced by permission of The Royal Society of Chemistry

RE: Permission Request Form: Susith Rajitha Galle Kankanamge

CONTRACTS-COPYRIGHT (shared) <Contracts-Copyright@rsc.org>

To: Susith R Galle Kankanamge <sgalle3@lsu.edu>

Many thanks for sending the permissions request below. The Royal Society of Chemistry (RSC) hereby grants permission for the use of your paper(s) specified below in the printed and microfilm version of your thesis. You may also make available the PDF version of your paper(s) that the RSC sent to the corresponding author(s) of your paper(s) upon publication of the paper(s) in the following ways: in your thesis via any website that your university may have for the deposition of theses, via your university's Intranet or via your own personal website. We are however unable to grant you permission to include the PDF version of the paper(s) on its own in your institutional repository. The Royal Society of Chemistry is a signatory to the STM Guidelines on Permissions (available on request).

Please note that if the material specified below or any part of it appears with credit or acknowledgement to a third party then you must also secure permission from that third party before reproducing that material.

Please ensure that the thesis states the following:

Reproduced by permission of The Royal Society of Chemistry

and include a link to the paper on the Royal Society of Chemistry's website.

Please ensure that your co-authors are aware that you are including the paper in your thesis.

Best wishes,

Chloe Szebrat
Contracts and Copyright Executive
Royal Society of Chemistry
Thomas Graham House
Science Park, Milton Road
Cambridge, CB4 0WF, UK
www.rsc.org

APPENDIX B: COPYRIGHT RELEASE 2

Molecular Structure, Chemical Exchange, and Conductivity Mechanism of High Concentration LiTFSI Electrolytes. Susith R. Galle Kankanamge and Daniel G. Kuroda., *The Journal of Physical Chemistry B* 2020 *124* (10), 1965-1977.

DOI: 10.1021/acs.jpcb.9b10795

(link)https://pubs.acs.org/doi/full/10.1021/acs.jpcb.9b10795

support@services.acs.org <support@services.acs.org>
Wed 10/28/2020 7:24 PM
To: Susith R Galle Kankanamge <sgalle3@lsu.edu>

ACS Chemistry for Life®

Dear Susith,

Thank you for contacting ACS Publications Support.

Your permission requested is granted and there is no fee for this reuse. In your planned reuse, you must cite the ACS article as the source, add this direct link **https://pubs.acs.org/doi/full/10.1021/acs.jpcb.9b10795**, and include a notice to readers that further permissions related to the material excerpted should be directed to the ACS.

If you need further assistance, please let me know.

Sincerely,
Keith Pearl
ACS Publications Support
Customer Services & Information
Website: https://help.acs.org/

REFERENCES

1. Bose, B. K., Global energy scenario and impact of power electronics in 21st century. *IEEE Trans Ind Electron* **2012,** *60* (7), 2638-2651.

2. Martins, F.; Felgueiras, C.; Smitkova, M.; Caetano, N., Analysis of fossil fuel energy consumption and environmental impacts in European countries. *Energies* **2019,** *12* (6), 964.

3. Ediger, V. Ş., An integrated review and analysis of multi-energy transition from fossil fuels to renewables. *Energy Procedia* **2019,** *156*, 2-6.

4. Al-Shetwi, A. Q.; Hannan, M.; Jern, K. P.; Mansur, M.; Mahlia, T., Grid-connected renewable energy sources: Review of the recent integration requirements and control methods. *J Cleaner Prod* **2020,** *253*, 119831.

5. Scrosati, B., History of lithium batteries. *J Solid State Electrochem* **2011,** *15* (7-8), 1623-1630.

6. Ruetschi, P., Review on the lead—acid battery science and technology. *J Power Sources* **1977,** *2* (1), 3-120.

7. Vincent, C. A., Lithium batteries: a 50-year perspective, 1959–2009. *Solid State Ionics* **2000,** *134* (1-2), 159-167.

8. Brandt, K., Historical development of secondary lithium batteries. *Solid State Ionics* **1994,** *69* (3-4), 173-183.

9. Diouf, B.; Pode, R., Potential of lithium-ion batteries in renewable energy. *Renewable Energy* **2015,** *76*, 375-380.

10. Wagner, F. T.; Lakshmanan, B.; Mathias, M. F., Electrochemistry and the future of the automobile. *J Phys Chem Lett* **2010,** *1* (14), 2204-2219.

11. Etacheri, V.; Marom, R.; Elazari, R.; Salitra, G.; Aurbach, D., Challenges in the development of advanced Li-ion batteries: a review. *Energy Environ Sci* **2011,** *4* (9), 3243-3262.

12. Barghamadi, M.; Kapoor, A.; Wen, C., A review on Li-S batteries as a high efficiency rechargeable lithium battery. *J Electrochem Soc* **2013,** *160* (8), A1256.

13. Marom, R.; Amalraj, S. F.; Leifer, N.; Jacob, D.; Aurbach, D., A review of advanced and practical lithium battery materials. *J Mater Chem* **2011,** *21* (27), 9938-9954.

14. Aurbach, D.; Talyosef, Y.; Markovsky, B.; Markevich, E.; Zinigrad, E.; Asraf, L.; Gnanaraj, J. S.; Kim, H.-J., Design of electrolyte solutions for Li and Li-ion batteries: a review. *Electrochim Acta* **2004,** *50* (2-3), 247-254.

15. Balbuena, P. B.; Wang, Y., *Lithium-ion batteries: solid-electrolyte interphase*. Imperial college press: 2004.

16. Manthiram, A., An outlook on lithium ion battery technology. *ACS Cent Sci* **2017,** *3* (10), 1063-1069.

17. Miao, Y.; Hynan, P.; von Jouanne, A.; Yokochi, A., Current Li-ion battery technologies in electric vehicles and opportunities for advancements. *Energies* **2019,** *12* (6), 1074.

18. Chikkannanavar, S. B.; Bernardi, D. M.; Liu, L., A review of blended cathode materials for use in Li-ion batteries. *J Power Sources* **2014,** *248*, 91-100.

19. De las Casas, C.; Li, W., A review of application of carbon nanotubes for lithium ion battery anode material. *J Power Sources* **2012,** *208*, 74-85.

20. Xu, K., Electrolytes and interphases in Li-ion batteries and beyond. *Chem Rev* **2014,** *114* (23), 11503-11618.

21. Verma, P.; Maire, P.; Novák, P., A review of the features and analyses of the solid electrolyte interphase in Li-ion batteries. *Electrochim Acta* **2010,** *55* (22), 6332-6341.

22. Arora, P.; White, R. E.; Doyle, M., Capacity fade mechanisms and side reactions in lithium-ion batteries. *J Electrochem Soc* **1998,** *145* (10), 3647.

23. Wen, J.; Yu, Y.; Chen, C., A review on lithium-ion batteries safety issues: existing problems and possible solutions. *Mater Express* **2012,** *2* (3), 197-212.

24. Liu, K.; Liu, Y.; Lin, D.; Pei, A.; Cui, Y., Materials for lithium-ion battery safety. *Sci Adv* **2018,** *4* (6), eaas9820.

25. Ellis, B. L.; Nazar, L. F., Sodium and sodium-ion energy storage batteries. *Curr Opin Solid State Mater Sci* **2012,** *16* (4), 168-177.

26. Pan, H.; Hu, Y.-S.; Chen, L., Room-temperature stationary sodium-ion batteries for large-scale electric energy storage. *Energy Environ Sci* **2013,** *6* (8), 2338-2360.

27. Palomares, V.; Serras, P.; Villaluenga, I.; Hueso, K. B.; Carretero-González, J.; Rojo, T., Na-ion batteries, recent advances and present challenges to become low cost energy storage systems. *Energy Environ Sci* **2012,** *5* (3), 5884-5901.

28. Kong, L.; Yan, C.; Huang, J. Q.; Zhao, M. Q.; Titirici, M. M.; Xiang, R.; Zhang, Q., A review of advanced energy materials for magnesium–sulfur batteries. *Energy Environ Mater* **2018,** *1* (3), 100-112.

29. Aurbach, D.; Gofer, Y.; Lu, Z.; Schechter, A.; Chusid, O.; Gizbar, H.; Cohen, Y.; Ashkenazi, V.; Moshkovich, M.; Turgeman, R., A short review on the comparison between Li battery systems and rechargeable magnesium battery technology. *J Power Sources* **2001,** *97*, 28-32.

30. Fu, L.; Li, N.; Liu, Y.; Wang, W.; Zhu, Y.; Wu, Y., Advances of aluminum based energy storage systems. *Chin J Chem* **2017,** *35* (1), 13-20.

31. Mokhtar, M.; Talib, M. Z. M.; Majlan, E. H.; Tasirin, S. M.; Ramli, W. M. F. W.; Daud, W. R. W.; Sahari, J., Recent developments in materials for aluminum–air batteries: A review. *J Ind Eng Chem* **2015,** *32*, 1-20.

32. Eftekhari, A.; Jian, Z.; Ji, X., Potassium secondary batteries. *ACS Appl Mater Interfaces* **2017,** *9* (5), 4404-4419.

33. Hwang, J. Y.; Myung, S. T.; Sun, Y. K., Recent progress in rechargeable potassium batteries. *Adv Funct Mater* **2018,** *28* (43), 1802938.

34. Ding, J.; Zhang, H.; Fan, W.; Zhong, C.; Hu, W.; Mitlin, D., Review of Emerging Potassium–Sulfur Batteries. *Adv Mater* **2020**, 1908007.

35. Pramudita, J. C.; Sehrawat, D.; Goonetilleke, D.; Sharma, N., An initial review of the status of electrode materials for potassium-ion batteries. *Adv Energy Mater* **2017,** *7* (24), 1602911.

36. Li, Y.; Fu, J.; Zhong, C.; Wu, T.; Chen, Z.; Hu, W.; Amine, K.; Lu, J., Recent advances in flexible zinc-based rechargeable batteries. *Adv Energy Mater* **2019,** *9* (1), 1802605.

37. Li, H.; Ma, L.; Han, C.; Wang, Z.; Liu, Z.; Tang, Z.; Zhi, C., Advanced rechargeable zinc-based batteries: Recent progress and future perspectives. *Nano Energy* **2019,** *62*, 550-587.

38. Khor, A.; Leung, P.; Mohamed, M.; Flox, C.; Xu, Q.; An, L.; Wills, R.; Morante, J.; Shah, A., Review of zinc-based hybrid flow batteries: From fundamentals to applications. *Mater Today Energy* **2018,** *8*, 80-108.

39. Ponrouch, A.; Monti, D.; Boschin, A.; Steen, B.; Johansson, P.; Palacín, M. R., Non-aqueous electrolytes for sodium-ion batteries. *J Mater Chem A* **2015,** *3* (1), 22-42.

40. Hwang, J.-Y.; Myung, S.-T.; Sun, Y.-K., Sodium-ion batteries: present and future. *Chem Soc Rev* **2017,** *46* (12), 3529-3614.

41. Yadegari, H.; Sun, Q.; Sun, X., Sodium-oxygen batteries: a comparative review from chemical and electrochemical fundamentals to future perspective. *Adv Mater* **2016,** *28* (33), 7065-7093.

42. Peled, E.; Golodnitsky, D.; Mazor, H.; Goor, M.; Avshalomov, S., Parameter analysis of a practical lithium-and sodium-air electric vehicle battery. *J Power Sources* **2011,** *196* (16), 6835-6840.

43. Sun, Q.; Yang, Y.; Fu, Z.-W., Electrochemical properties of room temperature sodium–air batteries with non-aqueous electrolyte. *Electrochem Commun* **2012,** *16* (1), 22-25.

44. Kim, J.; Lim, H.-D.; Gwon, H.; Kang, K., Sodium–oxygen batteries with alkyl-carbonate and ether based electrolytes. *Phys Chem Chem Phys* **2013,** *15* (10), 3623-3629.

45. Yabuuchi, N.; Kubota, K.; Dahbi, M.; Komaba, S., Research development on sodium-ion batteries. *Chem Rev* **2014,** *114* (23), 11636-11682.

46. Seh, Z. W.; Sun, J.; Sun, Y.; Cui, Y., A highly reversible room-temperature sodium metal anode. *ACS Cent Sci* **2015,** *1* (8), 449-455.

47. Peled, E.; Golodnitsky, D.; Hadar, R.; Mazor, H.; Goor, M.; Burstein, L., Challenges and obstacles in the development of sodium–air batteries. *J Power Sources* **2013,** *244*, 771-776.

48. Wang, Z.; Selbach, S. M.; Grande, T., Van der Waals density functional study of the energetics of alkali metal intercalation in graphite. *RSC Adv* **2014,** *4* (8), 4069-4079.

49. Alcántara, R.; Jaraba, M.; Lavela, P.; Tirado, J., NiCo2O4 spinel: first report on a transition metal oxide for the negative electrode of sodium-ion batteries. *Chem Mater* **2002,** *14* (7), 2847-2848.

50. Zhou, Q.; Liu, L.; Guo, G.; Yan, Z.; Tan, J.; Huang, Z.; Chen, X.; Wang, X., Sandwich-like cobalt sulfide–graphene composite–an anode material with excellent electrochemical performance for sodium ion batteries. *RSC Adv* **2015,** *5* (88), 71644-71651.

51. Qian, J.; Xiong, Y.; Cao, Y.; Ai, X.; Yang, H., Synergistic Na-storage reactions in Sn4P3 as a high-capacity, cycle-stable anode of Na-ion batteries. *Nano letters* **2014,** *14* (4), 1865-1869.

52. Che, H.; Chen, S.; Xie, Y.; Wang, H.; Amine, K.; Liao, X.-Z.; Ma, Z.-F., Electrolyte design strategies and research progress for room-temperature sodium-ion batteries. *Energy Environ Sci* **2017,** *10* (5), 1075-1101.

53. Cresce, A. V.; Russell, S. M.; Borodin, O.; Allen, J. A.; Schroeder, M. A.; Dai, M.; Peng, J.; Gobet, M. P.; Greenbaum, S. G.; Rogers, R. E., Solvation behavior of carbonate-based electrolytes in sodium ion batteries. *Phys Chem Chem Phys* **2017,** *19* (1), 574-586.

54. Zhang, M.; Hao, H.; Zhou, D.; Duan, Y.; Wang, Y.; Bian, H., Understanding the Microscopic Structure of a "Water-in-Salt" Lithium Ion Battery Electrolyte Probed with Ultrafast IR Spectroscopy. *J Phys Chem C* **2020,** *124* (16), 8594-8604.

55. Han, J.; Zhang, H.; Varzi, A.; Passerini, S., Fluorine-free water-in-salt electrolyte for green and low-cost aqueous sodium-ion batteries. *ChemSusChem* **2018,** *11* (21), 3704-3707.

56. Lei, P.; Liu, K.; Wan, X.; Luo, D.; Xiang, X., Ultrafast Na intercalation chemistry of Na 2 Ti 3/2 Mn 1/2 (PO 4) 3 nanodots planted in a carbon matrix as a low cost anode for aqueous sodium-ion batteries. *Chem Commun* **2019,** *55* (4), 509-512.

57. Li, W.; Zhang, F.; Xiang, X.; Zhang, X., High-efficiency Na-storage performance of a nickel-based ferricyanide cathode in high-concentration electrolytes for aqueous sodium-ion batteries. *ChemElectroChem* **2017,** *4* (11), 2870-2876.

58. Kühnel, R.-S.; Reber, D.; Battaglia, C., A high-voltage aqueous electrolyte for sodium-ion batteries. *ACS Energy Lett* **2017,** *2* (9), 2005-2006.

59. Jache, B.; Adelhelm, P., Use of graphite as a highly reversible electrode with superior cycle life for sodium-ion batteries by making use of co-intercalation phenomena. *Angew Chem Int Ed* **2014,** *53* (38), 10169-10173.

60. Kim, H.; Hong, J.; Yoon, G.; Kim, H.; Park, K.-Y.; Park, M.-S.; Yoon, W.-S.; Kang, K., Sodium intercalation chemistry in graphite. *Energy Environ Sci* **2015,** *8* (10), 2963-2969.

61. Kim, H.; Hong, J.; Park, Y. U.; Kim, J.; Hwang, I.; Kang, K., Sodium Storage Behavior in Natural Graphite using Ether-based Electrolyte Systems. *Adv Funct Mater* **2015,** *25* (4), 534-541.

62. Tsuzuki, S.; Mandai, T.; Suzuki, S.; Shinoda, W.; Nakamura, T.; Morishita, T.; Ueno, K.; Seki, S.; Umebayashi, Y.; Dokko, K., Effect of the cation on the stability of cation–glyme complexes and their interactions with the [TFSA]− anion. *Phys Chem Chem Phys* **2017,** *19* (28), 18262-18272.

63. Wahlers, J.; Fulfer, K. D.; Harding, D. P.; Kuroda, D. G.; Kumar, R.; Jorn, R., Solvation structure and concentration in glyme-based sodium electrolytes: a combined spectroscopic and computational study. *J Phys Chem C* **2016,** *120* (32), 17949-17959.

64. Geysens, P.; Rangasamy, V. S.; Thayumanasundaram, S.; Robeyns, K.; Van Meervelt, L.; Locquet, J.-P.; Fransaer, J.; Binnemans, K., Solvation Structure of Sodium Bis(fluorosulfonyl)imide-Glyme Solvate Ionic Liquids and Its Influence on Cycling of Na-MNC Cathodes. *J Phys Chem B* **2018,** *122* (1), 275-289.

65. Li, K.; Galle Kankanamge, S. R.; Weldeghiorghis, T. K.; Jorn, R.; Kuroda, D. G.; Kumar, R., Predicting Ion Association in Sodium Electrolytes: A Transferrable Model for Investigating Glymes. *J Phys Chem C* **2017,** *122* (9), 4747-4756.

66. Galle Kankanamge, S. R.; Li, K.; Fulfer, K. D.; Du, P.; Jorn, R.; Kumar, R.; Kuroda, D. G., Mechanism behind the Unusually High Conductivities of High Concentrated Sodium Ion Glyme-Based Electrolytes. *J Phys Chem C* **2018,** *122* (44), 25237-25246.

67. Jache, B.; Binder, J. O.; Abe, T.; Adelhelm, P., A comparative study on the impact of different glymes and their derivatives as electrolyte solvents for graphite co-intercalation electrodes in lithium-ion and sodium-ion batteries. *Phys Chem Chem Phys* **2016,** *18* (21), 14299-14316.

68. Cheng, X.-B.; Zhang, R.; Zhao, C.-Z.; Zhang, Q., Toward safe lithium metal anode in rechargeable batteries: a review. *Chem Rev* **2017,** *117* (15), 10403-10473.

69. Takehara, Z.-i., Future prospects of the lithium metal anode. *J Power Sources* **1997,** *68* (1), 82-86.

70. Park, M. S.; Ma, S. B.; Lee, D. J.; Im, D.; Doo, S.-G.; Yamamoto, O., A highly reversible lithium metal anode. *Sci Rep* **2014,** *4*, 3815.

71. Kozen, A. C.; Lin, C.-F.; Pearse, A. J.; Schroeder, M. A.; Han, X.; Hu, L.; Lee, S.-B.; Rubloff, G. W.; Noked, M., Next-generation lithium metal anode engineering via atomic layer deposition. *ACS Nano* **2015,** *9* (6), 5884-5892.

72. Yan, C.; Cheng, X. B.; Tian, Y.; Chen, X.; Zhang, X. Q.; Li, W. J.; Huang, J. Q.; Zhang, Q., Dual-layered film protected lithium metal anode to enable dendrite-free lithium deposition. *Adv Mater* **2018,** *30* (25), 1707629.

73. Qian, J.; Henderson, W. A.; Xu, W.; Bhattacharya, P.; Engelhard, M.; Borodin, O.; Zhang, J.-G., High rate and stable cycling of lithium metal anode. *Nat Commun* **2015,** *6* (1), 1-9.

74. Lin, D.; Liu, Y.; Cui, Y., Reviving the lithium metal anode for high-energy batteries. *Nat Nanotechnol* **2017,** *12* (3), 194.

75. Zhu, B.; Wang, X.; Yao, P.; Li, J.; Zhu, J., Towards high energy density lithium battery anodes: silicon and lithium. *Chem Sci* **2019,** *10* (30), 7132-7148.

76. Lee, J. H.; Yoon, C. S.; Hwang, J.-Y.; Kim, S.-J.; Maglia, F.; Lamp, P.; Myung, S.-T.; Sun, Y.-K., High-energy-density lithium-ion battery using a carbon-nanotube–Si composite anode and a compositionally graded Li [Ni 0.85 Co 0.05 Mn 0.10] O 2 cathode. *Energy Environ Sci* **2016,** *9* (6), 2152-2158.

77. Lv, X.; Wei, W.; Huang, B.; Dai, Y., Achieving high energy density for lithium-ion battery anodes by Si/C nanostructure design. *J Mater Chem A* **2019,** *7* (5), 2165-2171.

78. Kim, N.; Chae, S.; Ma, J.; Ko, M.; Cho, J., Fast-charging high-energy lithium-ion batteries via implantation of amorphous silicon nanolayer in edge-plane activated graphite anodes. *Nat Commun* **2017,** *8* (1), 1-10.

79. Li, J.-Y.; Xu, Q.; Li, G.; Yin, Y.-X.; Wan, L.-J.; Guo, Y.-G., Research progress regarding Si-based anode materials towards practical application in high energy density Li-ion batteries. *Mater Chem Front* **2017,** *1* (9), 1691-1708.

80. Wang, C.; Wu, L.; Wang, H.; Zuo, W.; Li, Y.; Liu, J., Fabrication and shell optimization of synergistic TiO2-MoO3 core–shell nanowire array anode for high energy and power density lithium-ion batteries. *Adv Funct Mater* **2015,** *25* (23), 3524-3533.

81. Sen, U. K.; Mitra, S., High-rate and high-energy-density lithium-ion battery anode containing 2D MoS2 nanowall and cellulose binder. *ACS Appl Mater Interfaces* **2013,** *5* (4), 1240-1247.

82. Park, M.-G.; Lee, D.-H.; Jung, H.; Choi, J.-H.; Park, C.-M., Sn-based nanocomposite for Li-ion battery anode with high energy density, rate capability, and reversibility. *ACS Nano* **2018,** *12* (3), 2955-2967.

83. Casimir, A.; Zhang, H.; Ogoke, O.; Amine, J. C.; Lu, J.; Wu, G., Silicon-based anodes for lithium-ion batteries: Effectiveness of materials synthesis and electrode preparation. *Nano Energy* **2016,** *27*, 359-376.

84. Vrankovic, D.; Graczyk-Zajac, M.; Kalcher, C.; Rohrer, J.; Becker, M.; Stabler, C.; Trykowski, G.; Albe, K.; Riedel, R., Highly porous silicon embedded in a ceramic matrix: a stable high-capacity electrode for Li-ion batteries. *ACS Nano* **2017,** *11* (11), 11409-11416.

85. Jia, H.; Zheng, J.; Song, J.; Luo, L.; Yi, R.; Estevez, L.; Zhao, W.; Patel, R.; Li, X.; Zhang, J.-G., A novel approach to synthesize micrometer-sized porous silicon as a high performance anode for lithium-ion batteries. *Nano Energy* **2018,** *50*, 589-597.

86. Liu, Y.; Tai, Z.; Zhou, T.; Sencadas, V.; Zhang, J.; Zhang, L.; Konstantinov, K.; Guo, Z.; Liu, H. K., An All-Integrated Anode via Interlinked Chemical Bonding between Double-Shelled–Yolk-Structured Silicon and Binder for Lithium-Ion Batteries. *Adv Mater* **2017,** *29* (44), 1703028.

87. Wu, H.; Zheng, G.; Liu, N.; Carney, T. J.; Yang, Y.; Cui, Y., Engineering empty space between Si nanoparticles for lithium-ion battery anodes. *Nano letters* **2012,** *12* (2), 904-909.

88. Xie, J.; Wang, J.; Lee, H. R.; Yan, K.; Li, Y.; Shi, F.; Huang, W.; Pei, A.; Chen, G.; Subbaraman, R., Engineering stable interfaces for three-dimensional lithium metal anodes. *Sci Adv* **2018,** *4* (7), eaat5168.

89. Xie, J.; Liao, L.; Gong, Y.; Li, Y.; Shi, F.; Pei, A.; Sun, J.; Zhang, R.; Kong, B.; Subbaraman, R., Stitching h-BN by atomic layer deposition of LiF as a stable interface for lithium metal anode. *Sci Adv* **2017,** *3* (11), eaao3170.

90. Li, N. W.; Yin, Y. X.; Yang, C. P.; Guo, Y. G., An artificial solid electrolyte interphase layer for stable lithium metal anodes. *Adv Mater* **2016,** *28* (9), 1853-1858.

91. Xu, R.; Zhang, X. Q.; Cheng, X. B.; Peng, H. J.; Zhao, C. Z.; Yan, C.; Huang, J. Q., Artificial soft–rigid protective layer for dendrite-free lithium metal anode. *Adv Funct Mater* **2018,** *28* (8), 1705838.

92. Cha, E.; Patel, M. D.; Park, J.; Hwang, J.; Prasad, V.; Cho, K.; Choi, W., 2D MoS 2 as an efficient protective layer for lithium metal anodes in high-performance Li–S batteries. *Nat Nanotechnol* **2018,** *13* (4), 337-344.

93. Liang, X.; Pang, Q.; Kochetkov, I. R.; Sempere, M. S.; Huang, H.; Sun, X.; Nazar, L. F., A facile surface chemistry route to a stabilized lithium metal anode. *Nat Energy* **2017,** *2* (9), 17119.

94. Henderson, W. A., Glyme− lithium salt phase behavior. *J Phys Chem B* **2006,** *110* (26), 13177-13183.

95. Henderson, W. A.; McKenna, F.; Khan, M. A.; Brooks, N. R.; Young Jr, V. G.; Frech, R., Glyme− lithium bis (trifluoromethanesulfonyl) imide and glyme− lithium Bis (perfluoroethanesulfonyl) imide phase behavior and solvate structures. *Chem Mater* **2005,** *17* (9), 2284-2289.

96. Jeong, S.-K.; Seo, H.-Y.; Kim, D.-H.; Han, H.-K.; Kim, J.-G.; Lee, Y. B.; Iriyama, Y.; Abe, T.; Ogumi, Z., Suppression of dendritic lithium formation by using concentrated electrolyte solutions. *Electrochem Commun* **2008,** *10* (4), 635-638.

97. Suo, L.; Borodin, O.; Gao, T.; Olguin, M.; Ho, J.; Fan, X.; Luo, C.; Wang, C.; Xu, K., "Water-in-salt" electrolyte enables high-voltage aqueous lithium-ion chemistries. *Science* **2015,** *350* (6263), 938-943.

98. Yamada, Y.; Furukawa, K.; Sodeyama, K.; Kikuchi, K.; Yaegashi, M.; Tateyama, Y.; Yamada, A., Unusual stability of acetonitrile-based superconcentrated electrolytes for fast-charging lithium-ion batteries. *J Am Chem Soc* **2014,** *136* (13), 5039-5046.

99. Wang, J.; Yamada, Y.; Sodeyama, K.; Chiang, C. H.; Tateyama, Y.; Yamada, A., Superconcentrated electrolytes for a high-voltage lithium-ion battery. *Nat Commun* **2016,** *7* (1), 1-9.

100. Dokko, K.; Watanabe, D.; Ugata, Y.; Thomas, M. L.; Tsuzuki, S.; Shinoda, W.; Hashimoto, K.; Ueno, K.; Umebayashi, Y.; Watanabe, M., Direct evidence for Li ion hopping conduction in highly concentrated sulfolane-based liquid electrolytes. *J Phys Chem B* **2018,** *122* (47), 10736-10745.

101. Kondou, S.; Thomas, M. L.; Mandai, T.; Ueno, K.; Dokko, K.; Watanabe, M., Ionic transport in highly concentrated lithium bis (fluorosulfonyl) amide electrolytes with keto ester solvents: structural implications for ion hopping conduction in liquid electrolytes. *Phys Chem Chem Phys* **2019,** *21* (9), 5097-5105.

102. Nakanishi, A.; Ueno, K.; Watanabe, D.; Ugata, Y.; Matsumae, Y.; Liu, J.; Thomas, M. L.; Dokko, K.; Watanabe, M., Sulfolane-based highly concentrated electrolytes of lithium bis (trifluoromethanesulfonyl) amide: ionic transport, Li-Ion coordination, and Li–S battery performance. *J Phys Chem C* **2019,** *123* (23), 14229-14238.

103. Ugata, Y.; Thomas, M. L.; Mandai, T.; Ueno, K.; Dokko, K.; Watanabe, M., Li-ion hopping conduction in highly concentrated lithium bis(fluorosulfonyl)amide/dinitrile liquid electrolytes. *Phys Chem Chem Phys* **2019,** *21* (19), 9759-9768.

104. Dong, X.; Lin, Y.; Li, P.; Ma, Y.; Huang, J.; Bin, D.; Wang, Y.; Qi, Y.; Xia, Y., High-energy rechargeable metallic lithium battery at− 70 C enabled by a cosolvent electrolyte. *Angew Chem Int Ed* **2019,** *131* (17), 5679-5683.

105. Seo, D. M.; Afroz, T.; Allen, J. L.; Boyle, P. D.; Trulove, P. C.; De Long, H. C.; Henderson, W. A., Structural interactions within lithium salt solvates: Cyclic carbonates and esters. *J Phys Chem C* **2014,** *118* (45), 25884-25889.

106. Afroz, T.; Seo, D. M.; Han, S.-D.; Boyle, P. D.; Henderson, W. A., Structural Interactions within Lithium Salt Solvates: Acyclic Carbonates and Esters. *J Phys Chem C* **2015,** *119* (13), 7022-7027.

107. Seo, D. M.; Boyle, P. D.; Sommer, R. D.; Daubert, J. S.; Borodin, O.; Henderson, W. A., Solvate structures and spectroscopic characterization of LiTFSI electrolytes. *J Phys Chem B* **2014,** *118* (47), 13601-13608.

108. Han, S.-D.; Yun, S.-H.; Borodin, O.; Seo, D. M.; Sommer, R. D.; Young Jr, V. G.; Henderson, W. A., Solvate Structures and Computational/Spectroscopic Characterization of LiPF6 Electrolytes. *J Phys Chem C* **2015,** *119* (16), 8492-8500.

109. Han, S.-D.; Allen, J. L.; Jónsson, E.; Johansson, P.; McOwen, D. W.; Boyle, P. D.; Henderson, W. A., Solvate structures and computational/spectroscopic characterization of lithium difluoro (oxalato) borate (LiDFOB) electrolytes. *J Phys Chem C* **2013,** *117* (11), 5521-5531.

110. Henderson, W. A.; Brooks, N. R.; Brennessel, W. W.; Young, V. G., LiClO4 electrolyte solvate structures. *J Phys Chem A* **2004,** *108* (1), 225-229.

111. Ueno, K.; Yoshida, K.; Tsuchiya, M.; Tachikawa, N.; Dokko, K.; Watanabe, M., Glyme-Lithium Salt Equimolar Molten Mixtures: Concentrated Solutions or Solvate Ionic Liquids? *J Phys Chem B* **2012,** *116* (36), 11323-11331.

112. Ueno, K.; Tatara, R.; Tsuzuki, S.; Saito, S.; Doi, H.; Yoshida, K.; Mandai, T.; Matsugami, M.; Umebayashi, Y.; Dokko, K., Li+ solvation in glyme-Li salt solvate ionic liquids. *Phys Chem Chem Phys* **2015,** *17* (12), 8248-8257.

113. Lee, K.-K.; Park, K.; Lee, H.; Noh, Y.; Kossowska, D.; Kwak, K.; Cho, M., Ultrafast fluxional exchange dynamics in electrolyte solvation sheath of lithium ion battery. *Nat Commun* **2017,** *8* (1), 1-9.

114. Liang, C.; Kwak, K.; Cho, M., Revealing the solvation structure and dynamics of carbonate electrolytes in lithium-ion batteries by two-dimensional infrared spectrum modeling. *J Phys Chem Lett* **2017,** *8* (23), 5779-5784.

115. Fulfer, K. D.; Kuroda, D. G., Ion speciation of lithium hexafluorophosphate in dimethyl carbonate solutions: an infrared spectroscopy study. *Phys Chem Chem Phys* **2018,** *20* (35), 22710-22718.

116. Fulfer, K. D.; Kuroda, D. G., Solvation structure and dynamics of the lithium ion in organic carbonate-based electrolytes: A time-dependent infrared spectroscopy study. *J Phys Chem C* **2016,** *120* (42), 24011-24022.

117. Fulfer, K. D.; Kuroda, D. G., A comparison of the solvation structure and dynamics of the lithium ion in linear organic carbonates with different alkyl chain lengths. *Phys Chem Chem Phys* **2017,** *19* (36), 25140-25150.

118. Klassen, B.; Aroca, R.; Nazri, M.; Nazri, G., Raman spectra and transport properties of lithium perchlorate in ethylene carbonate based binary solvent systems for lithium batteries. *J Phys Chem B* **1998,** *102* (24), 4795-4801.

119. Maeda, S.; Kameda, Y.; Amo, Y.; Usuki, T.; Ikeda, K.; Otomo, T.; Yanagisawa, M.; Seki, S.; Arai, N.; Watanabe, H., Local Structure of Li+ in Concentrated Ethylene Carbonate Solutions Studied by Low-Frequency Raman Scattering and Neutron Diffraction with Li-6/Li-7 Isotopic Substitution Methods. *J Phys Chem B* **2017,** *121* (48), 10979-10987.

120. Aroca, R.; Nazri, R.; Nazri, G. A.; Camargo, A. J.; Trsic, M., Vibrational spectra and ion-pair properties of lithium hexafluorophosphate in ethylene carbonate based mixed-solvent systems for lithium batteries. *J Solution Chem* **2000,** *29* (10), 1047-1060.

121. Giorgini, M. G.; Futamatagawa, K.; Torii, H.; Musso, M.; Cerini, S., Solvation structure around the Li+ ion in mixed cyclic/linear carbonate solutions unveiled by the Raman noncoincidence effect. *J Phys Chem Lett* **2015,** *6* (16), 3296-3302.

122. Burba, C. M.; Frech, R., Spectroscopic measurements of ionic association in solutions of LiPF6. *J Phys Chem B* **2005,** *109* (31), 15161-15164.

123. Kondo, K.; Sano, M.; Hiwara, A.; Omi, T.; Fujita, M.; Kuwae, A.; Iida, M.; Mogi, K.; Yokoyama, H., Conductivity and solvation of Li+ ions of LiPF6 in propylene carbonate solutions. *J Phys Chem B* **2000,** *104* (20), 5040-5044.

124. Cazzanelli, E.; Mustarelli, P.; Benevelli, F.; Appetecchi, G. B.; Croce, F., Raman and NMR analysis of LiClO4 concentrated solutions in ethylene carbonate-propylene carbonate. *Solid State Ionics* **1996,** *86*, 379-384.

125. Matsubara, K.; Kaneuchi, R.; Maekita, N., 13 C NMR estimation of preferential solvation of lithium ions in non-aqueous mixed solvents. *J Chem Soc, Faraday Trans* **1998,** *94* (24), 3601-3605.

126. Bogle, X.; Vazquez, R.; Greenbaum, S.; Cresce, A. v. W.; Xu, K., Understanding Li+-Solvent Interaction in Nonaqueous Carbonate Electrolytes with O-17 NMR. *J Phys Chem Lett* **2013,** *4* (10), 1664-1668.

127. Yang, L.; Xiao, A.; Lucht, B. L., Investigation of solvation in lithium ion battery electrolytes by NMR spectroscopy. *J Mol Liq* **2010,** *154* (2-3), 131-133.

128. Fukushima, T.; Matsuda, Y.; Hashimoto, H.; Arakawa, R., Studies on solvation of lithium ions in organic electrolyte solutions by electrospray ionization-mass spectroscopy. *Electrochem Solid-State Lett* **2001,** *4* (8), A127.

129. Matsuda, Y.; Fukushima, T.; Hashimoto, H.; Arakawa, R., Solvation of lithium ions in mixed organic electrolyte solutions by electrospray ionization mass spectroscopy. *J Electrochem Soc* **2002,** *149* (8), A1045.

130. Lewis, N. H.; Zhang, Y.; Dereka, B.; Carino, E. V.; Maginn, E. J.; Tokmakoff, A., Signatures of Ion Pairing and Aggregation in the Vibrational Spectroscopy of Super-Concentrated Aqueous Lithium Bistriflimide Solutions. *J Phys Chem C* **2020,** *124* (6), 3470-3481.

131. Soetens, J.-C.; Millot, C.; Maigret, B.; Bakó, I., Molecular dynamics simulation and X—ray diffraction studies of ethylene carbonate, propylene carbonate and dimethyl carbonate in liquid phase. *J Mol Liq* **2001,** *92* (3), 201-216.

132. Rushing, J. C.; Leonik, F. M.; Kuroda, D. G., Effect of solvation shell structure and composition on ion pair formation: The case study of litdi in organic carbonates. *J Phys Chem C* **2019,** *123* (41), 25102-25112.

133. Lim, J.; Lee, K.-K.; Liang, C.; Park, K.-H.; Kim, M.; Kwak, K.; Cho, M., Two-dimensional infrared spectroscopy and molecular dynamics simulation studies of nonaqueous lithium ion battery electrolytes. *J Phys Chem B* **2019,** *123* (31), 6651-6663.

134. Osawa, K.; Kossowska, D.; Park, K.; Kwak, K.; Cho, M., Two-dimensional infrared spectroscopic study of cytochrome c peroxidase activity in deep eutectic solvent. *Struct Dyn* **2019,** *6* (6), 064703.

135. Cui, Y.; Fulfer, K. D.; Ma, J.; Weldeghiorghis, T. K.; Kuroda, D. G., Solvation dynamics of an ionic probe in choline chloride-based deep eutectic solvents. *Phys Chem Chem Phys* **2016,** *18* (46), 31471-31479.

136. Cui, Y.; Rushing, J. C.; Seifert, S.; Bedford, N. M.; Kuroda, D. G., Molecularly heterogeneous structure of a nonionic deep eutectic solvent composed of n-methylacetamide and lauric acid. *J Phys Chem B* **2019,** *123* (18), 3984-3993.

137. Cui, Y.; Kuroda, D. G., Evidence of molecular heterogeneities in amide-based deep eutectic solvents. *J Phys Chem A* **2018,** *122* (5), 1185-1193.

138. Tamimi, A.; Fayer, M. D., Ionic liquid dynamics measured with 2D IR and IR pump–probe experiments on a linear anion and the influence of potassium cations. *J Phys Chem B* **2016,** *120* (26), 5842-5854.

139. Shin, J. Y.; Yamada, S. A.; Fayer, M. D., Dynamics of a Room Temperature Ionic Liquid in Supported Ionic Liquid Membranes vs the Bulk Liquid: 2D IR and Polarized IR Pump-Probe Experiments. *J Am Chem Soc* **2017,** *139* (1), 311-323.

140. Ren, Z.; Brinzer, T.; Dutta, S.; Garrett-Roe, S., Thiocyanate as a Local Probe of Ultrafast Structure and Dynamics in Imidazolium-Based Ionic Liquids: Water-Induced Heterogeneity and Cation-Induced Ion Pairing. *J Phys Chem B* **2015,** *119* (13), 4699-4712.

141. Tamimi, A.; Bailey, H. E.; Fayer, M. D., Alkyl chain length dependence of the dynamics and structure in the ionic regions of room-temperature ionic liquids. *J Phys Chem B* **2016,** *120* (30), 7488-7501.

142. Asbury, J. B.; Steinel, T.; Fayer, M., Using ultrafast infrared multidimensional correlation spectroscopy to aid in vibrational spectral peak assignments. *Chem Phys Lett* **2003,** *381* (1-2), 139-146.

143. Rector, K.; Rella, C.; Hill, J. R.; Kwok, A.; Sligar, S. G.; Chien, E. Y.; Dlott, D. D.; Fayer, M., Mutant and wild-type myoglobin-CO protein dynamics: vibrational echo experiments. *J Phys Chem B* **1997,** *101* (8), 1468-1475.

144. Zanni, M. T.; Hochstrasser, R. M., Two-dimensional infrared spectroscopy: a promising new method for the time resolution of structures. *Curr Opin Struct Biol* **2001,** *11* (5), 516-522.

145. Hamm, P.; Zanni, M., *Concepts and methods of 2D infrared spectroscopy*. Cambridge University Press: 2011.

146. Griffiths, D. J., Introduction to electrodynamics. American Association of Physics Teachers: 2005.

147. Jackson, J. D., Classical electrodynamics. American Association of Physics Teachers: 1999.

148. Kubo, R., *A stochastic theory of line shape*. 1969; Vol. 15, p 101-127.

149. Fenn, E. E.; Fayer, M., Extracting 2D IR frequency-frequency correlation functions from two component systems. *J Chem Phys* **2011,** *135* (7), 074502.

150. Kwac, K.; Cho, M., Molecular dynamics simulation study of N-methylacetamide in water. II. Two-dimensional infrared pump–probe spectra. *J Chem Phys* **2003,** *119* (4), 2256-2263.

151. Abramczyk, H., *Introduction to laser spectroscopy*. Elsevier: 2005.

152. Hamm, P.; Kaindl, R. A.; Stenger, J., Noise suppression in femtosecond mid-infrared light sources. *Opt Lett* **2000,** *25* (24), 1798-1800.

153. Trebino, R.; DeLong, K. W.; Fittinghoff, D. N.; Sweetser, J. N.; Krumbügel, M. A.; Richman, B. A.; Kane, D. J., Measuring ultrashort laser pulses in the time-frequency domain using frequency-resolved optical gating. *Rev Sci Instrum* **1997,** *68* (9), 3277-3295.

154. Khalil, M.; Demirdöven, N.; Tokmakoff, A., Obtaining absorptive line shapes in two-dimensional infrared vibrational correlation spectra. *Phys Rev Lett* **2003,** *90* (4), 047401.

155. Xie, L.; Ilic, M. D. In *Model predictive dispatch in electric energy systems with intermittent resources*, 2008 IEEE International Conference on Systems, Man and Cybernetics, 12-15 Oct. 2008; 2008; pp 42-47.

156. Kim, T. H.; Park, J. S.; Chang, S. K.; Choi, S.; Ryu, J. H.; Song, H. K., The Current Move of Lithium Ion Batteries Towards the Next Phase. *Adv Energy Mater* **2012,** *2* (7), 860-872.

157. Zhang, S. S., A review on electrolyte additives for lithium-ion batteries. *J Power Sources* **2006,** *162* (2), 1379-1394.

158. Goodenough, J. B.; Park, K. S., The Li-ion rechargeable battery: a perspective. *J Am Chem Soc* **2013,** *135* (4), 1167-76.

159. Dunn, B.; Kamath, H.; Tarascon, J. M., Electrical Energy Storage for the Grid: A Battery of Choices. *Science* **2011,** *334* (6058), 928-935.

160. Slater, M. D.; Kim, D.; Lee, E.; Johnson, C. S., Sodium-Ion Batteries. *Adv Funct Mater* **2013,** *23* (8), 947-958.

161. Alcantara, R.; Mateos, J. M. J.; Tirado, J. L., Negative electrodes for lithium- and sodium-ion batteries obtained by heat-treatment of petroleum cokes below 1000 degrees C. *J Electrochem Soc* **2002,** *149* (2), A201-A205.

162. Komaba, S.; Murata, W.; Ishikawa, T.; Yabuuchi, N.; Ozeki, T.; Nakayama, T.; Ogata, A.; Gotoh, K.; Fujiwara, K., Electrochemical Na Insertion and Solid Electrolyte Interphase for Hard-Carbon Electrodes and Application to Na-Ion Batteries. *Adv Funct Mater* **2011,** *21* (20), 3859-3867.

163. Kubota, K.; Komaba, S., Review-Practical Issues and Future Perspective for Na-Ion Batteries. *J Electrochem Soc* **2015,** *162* (14), A2538-A2550.

164. Divincenzo, D. P.; Mele, E. J., Cohesion and Structure in Stage-1 Graphite-Intercalation Compounds. *Phys Rev B* **1985,** *32* (4), 2538-2553.

165. Pascal, G. E.; Fouletier, M., Electrochemical Intercalation of Sodium in Graphite. *Solid State Ionics* **1988,** *28*, 1172-1175.

166. Ong, S. P.; Chevrier, V. L.; Hautier, G.; Jain, A.; Moore, C.; Kim, S.; Ma, X. H.; Ceder, G., Voltage, stability and diffusion barrier differences between sodium-ion and lithium-ion intercalation materials. *Energy Environ Sci* **2011,** *4* (9), 3680-3688.

167. Stevens, D. A.; Dahn, J. R., The mechanisms of lithium and sodium insertion in carbon materials. *J Electrochem Soc* **2001,** *148* (8), A803-A811.

168. Jache, B.; Adelhelm, P., Use of graphite as a highly reversible electrode with superior cycle life for sodium-ion batteries by making use of co-intercalation phenomena. *Angew Chem Int Ed* **2014,** *53* (38), 10169-73.

169. Monti, D.; Jonsson, E.; Palacin, M. R.; Johansson, P., Ionic liquid based electrolytes for sodium-ion batteries: Na+ solvation and ionic conductivity. *J Power Sources* **2014,** *245*, 630-636.

170. Lim, Y. R.; Shojaei, F.; Park, K.; Jung, C. S.; Park, J.; Cho, W. I.; Kang, H. S., Arsenic for high-capacity lithium- and sodium-ion batteries. *Nanoscale* **2018,** *10* (15), 7047-7057.

171. Carbone, L.; Munoz, S.; Gobet, M.; Devany, M.; Greenbaum, S.; Hassoun, J., Characteristics of glyme electrolytes for sodium battery: nuclear magnetic resonance and electrochemical study. *Electrochim Acta* **2017,** *231* (Supplement C), 223-229.

172. Okoshi, M.; Chou, C. P.; Nakai, H., Theoretical Analysis of Carrier Ion Diffusion in Superconcentrated Electrolyte Solutions for Sodium-Ion Batteries. *J Phys Chem B* **2018,** *122* (9), 2600-2609.

173. Westman, K.; Dugas, R.; Jankowski, P.; Wieczorek, W.; Gachot, G.; Morcrette, M.; Irisarri, E.; Ponrouch, A.; Palacín, M. R.; Tarascon, J. M.; Johansson, P., Diglyme Based Electrolytes for Sodium-Ion Batteries. *ACS Applied Energy Materials* **2018,** *1* (6), 2671-2680.

174. Ren, Z.; Ivanova, A. S.; Couchot-Vore, D.; Garrett-Roe, S., Ultrafast Structure and Dynamics in Ionic Liquids: 2D-IR Spectroscopy Probes the Molecular Origin of Viscosity. *Journal of Physical Chemistry Letters* **2014,** *5* (9), 1541-6.

175. Kim, Y. S.; Wang, J. P.; Hochstrasser, R. M., Two-dimensional infrared spectroscopy of the alanine dipeptide in aqueous solution. *J Phys Chem B* **2005,** *109* (15), 7511-21.

176. Frisch, M. J.; Trucks, G. W.; Schlegel, H. B.; Scuseria, G. E.; Robb, M. A.; Cheeseman, J. R.; Scalmani, G.; Barone, V.; Petersson, G. A.; Nakatsuji, H.; Li, X.; Caricato, M.; Marenich, A. V.; Bloino, J.; Janesko, B. G.; Gomperts, R.; Mennucci, B.; Hratchian, H. P.; Ortiz, J. V.; Izmaylov, A. F.; Sonnenberg, J. L.; Williams; Ding, F.; Lipparini, F.; Egidi, F.; Goings, J.; Peng, B.; Petrone, A.; Henderson, T.; Ranasinghe, D.; Zakrzewski, V. G.; Gao, J.; Rega, N.; Zheng, G.; Liang, W.; Hada, M.; Ehara, M.; Toyota, K.; Fukuda, R.; Hasegawa, J.; Ishida, M.; Nakajima, T.; Honda, Y.; Kitao, O.; Nakai, H.; Vreven, T.; Throssell, K.; Montgomery Jr., J. A.; Peralta, J. E.; Ogliaro, F.; Bearpark, M. J.; Heyd, J. J.; Brothers, E. N.; Kudin, K. N.; Staroverov, V. N.; Keith, T. A.; Kobayashi, R.; Normand, J.; Raghavachari, K.; Rendell, A. P.; Burant, J. C.; Iyengar, S. S.; Tomasi, J.; Cossi, M.; Millam, J. M.; Klene, M.; Adamo, C.; Cammi, R.; Ochterski, J. W.; Martin, R. L.; Morokuma, K.; Farkas, O.; Foresman, J. B.; Fox, D. J. *Gaussian 16*, Wallingford, CT, 2016.

177. Martinez, M. C.; Garcia de la Torre, J., Brownian dynamics simulation of restricted rotational diffusion. *Biophys J* **1987,** *52* (2), 303-10.

178. Choi, J. H.; Oh, K. I.; Lee, H.; Lee, C.; Cho, M., Nitrile and thiocyanate IR probes: quantum chemistry calculation studies and multivariate least-square fitting analysis. *J Chem Phys* **2008,** *128* (13), 134506.

179. Park, S.; Park, J.; Lin, H. W.; Lim, M., Vibrational Relaxation of Cyanate or Thiocyanate Bound to Ferric Heme Proteins Studied by Femtosecond Infrared Spectroscopy. *B Korean Chem Soc* **2014,** *35* (3), 758-764.

180. Ohta, K.; Tominaga, K., Vibrational population relaxation of thiocyanate ion in polar solvents studied by ultrafast infrared spectroscopy. *Chem Phys Lett* **2006,** *429* (1-3), 136-140.

181. Ji, M. B.; Park, S.; Gaffney, K. J., Dynamics of Ion Assembly in Solution: 2DIR Spectroscopy Study of LiNCS in Benzonitrile. *J Phys Chem Lett* **2010,** *1* (12), 1771-1775.

182. Kuroda, D. G.; Hochstrasser, R. M., Dynamic structures of aqueous oxalate and the effects of counterions seen by 2D IR. *Phys Chem Chem Phys* **2012,** *14* (18), 6219-24.

183. Park, K. H.; Choi, S. R.; Choi, J. H.; Park, S.; Cho, M., Real-Time Probing of Ion Pairing Dynamics with 2DIR Spectroscopy. *Chemphyschem* **2010,** *11* (17), 3632-3637.

184. Hojo, M.; Miyauchi, Y.; Tanio, A.; Imai, Y., Specific Interactions between Anions and Cations in Protophobic Aprotic-Solvents - Triple-Ion and Higher Aggregate Formation from Lithium and Tributylammonium Thiocyanates. *J Chem Soc Faraday T* **1991,** *87* (24), 3847-3852.

185. Kwak, K.; Park, S.; Finkelstein, I. J.; Fayer, M. D., Frequency-frequency correlation functions and apodization in two-dimensional infrared vibrational echo spectroscopy: a new approach. *J Chem Phys* **2007,** *127* (12), 124503.

186. Giammanco, C. H.; Kramer, P. L.; Yamada, S. A.; Nishida, J.; Tamimi, A.; Fayer, M. D., Carbon dioxide in an ionic liquid: Structural and rotational dynamics. *J Chem Phys* **2016,** *144* (10), 104506.

187. Lipari, G.; Szabo, A., Effect of Librational Motion on Fluorescence Depolarization and Nuclear Magnetic-Resonance Relaxation in Macromolecules and Membranes. *Biophys J* **1980,** *30* (3), 489-506.

188. Moog, R. S.; Ediger, M. D.; Boxer, S. G.; Fayer, M. D., Viscosity dependence of the rotational reorientation of rhodamine B in mono- and polyalcohols. Picosecond transient grating experiments. *Journal of Physical Chemistry* **1982,** *86* (24), 4694-4700.

189. Kramer, P. L.; Nishida, J.; Fayer, M. D., Separation of experimental 2D IR frequency-frequency correlation functions into structural and reorientation-induced contributions. *Journal of Chemical Physics* **2015,** *143* (12), 124505.

190. Amine, K.; Kanno, R.; Tzeng, Y. H., Rechargeable lithium batteries and beyond: Progress, Challenges, and future directions. *Mrs Bull* **2014,** *39* (5), 395-405.

191. Goodenough, J. B.; Kim, Y., Challenges for Rechargeable Li Batteries. *Chem Mater* **2010,** *22* (3), 587-603.

192. Johnson, L.; Li, C. M.; Liu, Z.; Chen, Y. H.; Freunberger, S. A.; Ashok, P. C.; Praveen, B. B.; Dholakia, K.; Tarascon, J. M.; Bruce, P. G., The role of LiO2 solubility in O-2 reduction in aprotic solvents and its consequences for Li-O-2 batteries. *Nat Chem* **2014,** *6* (12), 1091-1099.

193. Gauthier, M.; Carney, T. J.; Grimaud, A.; Giordano, L.; Pour, N.; Chang, H. H.; Fenning, D. P.; Lux, S. F.; Paschos, O.; Bauer, C.; Magia, F.; Lupart, S.; Lamp, P.; Shao-Horn, Y., Electrode-Electrolyte Interface in Li-Ion Batteries: Current Understanding and New Insights. *J Phys Chem Lett* **2015,** *6* (22), 4653-4672.

194. Nitta, N.; Wu, F. X.; Lee, J. T.; Yushin, G., Li-ion battery materials: present and future. *Mater Today* **2015,** *18* (5), 252-264.

195. Wang, J.; Yamada, Y.; Sodeyama, K.; Chiang, C. H.; Tateyama, Y.; Yamada, A., Superconcentrated electrolytes for a high-voltage lithium-ion battery. *Nat Commun* **2016,** *7*.

196. Yamada, Y.; Yaegashi, M.; Abe, T.; Yamada, A., A superconcentrated ether electrolyte for fast-charging Li-ion batteries. *Chem Commun* **2013,** *49* (95), 11194-11196.

197. Suo, L. M.; Hu, Y. S.; Li, H.; Armand, M.; Chen, L. Q., A new class of Solvent-in-Salt electrolyte for high-energy rechargeable metallic lithium batteries. *Nat Commun* **2013,** *4*.

198. Liang, H. Y.; Li, H.; Wang, Z. X.; Wu, F.; Chen, L. Q.; Huang, X. J., New binary room-temperature molten salt electrolyte based on urea and LiTFSI. *J Phys Chem B* **2001,** *105* (41), 9966-9969.

199. Chen, R. J.; Wu, F.; Li, L.; Qiu, X.; Chen, L. Q.; Chen, S., The structure-activity relationship studies of binary room temperature complex electrolytes based on LiTFSI and organic compounds with acylamino group. *Vib Spectrosc* **2007,** *44* (2), 297-307.

200. Ma, Q.; Qi, X. G.; Tong, B.; Zheng, Y. H.; Feng, W. F.; Nie, J.; Hu, Y. S.; Li, H.; Huang, X. J.; Chen, L. Q.; Zhou, Z. B., Novel Li[(CF3SO2)(n-C4F9SO2)N]-Based Polymer Electrolytes for Solid-State Lithium Batteries with Superior Electrochemical Performance. *ACS Appl Mater Interfaces* **2016,** *8* (43), 29705-29712.

201. Liu, M.; Zhou, D.; He, Y. B.; Fu, Y. Z.; Qin, X. Y.; Miao, C.; Du, H. D.; Li, B. H.; Yang, Q. H.; Lin, Z. Q.; Zhao, T. S.; Kang, F. Y., Novel gel polymer electrolyte for high-performance lithium-sulfur batteries. *Nano Energy* **2016,** *22*, 278-289.

202. Miao, R. R.; Yang, J.; Xu, Z. X.; Wang, J. L.; Nuli, Y.; Sun, L. M., A new ether-based electrolyte for dendrite-free lithium-metal based rechargeable batteries. *Sci Rep* **2016,** *6*.

203. Nie, M. Y.; Abraham, D. P.; Seo, D. M.; Chen, Y. J.; Bose, A.; Lucht, B. L., Role of Solution Structure in Solid Electrolyte lnterphase Formation on Graphite with LiPF6 in Propylene Carbonate. *J Phys Chem C* **2013,** *117* (48), 25381-25389.

204. Yoon, T.; Chapman, N.; Seo, D. M.; Lucht, B. L., Lithium Salt Effects on Silicon Electrode Performance and Solid Electrolyte Interphase (SEI) Structure, Role of Solution Structure on SEI Formation. *J Electrochem Soc* **2017,** *164* (9), A2082-A2088.

205. Niehoff, P.; Passerini, S.; Winter, M., Interface Investigations of a Commercial Lithium Ion Battery Graphite Anode Material by Sputter Depth Profile X-ray Photoelectron Spectroscopy. *Langmuir* **2013,** *29* (19), 5806-5816.

206. Xu, K.; von Cresce, A., Interfacing electrolytes with electrodes in Li ion batteries. *J Mater Chem* **2011,** *21* (27), 9849-9864.

207. Verma, P.; Maire, P.; Novak, P., A review of the features and analyses of the solid electrolyte interphase in Li-ion batteries. *Electrochim Acta* **2010,** *55* (22), 6332-6341.

208. Wang, D. Y.; Burns, J. C.; Dahn, J. R., A Systematic Study of the Concentration of Lithium Hexafluorophosphate (LiPF6) as a Salt for LiCoO2/Graphite Pouch Cells. *J Electrochem Soc* **2014,** *161* (9), A1278-A1283.

209. Lundgren, H.; Scheers, J.; Behm, M.; Lindbergh, G., Characterization of the Mass-Transport Phenomena in a Superconcentrated LiTFSI:Acetonitrile Electrolyte. *J Electrochem Soc* **2015,** *162* (7), A1334-A1340.

210. McOwen, D. W.; Seo, D. M.; Borodin, O.; Vatamanu, J.; Boyle, P. D.; Henderson, W. A., Concentrated electrolytes: decrypting electrolyte properties and reassessing Al corrosion mechanisms. *Energy Environ Sci* **2014,** *7* (1), 416-426.

211. Yang, L.; Ravdel, B.; Lucht, B. L., Electrolyte Reactions with the Surface of High Voltage LiNi0.5Mn1.5O4 Cathodes for Lithium-Ion Batteries. *Electrochem Solid-State Lett* **2010,** *13* (8), A95-A97.

212. MacNeil, D. D.; Lu, Z. H.; Chen, Z. H.; Dahn, J. R., A comparison of the electrode/electrolyte reaction at elevated temperatures for various Li-ion battery cathodes. *J Power Sources* **2002,** *108* (1-2), 8-14.

213. Hu, L. B.; Zhang, Z. C.; Amine, K., Electrochemical investigation of carbonate-based electrolytes for high voltage lithium-ion cells. *J Power Sources* **2013,** *236*, 175-180.

214. Brouillette, D.; Irish, D. E.; Taylor, N. J.; Perron, G.; Odziemkowski, M.; Desnoyers, J. E., Stable solvates in solution of lithium bis(trifluoromethylsulfone)imide in glymes and other aprotic solvents: Phase diagrams, crystallography and Raman spectroscopy. *Phys Chem Chem Phys* **2002,** *4* (24), 6063-6071.

215. Sogawa, M.; Sawayama, S.; Han, J.; Satou, C.; Ohara, K.; Matsugami, M.; Mimura, H.; Morita, M.; Fujii, K., Role of Solvent Size in Ordered Ionic Structure Formation in Concentrated Electrolytes for Lithium-Ion Batteries. *J Phys Chem C* **2019,** *123* (14), 8699-8708.

216. Han, S. D.; Borodin, O.; Seo, D. M.; Zhou, Z. B.; Henderson, W. A., Electrolyte Solvation and Ionic Association V. Acetonitrile-Lithium Bis(fluorosulfonyl)imide (LiFSI) Mixtures. *J Electrochem Soc* **2014,** *161* (14), A2042-A2053.

217. Mynam, M.; Ravikumar, B.; Rai, B., Molecular dynamics study of propylene carbonate based concentrated electrolyte solutions for lithium ion batteries. *J Mol Liq* **2019,** *278*, 97-104.

218. Seo, D. M.; Boyle, P. D.; Allen, J. L.; Han, S. D.; Jonsson, E.; Johansson, P.; Henderson, W. A., Solvate Structures and Computational/Spectroscopic Characterization of LiBF4 Electrolytes. *J Phys Chem C* **2014,** *118* (32), 18377-18386.

219. Seo, D. M.; Reininger, S.; Kutcher, M.; Redmond, K.; Euler, W. B.; Lucht, B. L., Role of Mixed Solvation and Ion Pairing in the Solution Structure of Lithium Ion Battery Electrolytes. *J Phys Chem C* **2015,** *119* (25), 14038-14046.

220. Takeuchi, M.; Matubayasi, N.; Kameda, Y.; Minofar, B.; Ishiguro, S.; Umebayashi, Y., Free-Energy and Structural Analysis of Ion Solvation and Contact Ion-Pair Formation of Li+ with BF4- and PF6- in Water and Carbonate Solvents. *J Phys Chem B* **2012,** *116* (22), 6476-6487.

221. Galle Kankanamge, S. R.; Kuroda, D. G., Molecular structure and ultrafast dynamics of sodium thiocyanate ion pairs formed in glymes of different lengths. *Phys Chem Chem Phys* **2019,** *21* (2), 833-841.

222. Frisch, M. J.; Trucks, G. W.; Schlegel, H. B.; Scuseria, G. E.; Robb, M. A.; Cheeseman, J. R.; Scalmani, G.; Barone, V.; Mennucci, B.; Petersson, G. A.; Nakatsuji, H.; Caricato, M.; Li, X.; Hratchian, H. P.; Izmaylov, A. F.; Bloino, J.; Zheng, G.; Sonnenberg, J. L.; Hada, M.; Ehara, M.; Toyota, K.; Fukuda, R.; Hasegawa, J.; Ishida, M.; Nakajima, T.; Honda, Y.; Kitao, O.; Nakai, H.; Vreven, T.; Montgomery, J. A.; Peralta, J. E.; Ogliaro, F.; Bearpark, M.; Heyd, J. J.; Brothers, E.; Kudin, K. N.; Staroverov, V. N.; Kobayashi, R.; Normand, J.; Raghavachari, K.; Rendell, A.; Burant, J. C.; Iyengar, S. S.; Tomasi, J.; Cossi, M.; Rega, N.; Millam, J. M.; Klene, M.; Knox, J. E.; Cross, J. B.; Bakken, V.; Adamo, C.; Jaramillo, J.; Gomperts, R.; Stratmann, R. E.; Yazyev, O.; Austin, A. J.; Cammi, R.; Pomelli, C.; Ochterski, J. W.; Martin, R. L.; Morokuma, K.; Zakrzewski, V. G.; Voth, G. A.; Salvador, P.; Dannenberg, J. J.; Dapprich, S.; Daniels, A. D.; Farkas; Foresman, J. B.; Ortiz, J. V.; Cioslowski, J.; Fox, D. J., Gaussian 09, Revision B.01. Wallingford CT, 2009.

223. Case, D. A.; Betz, R. M.; Cerutti, D. S.; Cheatham, T. E.; III, T. A. D.; Duke, R. E.; Giese, T. J.; Gohlke, H.; Goetz, A. W.; Homeyer, N.; Izadi, S.; Janowski, P.; Kaus, J.; Kovalenko, A.; Lee, T. S.; LeGrand, S.; P. Li, C. L.; Luchko, T.; Luo, R.; Madej, B.; Mermelstein, D.; Merz, K. M.; Monard, G.; Nguyen, H.; Nguyen, H. T.; Omelyan, I.; Onufriev, A.; Roe, D. R.; Roitberg, A.; Sagui, C.; C.L. Simmerling; Botello-Smith, W. M.; Swails, J.; Walker, R. C.; Wang, J.; Wolf, R. M.; Wu, X.; Xiao, L.; Kollman, P. A., AMBER 2016,University of California, San Francisco. **2016**.

224. Sprenger, K. G.; Jaeger, V. W.; Pfaendtner, J., The General AMBER Force Field (GAFF) Can Accurately Predict Thermodynamic and Transport Properties of Many Ionic Liquids. *J Phys Chem B* **2015,** *119* (18), 5882-5895.

225. Kumar, N.; Seminario, J. M., Lithium-Ion Model Behavior in an Ethylene Carbonate Electrolyte Using Molecular Dynamics. *J Phys Chem C* **2016,** *120* (30), 16322-16332.

226. Barthel, J.; Buchner, R.; Wismeth, E., FTIR spectroscopy of ion solvation of LiClO4 and LiSCN in acetonitrile, benzonitrile, and propylene carbonate. *J Solution Chem* **2000,** *29* (10), 937-954.

227. Amunson, K. E.; Kubelka, J., On the temperature dependence of amide I frequencies of peptides in solution. *J Phys Chem B* **2007,** *111* (33), 9993-9998.

228. Bhatt, M. D.; Cho, M.; Cho, K., Interaction of Li+ ions with ethylene carbonate (EC): Density functional theory calculations. *Appl Surf Sci* **2010,** *257* (5), 1463-1468.

229. Ding, W. H.; Lei, X. L.; Ouyang, C. Y., Coordination of Lithium Ion with Ethylene Carbonate Electrolyte Solvent: A Computational Study. *Int J Quantum Chem* **2016,** *116* (2), 97-102.

230. Li, T.; Balbuena, P. B., Theoretical studies of lithium perchlorate in ethylene carbonate, propylene carbonate, and their mixtures. *J Electrochem Soc* **1999,** *146* (10), 3613-3622.

231. Hyodo, S. A.; Okabayashi, K., Raman Intensity Study of Local-Structure in Non-Aqueous Electrolyte-Solutions .2. Cation Solvent Interaction in Mixed-Solvent Systems and Selective Solvation. *Electrochim Acta* **1989,** *34* (11), 1557-1561.

232. Doucey, L.; Revault, M.; Lautie, A.; Chausse, A.; Messina, R., A study of the Li/Li+ couple in DMC and PC solvents - Part 1: Characterization of LiAsF6/DMC and LiAsF6/PC solutions. *Electrochim Acta* **1999,** *44* (14), 2371-2377.

233. Kameda, Y.; Umebayashi, Y.; Takeuchi, M.; Wahab, M. A.; Fukuda, S.; Ishiguro, S. I.; Sasaki, M.; Amo, Y.; Usuki, T., Solvation structure of Li+ in concentrated LiPF6-propylene carbonate solutions. *J Phys Chem B* **2007,** *111* (22), 6104-6109.

234. Morita, M.; Asai, Y.; Yoshimoto, N.; Ishikawa, M., A Raman spectroscopic study of organic electrolyte solutions based on binary solvent systems of ethylene carbonate with low viscosity solvents which dissolve different lithium salts. *J Chem Soc, Faraday Trans* **1998,** *94* (23), 3451-3456.

235. Zhang, X.; Kuroda, D. G., An ab initio molecular dynamics study of the solvation structure and ultrafast dynamics of lithium salts in organic carbonates: A comparison between linear and cyclic carbonates. *J Chem Phys* **2019,** *150* (18), 184501.

236. Tasaki, K.; Goldberg, A.; Liang, J.-J.; Winter, M., New Insight into Electrochemical Differences in Cycling Behaviors of a Lithium-ion Battery Cell Between the Ethylene Carbonate- and Propylene Carbonate-Based Electrolytes. *MRS Proceedings* **2011,** *1313*, mrsf10-1313-kk11-01.

237. Yuan, K. J.; Bian, H. T.; Shen, Y. N.; Jiang, B.; Li, J. B.; Zhang, Y. F.; Chen, H. L.; Zheng, J. R., Coordination Number of Li+ in Nonaqueous Electrolyte Solutions Determined by Molecular Rotational Measurements. *J Phys Chem B* **2014,** *118* (13), 3689-3695.

238. Borodin, O.; Smith, G. D., LiTFSI structure and transport in ethylene carbonate from molecular dynamics simulations. *J Phys Chem B* **2006,** *110* (10), 4971-4977.

239. Borodin, O.; Smith, G. D., Quantum Chemistry and Molecular Dynamics Simulation Study of Dimethyl Carbonate: Ethylene Carbonate Electrolytes Doped with LiPF6. *J Phys Chem B* **2009,** *113* (6), 1763-1776.

240. Ong, M. T.; Verners, O.; Draeger, E. W.; van Duin, A. C. T.; Lordi, V.; Pask, J. E., Lithium Ion Solvation and Diffusion in Bulk Organic Electrolytes from First-Principles and Classical Reactive Molecular Dynamics. *J Phys Chem B* **2015,** *119* (4), 1535-1545.

241. Lee, K.-K.; Park, K.; Lee, H.; Noh, Y.; Kossowska, D.; Kwak, K.; Cho, M., Ultrafast fluxional exchange dynamics in electrolyte solvation sheath of lithium ion battery. *Nat Commun* **2017,** *8*.

242. Jiang, B.; Ponnuchamy, V.; Shen, Y. N.; Yang, X. M.; Yuan, K. J.; Vetere, V.; Mossa, S.; Skarmoutsos, I.; Zhang, Y. F.; Zheng, J. R., The Anion Effect on Li+ Ion Coordination Structure in Ethylene Carbonate Solutions. *J Phys Chem Lett* **2016,** *7* (18), 3554-3559.

243. Borodin, O.; Suo, L. M.; Gobet, M.; Ren, X. M.; Wang, F.; Faraone, A.; Peng, J.; Olguin, M.; Schroeder, M.; Ding, M. S.; Gobrogge, E.; Cresce, A. V.; Munoz, S.; Dura, J. A.;

Greenbaum, S.; Wang, C. S.; Xu, K., Liquid Structure with Nano-Heterogeneity Promotes Cationic Transport in Concentrated Electrolytes. *ACS Nano* **2017,** *11* (10), 10462-10471.

244. Tagawa, A.; Numata, T.; Shikata, T., Anti-parallel dimer and tetramer formation of propylene carbonate. *Aip Adv* **2017,** *7* (9).

245. Bohets, H.; van der Veken, B. J., On the conformational behavior of dimethyl carbonate. *Phys Chem Chem Phys* **1999,** *1* (8), 1817-1826.

246. Gontrani, L.; Russina, O.; Marincola, F. C.; Caminiti, R., An energy dispersive x-ray scattering and molecular dynamics study of liquid dimethyl carbonate. *J Chem Phys* **2009,** *131* (24).

247. Kwac, K.; Cho, M., Molecular dynamics simulation study of N-methylacetamide in water. II. Two-dimensional infrared pump-probe spectra. *Journal of Chemical Physics* **2003,** *119* (4), 2256-2263.

248. Kar, B. P.; Ramanathan, N.; Sundararajan, K.; Viswanathan, K. S., Conformations of dimethyl carbonate and its complexes with water: A matrix isolation infrared and ab initio study. *J Mol Struct* **2012,** *1024*, 84-93.

249. Golonzka, O.; Khalil, M.; Demirdoven, N.; Tokmakoff, A., Coupling and orientation between anharmonic vibrations characterized with two-dimensional infrared vibrational echo spectroscopy. *J Chem Phys* **2001,** *115* (23), 10814-10828.

250. Kim, Y. S.; Hochstrasser, R. M., Chemical exchange 2D IR of hydrogen-bond making and breaking. *P Natl Acad Sci USA* **2005,** *102* (32), 11185-11190.

251. Herstedt, M.; Smirnov, M.; Johansson, P.; Chami, M.; Grondin, J.; Servant, L.; Lassegues, J. C., Spectroscopic characterization of the conformational states of the bis (trifluoromethanesulfonyl)imide anion (TFSI-). *J Raman Spectrosc* **2005,** *36* (8), 762-770.

252. Johansson, P.; Gejji, S. P.; Tegenfeldt, J.; Lindgren, J., The imide ion: potential energy surface and geometries. *Electrochim Acta* **1998,** *43* (10-11), 1375-1379.

253. Lassegues, J. C.; Grondin, J.; Aupetit, C.; Johansson, P., Spectroscopic Identification of the Lithium Ion Transporting Species in LiTFSI-Doped Ionic Liquids. *J Phys Chem A* **2009,** *113* (1), 305-314.

254. Taylor, R., Interpretation of the Correlation-Coefficient - a Basic Review. *J Diagn Med Sonog* **1990,** *6* (1), 35-39.

255. Hanggi, P.; Talkner, P.; Borkovec, M., Reaction-Rate Theory - 50 Years after Kramers. *Rev Mod Phys* **1990,** *62* (2), 251-341.

256. Laage, D.; Hynes, J. T., On the residence time for water in a solute hydration shell: Application to aqueous halide solutions. *J Phys Chem B* **2008,** *112* (26), 7697-7701.

257. Flores, E.; Åvall, G.; Jeschke, S.; Johansson, P., Solvation structure in dilute to highly concentrated electrolytes for lithium-ion and sodium-ion batteries. *Electrochim Acta* **2017,** *233*, 134-141.

258. Takeuchi, M.; Kameda, Y.; Umebayashi, Y.; Ogawa, S.; Sonoda, T.; Ishiguro, S.-i.; Fujita, M.; Sano, M., Ion–ion interactions of LiPF6 and LiBF4 in propylene carbonate solutions. *J Mol Liq* **2009,** *148* (2-3), 99-108.

259. Borodin, O.; Olguin, M.; Ganesh, P.; Kent, P. R.; Allen, J. L.; Henderson, W. A., Competitive lithium solvation of linear and cyclic carbonates from quantum chemistry. *Phys Chem Chem Phys* **2016,** *18* (1), 164-175.

260. Krachkovskiy, S. A.; Bazak, J. D.; Werhun, P.; Balcom, B. J.; Halalay, I. C.; Goward, G. R., Visualization of steady-state ionic concentration profiles formed in electrolytes during Li-ion battery operation and determination of mass-transport properties by in situ magnetic resonance imaging. *J Am Chem Soc* **2016,** *138* (25), 7992-7999.

261. Klett, M.; Giesecke, M.; Nyman, A.; Hallberg, F.; Lindström, R. W.; Lindbergh, G. r.; Furó, I. n., Quantifying mass transport during polarization in a Li Ion battery electrolyte by in situ 7Li NMR imaging. *J Am Chem Soc* **2012,** *134* (36), 14654-14657.

262. Wiemers-Meyer, S.; Winter, M.; Nowak, S., A battery cell for in situ NMR measurements of liquid electrolytes. *Phys Chem Chem Phys* **2017,** *19* (7), 4962-4966.

263. Klamor, S.; Zick, K.; Oerther, T.; Schappacher, F.; Winter, M.; Brunklaus, G., 7 Li in situ 1D NMR imaging of a lithium ion battery. *Phys Chem Chem Phys* **2015,** *17* (6), 4458-4465.

264. Chien, P.-H.; Feng, X.; Tang, M.; Rosenberg, J. T.; O'Neill, S.; Zheng, J.; Grant, S. C.; Hu, Y.-Y., Li Distribution heterogeneity in solid electrolyte Li10GeP2S12 upon electrochemical cycling probed by 7Li MRI. *J Phys Chem Lett* **2018,** *9* (8), 1990-1998.

265. Forster, J. D.; Harris, S. J.; Urban, J. J., Mapping Li+ concentration and transport via in situ confocal Raman microscopy. *J Phys Chem Lett* **2014,** *5* (11), 2007-2011.

266. Brissot, C.; Rosso, M.; Chazalviel, J.-N.; Lascaud, S., Concentration measurements in lithium/polymer–electrolyte/lithium cells during cycling. *J Power Sources* **2001,** *94* (2), 212-218.

267. Yamanaka, T.; Nakagawa, H.; Tsubouchi, S.; Domi, Y.; Doi, T.; Abe, T.; Ogumi, Z., In situ Raman spectroscopic studies on concentration change of ions in the electrolyte solution in separator regions in a lithium ion battery by using multi-microprobes. *Electrochem Commun* **2017,** *77*, 32-35.

268. Yamanaka, T.; Nakagawa, H.; Tsubouchi, S.; Domi, Y.; Doi, T.; Abe, T.; Ogumi, Z., In situ Raman spectroscopic studies on concentration change of electrolyte salt in a lithium ion model battery with closely faced graphite composite and LiCoO2 composite electrodes by using an ultrafine microprobe. *Electrochim Acta* **2017,** *234*, 93-98.

269. Niedzicki, L.; Karpierz, E.; Bitner, A.; Kasprzyk, M.; Zukowska, G.; Marcinek, M.; Wieczorek, W., Optimization of the lithium-ion cell electrolyte composition through the use of the LiTDI salt. *Electrochim Acta* **2014,** *117*, 224-229.

270. Xu, K., Nonaqueous liquid electrolytes for lithium-based rechargeable batteries. *Chem Rev* **2004,** *104* (10), 4303-4418.

271. Bath, B. D.; White, H. S.; Scott, E. R., Electrically facilitated molecular transport. Analysis of the relative contributions of diffusion, migration, and electroosmosis to solute transport in an ion-exchange membrane. *Anal Chem* **2000,** *72* (3), 433-442.

272. Szymczyk, A.; Labbez, C.; Fievet, P.; Vidonne, A.; Foissy, A.; Pagetti, J., Contribution of convection, diffusion and migration to electrolyte transport through nanofiltration membranes. *Adv Colloid Interface Sci* **2003,** *103* (1), 77-94.

273. Ue, M.; Ida, K.; Mori, S., Electrochemical properties of organic liquid electrolytes based on quaternary onium salts for electrical double-layer capacitors. *J Electrochem Soc* **1994,** *141* (11), 2989.

274. Kuroda, D. G.; Singh, P. K.; Hochstrasser, R. M., Differential Hydration of Tricyanomethanide Observed by Time Resolved Vibrational Spectroscopy. *J Phys Chem B* **2013,** *117* (16), 4354-4364.

275. Weidinger, D.; Houchins, C.; Owrutsky, J. C., Vibrational dynamics of tricyanomethanide. *Chem Phys Lett* **2012,** *525*, 60-63.

VITA

Susith Rajitha Abeythunga Galle Kankanamge was born in Galle, Sri Lanka to Dolison Abeythunga and Hemalatha Kulathunga. He is the third of four children (Yasith, Lasith, Malithi-siblings). Susith graduated from St. Aloysius College in Galle in 2008 and attended University of Colombo from 2009 to 2014 where he graduated with his Bachelor of Science in Chemistry. Then he started his graduate studies at Louisiana State University in 2015. Later in the same year he joined with Kuroda group to study the structure and dynamics of novel battery electrolyte with multidimensional infrared spectroscopic techniques. Susith plans to graduate with a doctorate in Physical Chemistry.